Constraining the Dark Energy Equation of State Using Alternative Cosmic Tracers

by

Ricardo Chávez

Thesis submitted in partial fulfillment of the requirements
for the degree of

MASTER OF SCIENCE IN ASTROPHYSICS

at the

Instituto Nacional de Astrofísica, Óptica y Electrónica
July 2010
Tonantzintla, Puebla

Under the supervision of:

Ph.D. Roberto Terlevich
Tenured Researcher INAOE, Mexico
Ph.D. Elena Terlevich
Tenured Researcher INAOE, Mexico
Ph.D. Manolis Plionis
Tenured Researcher INAOE, Mexico & NOA, Greece

To my parents, for their tireless support.

Abstract

We propose to use the H II galaxies redshift-distance relation, measured by means of their $L(\mathrm{H}\beta) - \sigma$ correlation, in order to determine the Hubble function to intermediate and high redshifts, in an attempt to constrain the dark energy equation of state parameters solution space, as an alternative to the cosmological use of type Ia supernovae.

So that we can use effectively high redshift H II galaxies as probes for dark energy equation of state parameters, we must reassess the $L(\mathrm{H}\beta) - \sigma$ distance estimator, minimizing the observational uncertainties and taking care of the possible associated systematics, such as stellar age, gas metallicity, reddening, environment and morphology.

In order to reassess the $L(\mathrm{H}\beta) - \sigma$ distance estimator, we have selected and observed a sample of 128 H II galaxies from the local universe. From a preliminary analysis, which does not yet take care of the possible systematic effects, we have obtained a relation given by $\log_{10} L(\mathrm{H}\beta) = (3.95 \pm 0.10) \log_{10} \sigma + (34.68 \pm 0.17)$, which has an associated dispersion, $\delta \log_{10} L(\mathrm{H}\beta) = 0.299$, similar to the one obtained in previous works (Melnick et al., 1988).

The selection of a intermediate and high redshift sample of H II galaxies, its accurate observation and analysis, using the previously reassessed $L(\mathrm{H}\beta) - \sigma$ distance estimator, is a crucial task to be accomplished in order to realize our final objectives and it will realized during my doctoral research.

Resumen

Se propone utilizar la relación corrimiento al rojo - distancia para galaxias H II, medida mediante su correlación $L(\mathrm{H}\beta) - \sigma$, con el propósito de determinar la función de Hubble a corrimientos al rojo intermedios y altos, en un intento para restringir el espacio de soluciones de los parámetros de la ecuación de estado de la energía oscura; como una alternativa al uso cosmológico de supernovas de tipo Ia.

De modo que sea posible el uso efectivo de galaxias H II a alto corrimiento al rojo como trazadores de los parámetros de la ecuación de estado de la energía oscura, se hace necesario re-evaluar el estimador de distancia $L(\mathrm{H}\beta) - \sigma$, minimizando las incertidumbres observacionales y tomando en cuenta los posibles errores sistemáticos asociados, tales como edad estelar, metalicidad del gas, enrojecimiento, medio ambiente y morfología.

Con la intención de re-evaluar el estimador de distancia $L(\mathrm{H}\beta) - \sigma$, se ha seleccionado y observado una muestra de 128 galaxias H II del universo local. De un análisis preliminar, que aún no toma en cuenta los posibles effectos sistemáticos, se ha obtenido una relación dada por $\log_{10} L(\mathrm{H}\beta) = (3.95 \pm 0.10) \log_{10} \sigma + (34.68 \pm 0.17)$, la cual tiene una dispersion asociada, $\delta \log_{10} L(\mathrm{H}\beta) = 0.299$, similar a la que se ha obtenido en trabajos previos (Melnick et al., 1988).

La selección de una muestra de galaxias H II a corrimiento al rojo intermedio y alto, su observación precisa y análisis, utilizando el estimador de distancia $L(\mathrm{H}\beta) - \sigma$ previamente re-evaluado, es una tarea crucial a llevar a cabo para conseguir los objetivos planteados y sera efectuada durante la investigación doctoral.

Preface

The terms "cosmological constant" and more recently "dark energy" and "modified gravity" have been remainders of our incomplete understanding of the "physical reality". The fundamental problems have been inconsistencies arising between the observational and theoretical approaches or even between the two main theoretical alternatives.

The "knowledge" is constructed progressively, harsh and lengthy battles between proud theoretical systems, between judgements, must be fought before a glimpse of certainty may be acquired. However, sometimes an apparently tractable *petit* problem has been enough to "demolish" the noblest system.

The cosmic acceleration, detected at the end of the 1990s, could be one of this class of problems that are the key to a new view of reality. First of all, this problem is related to many current fields in physics, crossing from gravitation to quantum field theory and to the unknown in the incarnation of quantum gravity with its multiple flavors (eg. string theory, loop quantum gravity, twistor theory, ...). Even more, the quest for a theoretical account of the observed acceleration has given an enormous impetus to the search for alternative theories of gravity.

The theoretical explanations for the cosmic acceleration are many and diverse, first of all we have the cosmological constant as a form of vacuum energy, then we are faced with a multitude of models in which the origin for the acceleration is explained by means of a substance with an exotic equation of state, and finally we encounter explanations based on modifications of the general relativity theory.

The fact is that the current empirical data are not enough to discriminate between the great number of theoretical models, and therefore if we want to eventually decide on which is the best model we will need more and accurate data.

This work is devoted to explore the possibility of using H II galaxies as probes for the

cosmic expansion history. Many distinct probes already have been used or proposed, such as type Ia Supernovae (SNe Ia), baryon acoustic oscillations, galaxy clusters and weak lensing. From the previously mentioned only type Ia Supernovae and H II galaxies are purely geometrical probes (i.e. related directly to the metric), whereas the others are growth probes (i.e. related to the rate of growth of matter density perturbations) or a combination of both.

The advantage of using H II galaxies over the use of type Ia Supernovae, as probes of comic acceleration, is that H II galaxies can be observed easily to higher redshifts. However, the H II galaxies distance modulus determinations, through their $L(H\beta) - \sigma$ relation, have larger uncertainties than those of type Ia Supernovae. Nevertheless, H II galaxies would be a valuable complement to the type Ia Supernovae data, especially at high redshifts, and even more they could also be used as a confirmation for cosmic acceleration, which for the present is based only on SNe Ia.

The use of H II galaxies as probes of cosmic acceleration is conditioned to our succeeding in improving its $L(H\beta) - \sigma$ relation, obtaining an accurate determination of its zero point and reducing its scatter, and finally taking care of all the systematics that can possibly affect it.

H II galaxies are a promising new avenue for the determination of the cosmic expansion history. Their true value will be seen and assessed during coming years, when a enough large sample of intermediate and high redshift objects will have been observed and analysed.

Acknowledgments

List of Symbols

We have attempted to keep the basic notation as standard as possible. In general, the notation is always defined at its first occurrence in the text. The signature of the metric is assumed to be $(+, -, -, -)$ and the speed of light, c, is taken to be equal to 1 throughout this work, unless otherwise specified. Throughout this work the Einstein summation convention is assumed. Note that throughout this thesis the subscript 0 denotes a parameter's present epoch value, unless otherwise specified.

$\Box$ The D'Alembert operator.

χ The comoving distance.

χ^2 The Chi-square merit function.

δ_k The perturbations to the mass-energy density decomposed into their Fourier modes.

Γ^a_{bc} The metric connection coefficients or Christoffel symbols.

κ The Einstein's gravitational constant.

Λ The cosmological constant.

$\mathcal{L}$ The Lagrangian density or the likelihood estimator.

μ The distance modulus.

Ω The mass-energy density nomarlized to the present ρ_c value.

ρ The mass-energy density.

ρ_c	The critical density (that required for the Universe to have a flat spatial geometry).
σ	The emisson-line width.
$a(t)$	The cosmic scale factor.
c_s	The sound speed.
D_A	The angular distance.
D_L	The luminosity distance.
D_M	The proper distance.
dV	The comoving volume element.
F	The flux.
$G_{\mu\nu}$	The Einstein tensor.
$g_{\mu\nu}$	The metric.
H	The Hubble parameter.
h	The dimensionless Hubble parameter.
L	The luminosity.
M_z	The H II galaxies distance indicator.
p	The pressure.
$q(t)$	The deceleration parameter .
R	The Ricci scalar.
$R_{\mu\nu}$	The Ricci tensor.
R_{curv}	The curvature radius.
R_c	The core radius.

S The action.

s The scale of acoustic oscillations.

$t(z)$ The cosmological time.

$T_{\mu\nu}$ The stress-energy tensor.

W The line equivalent width.

w The equation of state parameter.

z The redshift.

Contents

Chapter 1

Introduction

Our current understanding of the cosmological evidence shows that our Universe is homogeneous on large-scales, spatially flat and in an accelerated expansion phase; is composed of baryons, some sort of cold dark matter and a component which acts as having a negative pressure (dubbed "dark energy" or cosmological constant), which explains the accelerated cosmic expansion. The Universe underwent an inflationary infancy of an extremely rapid growth, followed by a phase of gentler expansion driven initially by its relativistic and then by its non-relativistic contents but by now its evolution is governed by the dark energy component [eg., Ratra & Vogeley (2008); Frieman et al. (2008)].

The observational evidence of the dark energy component was presented in 1998 when two teams studying type Ia supernovae (SNe Ia), the *Supernova Cosmology Project* and the *High-z Supernova Search*, found independently that the distances of these objects were farther than expected in a Universe without cosmological constant (Riess et al., 1998; Perlmutter et al., 1999). Since then measurements of cosmic microwave background (CMB) anisotropy [eg., Jaffe et al. (2001); Pryke et al. (2002); Spergel et al. (2007)] and of large-scale structure (LSS) [eg., Tegmark et al. (2004); Seljak et al. (2005)], in combination with independent Hubble relation measurements (Freedman et al., 2001), have confirmed the accelerated expansion of the Universe.

The accumulated evidence imply that nearly 70% of the total mass-energy of the Universe is composed of the mysterious dark energy; although its nature is still largely unknown. Possible candidates of the cause of the accelerated expansion of the Universe

are Einstein's cosmological constant, which implies that the dark energy component is constant in time and uniform in space (Carroll, 2001); or perhaps the dark energy is an exotic form of matter of which the equation of state could be time dependent [eg., Copeland et al. (2006)]; or even that the range of validity of General Relativity (GR) is limited.

From the previous discussion we can see that understanding the nature of dark energy is of paramount importance and it could have deep implications for fundamental physics; it is thus of no surprise that this problem has been called out prominently in recent policy reports (Albrecht et al., 2006; Peacock et al., 2006) where extensive experimental programs to explore dark energy have been put forward.

To the present day, the cosmic acceleration has been traced directly only by means of SNe Ia and at redshifts $z \lesssim 1$, a fact which implies that it is of great importance to use alternative geometrical probes at higher redshifts in order to verify the SNe Ia results and to obtain more stringent constrains in the cosmological parameters solution space, with the final aim of discriminating among the various theoretical alternatives that attempt to explain the accelerated expansion of the Universe.

1.1 Aims of This Work

The main objective of this work is to trace the Hubble function using the redshift-distance relation of H II galaxies, as an alternative to SNe Ia, in an attempt to constrain the dark energy equation of state, combining also the results of the clustering method [eg., Plionis et al. (2009)]. The main reasons for choosing H II galaxies as alternative tracers of the Hubble function, are:

- H II galaxies can be used as standard candles (Melnick et al., 2000; Melnick, 2003; Siegel et al., 2005) due to the correlation between their velocity dispersion and $H\beta$-line luminosity (Melnick, 1978; Terlevich & Melnick, 1981; Melnick et al., 1988).

- H II galaxies can be observed to higher redshifts than those sampled by current SNe Ia surveys and thus probe a region where the Hubble function is more sensitive to the cosmological parameters.

- The use of H II galaxies as alternative high-z tracer will enable us, to some extent, to independently verify the SNe Ia based results.

In order to use effectively high-z H II galaxies as geometrical probes, we need to re-assess the $L(\mathrm{H}\beta) - \sigma$ distance estimator, since this was originally done 30 years ago using non-linear detectors and without including corrections for effects such as the galaxy peculiar motions and environmental dependencies. Having this objective in mind, we must investigate, at low-z's, all the parameters that can systematically affect the distance estimator; among which the stellar age, metallicity, extinction, environment, etc., with the intention to determine accurately the estimator's zero-point.

1.2 Structure of This Work

Through the second chapter we will be presenting the cosmic acceleration problem, its observational evidence, its implications and possible theoretical explanations and finally the possible avenues to constrain its parameters solution space in order to obtain a better understanding of its nature, than what is currently owned.

The third chapter explores the fundamental properties of H II galaxies, its $L(\mathrm{H}\beta) - \sigma$ relation, its possible systematics, the possibility of using H II galaxies as distance indicators and finally the related cosmological implications.

Through the fourth chapter we will explain the methodology to locally re-assess the $L(\mathrm{H}\beta) - \sigma$ relation for H II galaxies in order to use them as cosmological probes at high redshifts. In the same form, we will describe the methodology to analyse an intermediate and high-z sample of H II galaxies in order to constraint the parameters space of the dark energy equation of state.

In the fifth chapter we explore in detail the local sample of H II galaxies and show some preliminary results regarding the $L(\mathrm{H}\beta) - \sigma$ relation.

Finally, in the sixth chapter we will overview the future work to be accomplished during the doctoral research and we will give some concluding remarks.

Chapter 2

The Cosmic Acceleration Problem

The cause of the cosmic acceleration is one of the most intriguing problems in all physics. In one form or another it is related to gravitation, high energy physics, extra dimensions, quantum field theory and even more exotic areas of Physics as quantum gravity or worm holes. However, we still know very little regarding the mechanism that drives the accelerated expansion of the Universe.

Due to the lack of a fundamental physical theory explaining the accelerated expansion, there have been many theoretical speculations about the nature of dark energy [eg., Caldwell & Kamionkowski (2009); Frieman et al. (2008)]; furthermore and most importantly, the current observational/experimental data are not adequate to distinguish between the many adversary theoretical models.

Essentially one can probe dark energy by one or more of the following methods:

- Geometrical probes of the cosmic expansion, which are directly related to the metric like distances and volumes.

- Growth probes related to the growth rate of the matter density perturbations.

The existence of dark energy was first inferred from a geometrical probe, the redshift-distance relation of type Ia supernovae (Riess et al., 1998; Perlmutter et al., 1999); while this method continues to be the only that probes directly the cosmic acceleration. The recent *Union2* compilation of SNe Ia data (Amanullah et al., 2010) and other cosmological probes are consistent with a cosmological constant, although the results, within reasonable statistical uncertainty, also agree with many dynamical dark-energy

models (Linder, 2010). It is therefore of great importance to trace the Hubble function, by means of a geometrical probe, at higher redshifts than currently probed, since at higher redshifts the different models deviate significantly from each other.

In this chapter we will explore the Cosmic Acceleration issue; the first section is devoted to a general account of the basics of theoretical and observational cosmology, in the second section we present a brief outlook of the observational evidence which supports the cosmic acceleration; later we will survey some of the theoretical explanations of the accelerating expansion and finally we will overview some probes currently used in the attempt to constrain the dark energy parameters.

Finally, a few words of caution regarding the used terminology. Through this chapter we will be using the term *dark energy* as opposed to *cosmological constant*, in the sense of a time-evolving cause of the cosmic acceleration. However, in later chapters we will use only the term *dark energy* since we consider it as the most general model, of which the *cosmological constant* is (mathematically) a particular case, while it effectively reproduces also the phenomenology of some modified gravity models.

2.1 Cosmology Basics

The fundamental assumption over which our current understanding of the Universe is constructed is known as the cosmological principle, which states that the Universe is homogeneous and isotropic on large-scales. The evidences that sustain the cosmological principle are basically the near-uniformity of the CMB temperature (Spergel et al., 2003) and the large-scale distribution of galaxies (Yadav et al., 2005).

Under the assumption of homogeneity and isotropy, the geometrical properties of space-time are described by the Friedmann-Robertson-Walker (FRW) metric (Robertson, 1935), given by

$$ds^2 = dt^2 - a^2(t) \left[\frac{dr^2}{1 - kr^2} + r^2(d\theta^2 + \sin^2\theta d\phi^2) \right], \qquad (2.1)$$

where r, θ, ϕ are spatial comoving coordinates (i.e., where a freely falling particle comes to rest) and t is the time parameter, whereas $a(t)$ is the cosmic scale factor which at the present epoch, t_0, has a value $a(t_0) = 1$; k is the curvature of the space, such that $k = 0$ corresponds to a spatially flat Universe, $k > 0$ to a positive curvature

(three-sphere) and $k < 0$ to a negative curvature (saddle as a 2-D analogue). Note that we are using units where the speed of light, $c = 1$.

From the FRW metric we can derive the cosmological redshift, i.e. the amount that a photon's wavelength (λ) increases due to the scaling of the photon's energy with $a(t)$, with corresponding definition:

$$1 + z \equiv \frac{\lambda_0}{\lambda_e} = \frac{a(t_0)}{a(t)} = \frac{1}{a(t)}, \tag{2.2}$$

where, z is the redshift, λ_0 is the observer's frame wavelength and λ_e is the emission's frame wavelength. Note that throughout this thesis the subscript 0 denotes a parameter's present epoch value.

In order to determine the dynamics of the space-time geometry we must solve the GR field equations for the FRW metric, in the presence of matter, obtaining the cosmological field equations or Friedmann-Lemaître equations (for a full derivation see Appendix A):

$$\left(\frac{\dot{a}}{a}\right)^2 = \frac{8\pi G\rho}{3} - \frac{k}{a^2} + \frac{\Lambda}{3}, \tag{2.3}$$

$$\frac{\ddot{a}}{a} = -\frac{4\pi G}{3}(\rho + 3p) + \frac{\Lambda}{3}, \tag{2.4}$$

where ρ is the total energy density of the Universe, p is the total pressure and Λ is the cosmological constant.

In eq.(2.3) we can define the Hubble parameter

$$H \equiv \frac{\dot{a}}{a}, \tag{2.5}$$

of which its present value is conventionally expressed as $H_0 = 100h$ km s^{-1} Mpc^{-1}, where $h = 0.73 \pm 0.019$ (Freedman et al., 2001; Tegmark et al., 2006) is the dimensionless Hubble parameter.

The time derivative of eq.(2.3) gives:

$$\ddot{a} = \frac{8\pi G}{3}\left(\rho a + \frac{\dot{\rho}a^2}{2\dot{a}}\right) + \frac{\Lambda a}{3},$$

and from the above and eq.(2.4) we can eliminate $\ddot{a}$ to obtain

$$\frac{-4\pi Ga}{3}\left[(\rho + 3p) + 2\left(\rho + \frac{\dot{\rho}a}{2\dot{a}}\right)\right] = 0$$

$$\frac{a}{\dot{a}}\dot{\rho} + 3(\rho + p) = 0,$$

which then gives:

$$\dot{\rho} + \frac{3\dot{a}}{a}(\rho + p) = 0, \tag{2.6}$$

which is an expression of energy conservation.

Equation (2.6) can be written as

$$\frac{d(\rho a^3)}{dt} = -3a^2 \dot{a} p \tag{2.7}$$

$$\frac{d(\rho a^3)}{da} = -3a^2 p, \tag{2.8}$$

and thus:

$$d(\rho_i a^3) = -p_i da^3, \tag{2.9}$$

where the subscript i runs over all the components of the Universe. Equation (2.9) is the expanding universe analog of the first law of thermodynamics, $dE = -pdV$.

If we assume that the different components of the cosmological fluid have an equation of state of the generic form:

$$p_i = w_i \rho_i, \tag{2.10}$$

then from eq.(2.8) we have

$$\frac{d(\rho_i a^3)}{da} = -3w_i \rho_i a^2, \tag{2.11}$$

which in the case where the equation of state parameter depends on time, ie., $w_i(a)$, it takes the following form:

$$\rho_i \propto \exp\left\{-3 \int \frac{da}{a}[1 + w_i(a)]\right\}. \tag{2.12}$$

For the particular case where w_i is a constant through cosmic time, we have

$$\rho_i \propto a^{-3(1+w_i)}, \tag{2.13}$$

where $w_i \equiv p_i/\rho_i$. These last two equations can be written as a function of redshift, defined by the eq.(2.2), as:

$$\rho_i \propto \exp\left[3 \int_0^z \frac{1 + w_i(z')}{1 + z'} dz'\right], \tag{2.14}$$

$$\rho_i \propto (1 + z)^{3(1+w_i)}. \tag{2.15}$$

For the case of non-relativistic matter (dark matter and baryons), $w_m = 0$ and $\rho_m \propto (1 + z)^3$, while for relativistic particles (radiation and neutrinos), $w_r = 1/3$ and $\rho_r \propto$

$(1+z)^4$, while for vacuum energy (cosmological constant), $w_\Lambda = -1$ and for which we have $p_\Lambda = -\rho_\Lambda = -\Lambda/8\pi G$.

In general the dark energy equation of state can be parameterized as (Plionis et al., 2009)

$$p_w = w(z)\rho_w, \tag{2.16}$$

where

$$w(z) = w_0 + w_1 f(z), \tag{2.17}$$

with $w_0 = w(0)$ and $f(z)$ is an increasing function of redshift, such as $f(z) = z/(1+z)$ (Linder, 2003).

The critical density can be defined as that required for the Universe to have a flat spatial geometry. From eq.(2.3), where we subsume the cosmological constant into the density term, and the definition of the Hubble parameter, eq.(2.5), we have that:

$$\rho_c \equiv \frac{3H_0^2}{8\pi G} = 1.88 \times 10^{-29} h^2 \text{ g cm}^{-3} = 8.10 \times 10^{-47} h^2 \text{ GeV}^4 . \tag{2.18}$$

This parameter provides a convenient mean to normalize the mass-energy densities of the different cosmic components, and we can write:

$$\Omega_i = \frac{\rho_i(t_0)}{\rho_c} , \tag{2.19}$$

where the subscript i runs over all the different components of the cosmological fluid. Using this last definition and eq.(2.14) we can write eq.(2.3) as:

$$H^2(z) = H_0^2 \left[\Omega_r (1+z)^4 + \Omega_m (1+z)^3 + \Omega_k (1+z)^2 + \Omega_w \exp\left(3 \int_0^z \frac{1+w(x)}{1+x} dx \right) \right], \tag{2.20}$$

where Ω_k has been defined as

$$\Omega_k \equiv \frac{-k}{a^2 H_0^2} .$$

By definition we have that $\Omega_r + \Omega_m + \Omega_k + \Omega_w \equiv 1$, and as a useful parameter we can define $\Omega_0 \equiv \Omega_r + \Omega_m + \Omega_w$, such that for a positively curved Universe $\Omega_0 > 1$ and for a negatively curved Universe $\Omega_0 < 1$.

The value of the curvature radius, $R_{curv} \equiv a/\sqrt{|k|}$, is given by

$$R_{curv} = \frac{H_0^{-1}}{\sqrt{|\Omega_0 - 1|}}, \tag{2.21}$$

then its characteristic scale or Hubble radius is given by $H_0^{-1} \approx 3000 h^{-1}$ Mpc.

2.1.1 Observational toolkit

In observational cosmology one of the fundamental observables is the redshift, and therefore it is important to express the distance relations in terms of z. The first distance measure to be considered is the lookback time, i.e. the difference between the age of the Universe at observation t_0 and the age of the Universe when the photons were emitted t. From the definitions of redshift, eq.(2.2), and the Hubble parameter, eq.(2.5), we have:

$$\frac{dz}{dt} = -\frac{\dot{a}}{a^2} = -H(z)(1+z) ,$$

from which we have:

$$dt = -\frac{dz}{H(z)(1+z)} , \tag{2.22}$$

and the lookback time is defined as:

$$t_0 - t = \int_t^{t_0} dt = \int_0^z \frac{dz'}{H(z')(1+z')} = \frac{1}{H_0} \int_0^z \frac{dz'}{(1+z')E(z')} , \tag{2.23}$$

where

$$E(z) = \sqrt{\Omega_r(1+z)^4 + \Omega_m(1+z)^3 + \Omega_k(1+z)^2 + \Omega_w \exp\left(3\int_0^z \frac{1+w(x)}{1+x}dx\right)} . \tag{2.24}$$

From the definition of lookback time it is clear that the cosmological time or time back to the Big Bang, is given by

$$t(z) = \int_z^\infty \frac{dz'}{(1+z')H(z')} . \tag{2.25}$$

In the following discussion it will be useful to have an adequate parameterization of the FRW metric (Hobson et al., 2005) which is given by:

$$ds^2 = dt^2 - a^2(t) \left[d\chi^2 + S^2(\chi)(d\theta^2 + \sin^2\theta d\phi^2) \right] ,$$

where the function $r = S(\chi)$ is:

$$S(\chi) = \begin{cases} \sqrt{k}^{-1} \sin(\chi\sqrt{k}) & \text{if } k > 0, \\ \chi & \text{if } k = 0, \\ \sqrt{|k|}^{-1} \sinh(\chi\sqrt{|k|}) & \text{if } k < 0, \end{cases} \tag{2.26}$$

We can see that the comoving distance, i.e., that between two free falling particles which remains constant with epoch, is defined by:

$$\chi = \int_t^{t_0} \frac{dt}{a(t)} = \frac{1}{H_0} \int_0^z \frac{dz'}{E(z')} \ . \tag{2.27}$$

The transverse comoving distance (also called proper distance) is defined as:

$$D_M(t) = a(t)S(\chi), \tag{2.28}$$

At the present time and for the case of a flat model we have, $D_M = a(t_0)\chi = \chi$.

The angular distance is defined as the ratio of an object's physical transverse size to its angular size, and can be expressed as:

$$D_A = \frac{D_M}{1+z} \ . \tag{2.29}$$

Finally, the luminosity distance is defined by means of the relation

$$f = \frac{L}{4\pi D_L^2}, \tag{2.30}$$

where f is an observed flux, L is the intrinsic luminosity of the observed object and D_L is the luminosity distance; from which one obtains:

$$D_L = (1+z)D_M = (1+z) \int_0^z \frac{dz'}{H(z')} \ . \tag{2.31}$$

The distance modulus of a given cosmic object is defined as:

$$\mu \equiv m - M = 5\log_{10}(D_L/10 \text{ pc}) \tag{2.32}$$

where m and M is the apparent and absolute magnitude of the object, respectively. If the distance, D_L, is expressed in Mpc then we have:

$$\mu = 5\log_{10} D_L + 25 \ . \tag{2.33}$$

Through this relation and with the use of standard candles, i.e. objects of fixed absolute magnitude M, we can constrain the different parameters of the cosmological models via the construction of the Hubble diagram (the magnitude-redshift relation).

The scale factor can be Taylor expanded around its present value:

$$
\begin{aligned}
a(t) &= a(t_0) - (t_0 - t)\dot{a}(t_0) + \frac{1}{2}(t_0 - t)^2\ddot{a}(t_0) - \cdots \\
&= a(t_0)[1 - (t_0 - t)H(t_0) - \frac{1}{2}(t_0 - t)^2 q(t_0)H^2(t_0) - \cdots] \\
&= 1 + H_0(t - t_0) - \frac{1}{2}q_0 H_0^2(t - t_0)^2 + \cdots ,
\end{aligned}
$$

where the deceleration parameter $q(t)$ is given by

$$
q(t) \equiv -\frac{\ddot{a}(t)a(t)}{\dot{a}^2(t)} .
\tag{2.34}
$$

From the previous definitions we can write the distance-redshift relation as

$$
H_0 D_L = z + \frac{1}{2}(1 - q_0)z^2 + \cdots ,
\tag{2.35}
$$

where we can recognize that for $z \ll 1$ it can be written as

$$
H_0 D_L \approx z,
\tag{2.36}
$$

which is known as the "Hubble law".

Finally the comoving volume element, as a function of redshift, can be written as:

$$
\frac{dV}{dz d\Omega} = \frac{S^2(\chi)}{H(z)} ,
\tag{2.37}
$$

where Ω is the solid angle.

2.1.2 Growth of structure

The accelerated expansion of the Universe affects the evolution of cosmic structures since the expansion rate influences the growth rate of the density perturbations.

The basic assumptions regarding the evolution of structure in the Universe are that the dark matter is composed of non relativistic particles, i.e it is composed of what is called cold dark matter (CDM), and that the initial spectrum of density perturbations is nearly scale invariant, $P(k) \sim k^{n_s}$, where the spectral index is $n_s \simeq 1$, as it is predicted by inflation. With this in mind, the growth of small amplitude, matter density perturbations on length scales much smaller than the Hubble radius is governed by a

second order differential equation, constructed by linearizing the perturbed equations of motions of a cosmic fluid element and given by:

$$\ddot{\delta}_k + 2H\dot{\delta}_k - 4\pi G\rho_m \delta_k = 0, \tag{2.38}$$

where the perturbations $\delta_k \equiv \delta\rho_m(\mathbf{x}, t)/\bar{\rho}_m(t)$ have been decomposed into their Fourier modes of wave number k. The expansion of the Universe enters through the so-called "Hubble drag" term, $2H\dot{\delta}_k$. Note that $\bar{\rho}_m$ is the mean density.

The growing mode solution of the previous differential equation, in the standard *concordance* cosmological model ($w_\Lambda = -1$) is given by:

$$\delta_k(z) \propto H(z)(5\Omega_m/2) \int_z^\infty \frac{1+z'}{H^3(z')} dz' . \tag{2.39}$$

From the previous equation we obtain that $\delta_k(t)$ is approximately constant during the radiation dominated epoch, grows as $a(t)$ during the matter dominated epoch and again is constant during the cosmic acceleration dominated epoch, in which the growth of linear perturbations effectively freezes when the cosmic acceleration dominates.

2.2 Empirical Evidence

The cosmic acceleration was established empirically at the end of the 1990s when two independent teams, the *Supernova Cosmology Project* and the *High-z Supernova Search*, succeeded in their attempt to measure the supernova Hubble diagram up to relatively high redshifts ($z \sim 1$) (Riess et al., 1998; Perlmutter et al., 1999). Surprisingly, both teams found that the distant supernovae are $\sim 0.25 \, \mathrm{mag}$ dimmer that they would be in a decelerating universe, indicating that the cosmic expansion has been accelerating over the past $\sim 7 \, \mathrm{Gyr}$ (see Figure 2.1).

The cosmic acceleration has been verified by many other probes, and in this section we will briefly review the current evidence on which this picture of the Universe was constructed.

2.2.1 Cosmic microwave background

The measurement of the CMB black body spectrum was one of the most important tests of the big bang cosmology. The CMB spectrum started being studied by means of bal-
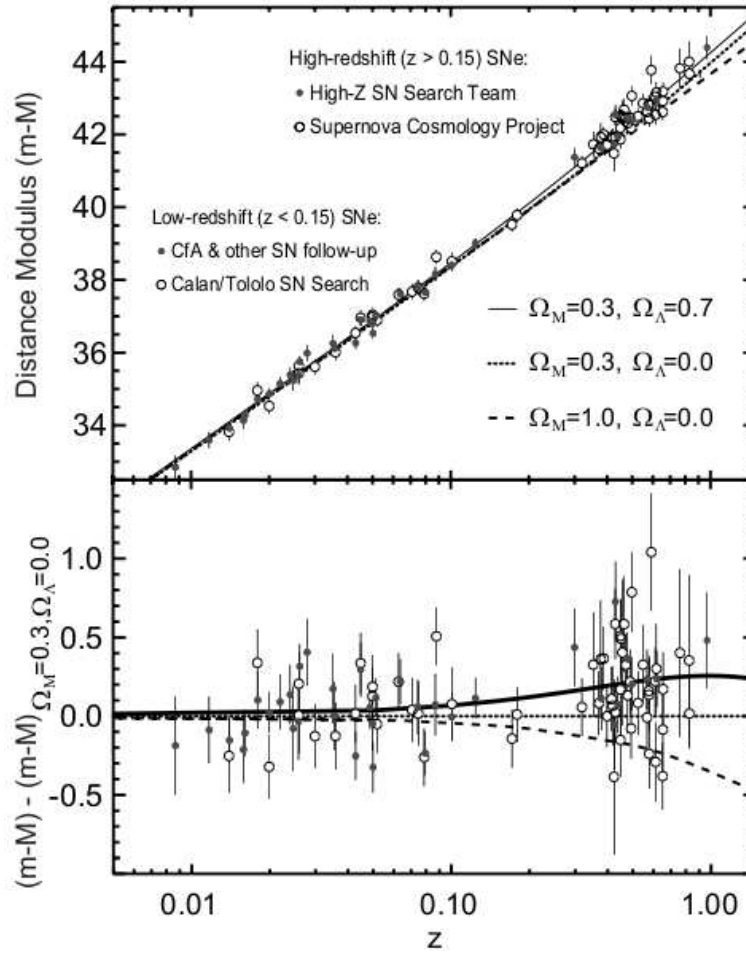
Figure 2.1: *Upper panel:* Hubble diagram of type Ia supernovae measured by the Supernova Cosmology Project and the High-z Supernova Team. *Lower Panel:* Residuals in distance modulus relative to an open Universe with $\Omega_0 = \Omega_m = 0.3$. Taken from Perlmutter & Schmidt (2003).

loon and rocket borne observations and finally the black body shape of the spectrum was settled in the 1990s by observations with the FIRAS radiometer at the Cosmic Background Explorer Satellite (COBE) (Mather et al., 1990), which also showed that the departures from a pure blackbody were extremely small ($\delta E/E \leq 10^{-4}$) (Fixsen et al., 1996).

The CMB anisotropies provide a vision of the Universe when photons decoupled from baryons and before structure developed, about 380000 years after the Big Bang. The angular power spectrum of the CMB temperature anisotropies is dominated by acoustic peaks that arise from gravity-driven sound waves in the photon-baryon fluid.
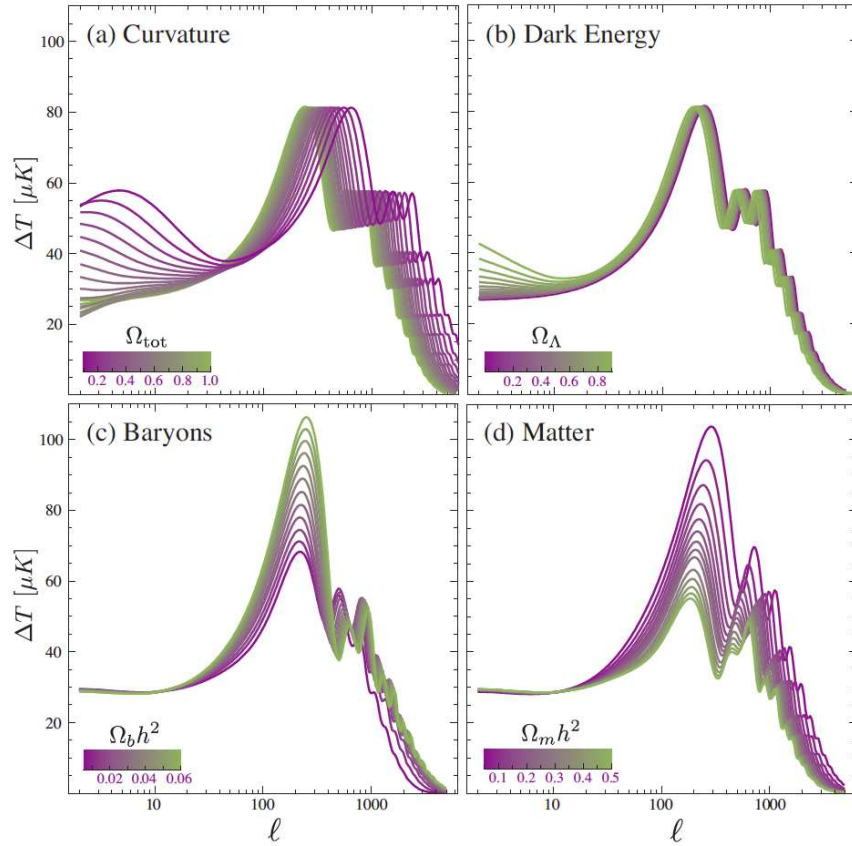
Figure 2.2: Sensitivity of the acoustic temperature spectrum to four fundamental cosmological parameters. (a) The curvature as quantified by Ω_0. (b) The dark energy as quantified by the cosmological constant Ω_Λ ($w_\Lambda = -1$). (c) The baryon density $\Omega_b h^2$. (d) The matter density $\Omega_m h^2$. All parameters are varied around a fiducial model with: $\Omega_0 = 1, \Omega_\Lambda = 0.65, \Omega_b h^2 = 0.02, \Omega_m h^2 = 0.147, n = 1, z_{ri} = 0, E_i = 0$. Taken from Hu & Dodelson (2002).

The position and amplitudes of the acoustic peaks indicate that the Universe is nearly spatially flat (see Figure 2.2). Furthermore, in combination with Large Scale Structure (LSS) or independent H_0 measurements, it shows that the matter contributes only about 25% of the critical energy density (Hu & Dodelson, 2002). Clearly, a component of missing energy is necessary to match both results, a fact which is fully consistent with the dark energy being an explanation of the accelerated expansion.

Measurements of the angular power spectrum of the CMB have been carried out in the last ten years by many experiments [e.g., Jaffe et al. (2001); Pryke et al. (2002); Spergel et al. (2007); Reichardt et al. (2009)]. Figure 2.3 shows a combination of some recent results where the first acoustic peak around $l = 200$ is clearly seen, which con-
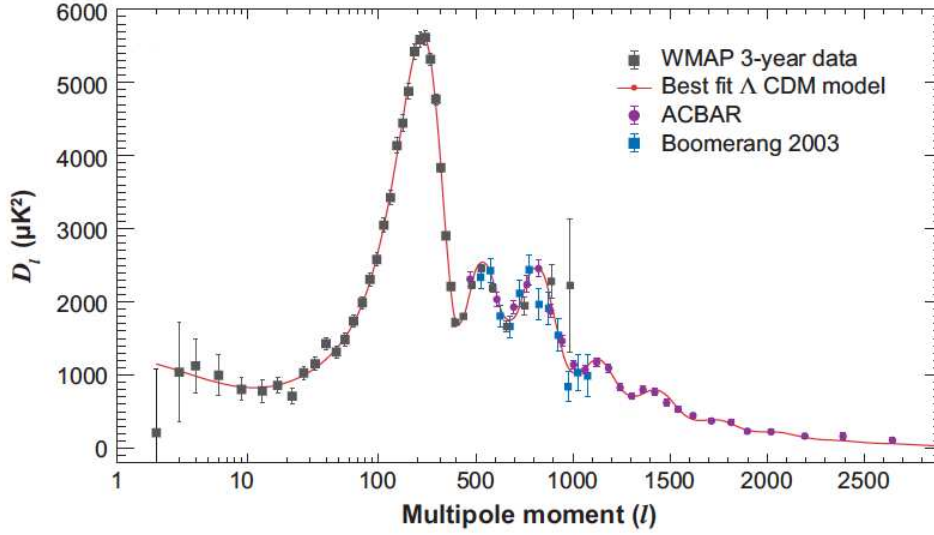
Figure 2.3: Angular power spectrum measurements of the cosmic microwave background temperature fluctuations form the Wilkinson Microwave Anisotropy Probe (WMAP), Boomerang, and the Arcminute Cosmology Bolometer Array Receiver (ACBAR). Taken from Frieman et al. (2008).

strain the spatial curvature of the universe to be very close to null. Although all these results are consistent with an accelerating expansion of the universe, they alone are not conclusive; other cosmological data, like the measurements of the Hubble constant, are necessary in order to indicate the cosmic acceleration.

2.2.2 Large-scale structure

The two-point correlation function of galaxies, as a measure of distribution of galaxies on large scales, has long been used to provide constrains on various cosmological parameters. The measurement of the correlation function of galaxies from the APM survey excluded, at that time, the standard cold dark matter (CDM) picture (Maddox et al., 1990) and subsequently argued in favor of a model with a low density CDM and possibly a cosmological constant (Efstathiou et al., 1990).

The baryonic acoustic oscillations (BAO) leave a characteristic signature in the clustering of galaxies, a bump in the two-point correlation function at a scale $\sim 100h^{-1}\,\mathrm{Mpc}$ that can be measured today. Measurements of the BAO signature have been carried out by Eisenstein et al. (2005) for luminous red galaxies of the Sloan Digital Sky Survey
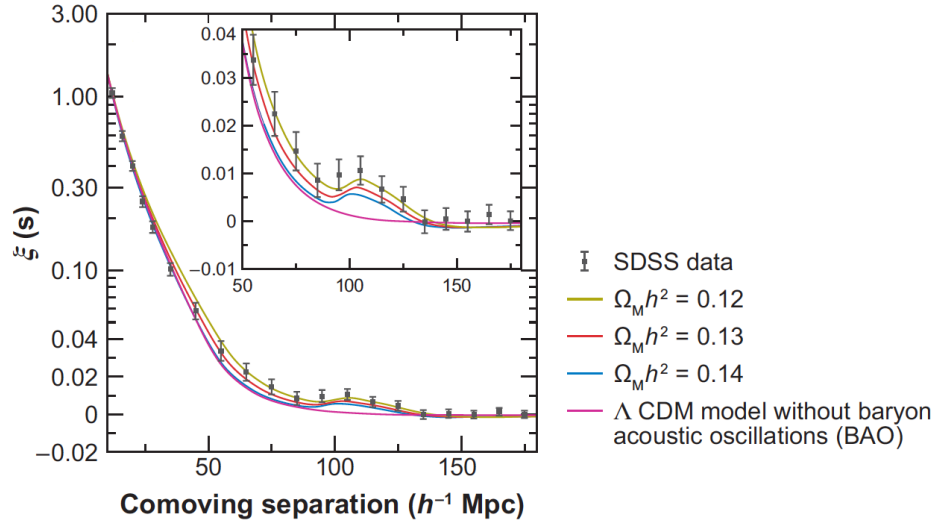
Figure 2.4: Detection of the baryon acoustic peak in the clustering of luminous red galaxies in the Sloan Digital Sky Survey (Eisenstein et al., 2005). The two-point galaxy correlation function in redshift space is shown; the inset shows an expanded view with a linear vertical axis. Curves correspond to the ΛCDM predictions for $\Omega_m h^2 = 0.12$ (dark yellow), 0.13 (red), and 0.14 (blue). The magenta curve shows a ΛCDM model without baryonic acoustic oscillations. Taken from Frieman et al. (2008).

(SDSS). They find results for the value of $\Omega_m h^2$ and the acoustic peak at $100h^{-1}$ Mpc scale which are consistent with the outcome of the CMB fluctuation analyses (see Figure 2.4).

2.2.3 Current supernovae results

After the first SNe Ia results were published, concerns were raised about the possibility that intergalactic extinction or evolutionary effects could be the cause of the observed distant supernovae dimming (Aguirre, 1999; Drell et al., 2000). Since then a number of surveys have been conducted which have strengthened the evidence for cosmic acceleration. Observations have been conducted with the Hubble Space Telescope (HST), which have provided high quality light curves (Riess et al., 2007), and with ground based telescopes, which have permitted the construction of two large surveys, based on 4 meter class telescopes, the SNLS (Supernova Legacy Survey) (Astier et al., 2006) and the ESSENCE (Equation of State: Supernovae Trace Cosmic Expansion) survey (Miknaitis et al., 2007) with spectroscopic follow ups on larger telescopes.
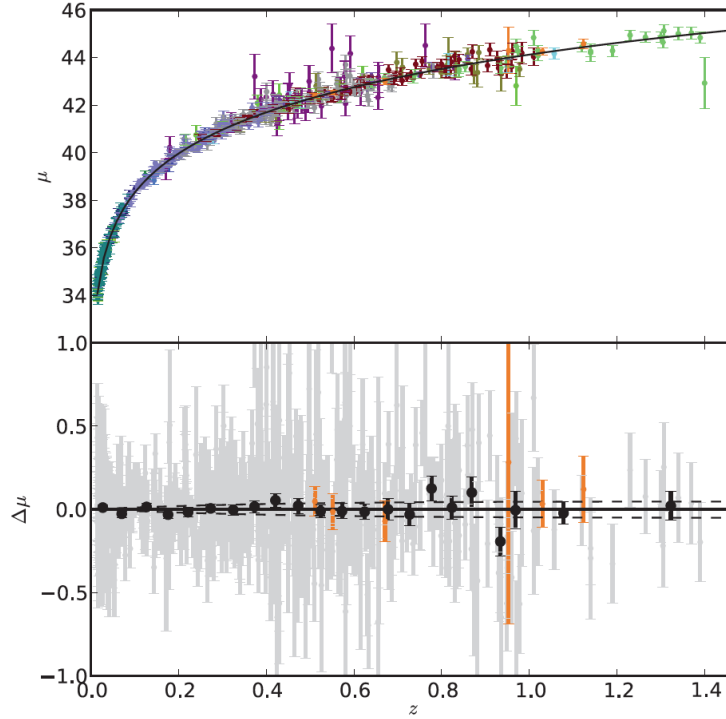
Figure 2.5: *Upper panel:* Hubble diagram for the *Union2* SNe Ia compilation. The solid line represents the best fitted cosmology for a flat Universe including CMB and BAO constraints. The different colors indicate the different data. *Lower panel:* Hubble diagram residuals were the best fitted cosmology has been subtracted from the light curve shape and color corrected peak magnitudes. The gray points show the residuals for individual SNe, while the black points show the binned values in redshifts bins of 0.05 for $z < 1.0$ and 0.2 for $z > 1.0$. The dashed lines show the expected Hubble diagram residuals for cosmological models with $w \pm 0.1$ from the best fitted value. Taken from Amanullah et al. (2010).

The SNe Ia Hubble diagram has been constantly improved by the addition of new data, from the above mentioned surveys, mostly at $z < 1.0$. Amanullah et al. (2010) have succeeded in analyzing the current SNe Ia data (557 objects) homogeneously and have taken care of known systematics, forming what has been named the *Union2* compilation. Figure 2.5 shows the Hubble diagram based on the *Union2* dataset, where the solid line represents the best fitted cosmology, obtained from an iterative χ^2-minimization procedure based on:

$$\chi^2 = \sum_{\text{SNe}} \frac{[\mu_B(\alpha, \beta, M_B) - \mu(z; \Omega_m, \Omega_w, w)]^2}{\sigma_{\text{ext}}^2 + \sigma_{\text{sys}}^2 + \sigma_{\text{lc}}^2} \, , \tag{2.40}$$

where σ_{lc} is the propagated error of the covariance matrix of the light curve fit, whereas, σ_{ext} and σ_{sys} are the uncertainties associated with the Galactic extinction correction,
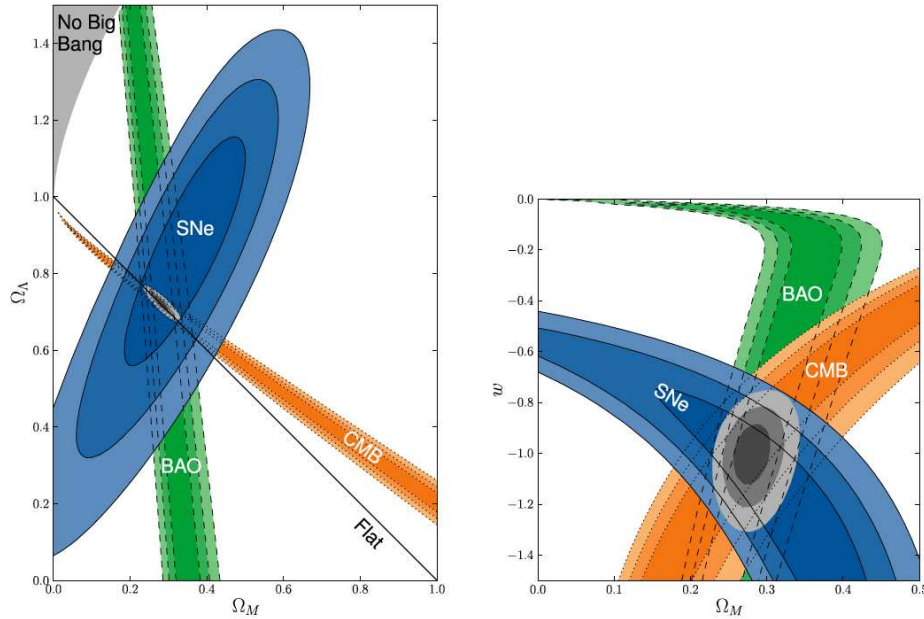
Figure 2.6: *Left panel:* 68.3 %, 95.4 % and 99.7% confidence regions in the $(\Omega_m, \Omega_\Lambda)$ plane from SNe, BAO and CMB with systematic errors. Cosmological constant dark energy ($w = -1$) has been assumed. *Right panel:* 68.3 %, 95.4 % and 99.7% confidence regions in the (Ω_m, w) plane from SNe, BAO and CMB with systematic errors. Zero curvature and constant w has been assumed. Taken from Amanullah et al. (2010).

host galaxy peculiar velocity and gravitational lensing, the former, and potential systematic errors the later. The observed distance modulus is defined as $\mu_B = m_B^{\mathrm{corr}} - M_B$, where M_B is the absolute B-band magnitude and $m_B^{\mathrm{corr}} = m_B^{\mathrm{max}} + \alpha x_1 - \beta c$; furthermore m_B^{max}, x_1 and c are parameters for each supernova that are weighted by the *nuisance* parameters α, β and M_B which are fitted simultaneously with the cosmological parameters $(z; \Omega_m, \Omega_w, w)$ which give the model distance modulus μ.

Combining the data from the three probes that have been considered up to now, it is possible to obtain stronger constraints over the cosmological parameters (see Figure 2.6). Table 2.1 shows the fitted cosmological parameters from using jointly the SNe Ia, BAO and CMB cosmological data.

2.3 Theoretical Landscape

The cosmic accelerated expansion has deep consequences for our understanding of the physical world. From the theoretical side many plausible explanations have been pro-

Table 2.1: χ^2 minimization results of cosmological parameters Ω_m, w and Ω_k and their uncertainties. Adapted from Amanullah et al. (2010).

Fit	Ω_m	Ω_k	w
SNe	$0.274^{+0.040}_{-0.037}$	0 (fixed)	-1 (fixed)
SNe + BAO + CMB	$0.281^{+0.018}_{-0.016}$	$-0.004^{+0.006}_{-0.007}$	-1 (fixed)
SNe + BAO + CMB	$0.281^{+0.018}_{-0.016}$	$-0.006^{+0.008}_{-0.007}$	$-1.035^{+0.093}_{-0.097}$

posed. The "simplest" one is the traditional cosmological constant, but as we will see, this solution presents serious theoretical inconsistencies. To alleviate these problems various solutions have been proposed which involve either the introduction of an exotic fluid, with negative pressure, the dynamical consequences of which evolve with time (here we call them Dark Energy theories) or a modification of general relativity.

2.3.1 The cosmological constant

The Cosmological Constant, Λ, was introduced by Einstein in his field equations, in order to obtain a static solution. It is possible since the Einstein tensor, $G^{\mu\nu} = R^{\mu\nu} - 1/2g^{\mu\nu}R$, satisfies the Bianchi identities $\nabla_\nu G^{\mu\nu} = 0$ and the energy momentum tensor, $T^{\mu\nu}$, satisfies energy conservation $\nabla_\nu T^{\mu\nu} = 0$; furthermore the metric, $g^{\mu\nu}$, is invariant to covariant derivatives $\nabla_\alpha g^{\mu\nu} = 0$; then there is a freedom to add a constant term to the GR equations:

$$R_{\mu\nu} - \frac{1}{2}g_{\mu\nu}R + \Lambda g_{\mu\nu} = 8\pi G T_{\mu\nu} , \tag{2.41}$$

from which we can obtain equations (2.3) and (2.4):

$$\left(\frac{\dot{a}}{a}\right)^2 = \frac{8\pi G\rho}{3} - \frac{k}{a^2} + \frac{\Lambda}{3} ,$$
$$\frac{\ddot{a}}{a} = -\frac{4\pi G}{3}(\rho + 3p) + \frac{\Lambda}{3} .$$

Form the first of these equations we can see that:

$$\rho_\Lambda = \frac{\Lambda}{8\pi G} , \tag{2.42}$$

and combining the above with eq.(2.4), we can see that $p_\Lambda = -\rho_\Lambda$. As an approximation, in the case in which the energy density of the cosmological constant dominates

the dynamics of the Universe, and neglecting the matter component, we have that:

$$\frac{\ddot{a}}{a} = -\frac{4\pi G}{3}(\rho_\Lambda + 3p_\Lambda)$$
$$= \frac{8\pi G}{3}\rho_\Lambda .$$

From this rough argument, it becomes evident how the cosmological constant explains the phenomenology of the accelerated cosmic expansion, since it is clear that we have $\ddot{a} \propto \rho_\Lambda a$.

From the previous argument we see that for a cosmological constant we have $w = -1$. It is interesting to note that the current high-quality cosmological data strongly suggest that the mechanism behind the cosmic acceleration is no other than the cosmological constant. However, we will show that this explanation of the accelerating universe presents serious theoretical inconsistencies.

From the point of view of modern field theories, the cosmological constant can be explained as the energy of the vacuum. The possible sources for the vacuum energy are basically of two kinds: a bare cosmological constant in the general relativity action or the energy density of the quantum vacuum.

A bare cosmological constant (Λ_0) can be added in the general relativity action:

$$S = \frac{1}{16\pi G} \int d^4x \sqrt{-g}(R - 2\Lambda_0) . \tag{2.43}$$

In fact this is the most general covariant action that we can construct from the metric and its first and second derivatives; we obtain eq.(2.41) varying this action with the addition of matter terms. In this case the effective cosmological constant is the sum of the bare term and a potential energy.

The energy density of the quantum vacuum arises from the fact that for each mode of the quantum field there is a zero-point energy $\hbar\omega/2$. Formally the total energy would be infinite unless we discard the very high momentum modes on the ground that we trust the theory only to a certain ultraviolet momentum cutoff k_{max}, then we have

$$\rho_\Lambda = \frac{1}{2}\sum_{fields} g_i \int_0^\infty \frac{d^3k}{(2\pi)^3}\sqrt{k^2 + m^2} \simeq \sum_{fields}\frac{g_i k_{max}^4}{16\pi^2}, \tag{2.44}$$

21

where g_i accounts for the degrees of freedom of the field (its sign is $+$ for bosons and $-$ for fermions). From the last equation we can see that $\rho_\Lambda \sim k_{max}^4$, then imposing as a cutoff the energies where the known symmetry breaks, we have that:

- In the case of the electroweak symmetry braking, the potential is $M_{EW} \sim 200\,\text{GeV}$ (1 GeV $= 1.6 \times 10^{-3}$ erg) and then the contribution to the vacuum energy is $\rho_\Lambda^{EW} \sim (200\,\text{GeV})^4 \sim 3 \times 10^{47}$ erg/cm^3.

- The potential arising from the breaking of chiral symmetry is due to the nonzero expectation value of the quark bilinear $q\bar{q}$ with a potential $M_{QCD} \sim 0.3$ GeV and then its contribution to the vacuum energy is $\rho_\Lambda^{QCD} \sim (0.3\,\text{GeV})^4 \sim 1.6 \times 10^{36}$ erg/cm^3.

- For the Planck scale transition we have a potential $M_{Pl} = (8\pi G)^{-1/2} \sim 10^{18}$ GeV and then its contribution to the vacuum energy is $\rho_\Lambda^{Pl} \sim (10^{18}\,\text{GeV})^4 \sim 2 \times 10^{110}$ erg/cm^3.

The previously mentioned theoretical inconsistency arises from the fact that, while quantum field theory predicts a vacuum energy density which has a value $10^{36} \lesssim \rho_\Lambda \lesssim 10^{110}$ erg/cm^3, the cosmological observations provide a value:

$$|\rho_\Lambda^{obs}| \leq (10^{-12}\,\text{GeV})^4 \sim 2 \times 10^{-10}\ \text{erg/cm}^3\ , \tag{2.45}$$

which is $10^{46} - 10^{120}$ times smaller than any theoretical prediction. This serious inconsistency between the observed value and the quantum field theory expectations (Carroll, 2001) has been dubbed *the cosmological constant problem* or *the fine tuning problem* and has a long history (Weinberg, 1989).

2.3.2 Dark energy theories

An alternative cause of the accelerated cosmic expansion, which possibly avoids the *cosmological constant problem*, could be a dynamic dark energy with the value of its equation of state parameter, w, changing with the redshift. In such an approach the vacuum energy, arising from quantum field theories, could have a value exactly equal to zero due to some mechanism, modeled theoretically by the renormalization procedure, that cancels it.

The dark energy approach as an explanation of the accelerated expansion could have a new field as its origin. The simplest such field is a scalar one and it has been named *quintessence*. The action for this model is given by

$$S = \int d^4x \sqrt{-g} \left(\frac{R}{16\pi G} + \mathcal{L}_{SM} + \mathcal{L}_Q \right) , \tag{2.46}$$

where R is the Ricci scalar, g is the determinant of the metric, $\mathcal{L}_{SM}$ is the Lagrangian for Standard Model particles and the quintessence Lagrangian is given by

$$\mathcal{L}_Q = -\frac{1}{2}(\nabla_\mu Q)(\nabla^\mu Q) - V(Q) . \tag{2.47}$$

The field obeys the Klein-Gordon equation:

$$\Box Q = V_{,Q}; \tag{2.48}$$

and its stress-energy tensor is given by

$$T_{\mu\nu} = (\nabla_\mu Q)(\nabla_\nu Q) + g_{\mu\nu}\mathcal{L}_Q . \tag{2.49}$$

The scalar field obeys the equation of motion:

$$\ddot{Q} + 3H\dot{Q} + V_{,Q} = 0 \tag{2.50}$$

with energy density and pressure given by:

$$\rho_Q = \frac{1}{2}\dot{Q}^2 + V(Q), \qquad\qquad p_Q = \frac{1}{2}\dot{Q}^2 - V(Q) . \tag{2.51}$$

Then its equation of state parameter, $w = p/\rho$, is given by:

$$w = \frac{\dot{Q}^2/2 - V(Q)}{\dot{Q}^2/2 + V(Q)} = \frac{-1 + \dot{Q}^2/2V}{1 + \dot{Q}^2/2V} , \tag{2.52}$$

from which it is obvious that if the evolution of the field is slow, we have $\dot{Q}^2/2V \ll 1$, and the field behaves like a slowly varying vacuum energy, with $w < 0$, $\rho_Q(t) \propto V[Q(t)]$ and $p_Q(t) \propto -V[Q(t)]$.

2.3.3 Modified gravity theories

As it was mentioned earlier, an alternative explanation of the cosmic acceleration is through a modification to the laws of gravity. This implies a modification to the geometry side of the GR field equations, instead of the modification of the stress-energy tensor. Many ideas have been explored in this direction, some of them based on models motivated by higher-dimensional theories and string theory [eg., Dvali et al. (2000); Deffayet (2001)] and others as phenomenological modifications to the Einstein-Hilbert action of GR [eg., Carroll et al. (2004); Song et al. (2007)].

2.4 Probes of Cosmic Acceleration

The accelerated expansion of the Universe appears to be a well established fact, while the dark energy density has been determined apparently to a precision of a few percent. However, measuring its equation of state parameter and determining if it is time-varying is a significantly more difficult task. The primary consequence of dark energy is its effect on the expansion rate of the universe and thus on the redshift-distance relation and on the growth-rate of cosmic structures. Therefore, we have basically two kinds of probes for dark energy, one geometrical and the other one based on the rate of growth of density perturbations.

The *Growth* probes are related to the rate of growth of matter density perturbations, a typical example being the spatial clustering of extragalactic sources and its evolution. The *Geometrical* probes are related directly to the metric, a typical example being the redshift-distance relation as traced by SNe Ia.

In general, in order to use the latter probes, based on any kind of tracers, one has to measure the redshift which is relatively straightforward, but also the tracer distance, which in general is quite difficult. In Appendix C we review the cosmic distance ladder which allows the determination of distances to remote sources.

2.4.1 Type Ia supernovae

Type Ia Supernovae have been used as geometrical probes, since they are standard candles (Leibundgut, 2001), and through their determination of the Hubble function

have provided constrains of cosmological parameters through eq.(2.32). Up to date they are the most effective, and better understood, probe of the cosmic acceleration (Frieman et al., 2008).

The standardization of SNe Ia became possible after the work of Phillips (1993) where an empirical correlation was established between their peak brightness and the luminosity decline rate, after peak luminosity (in the sense that more luminous SNe Ia decline more slowly).

The principal systematics in the distance determination derived from SNe Ia, are errors in host galaxy extinction correction and uncertainties in SNe Ia intrinsic colors, luminosity evolution and selection bias in the low redshift samples (Frieman et al., 2008). The extinction correction is particularly difficult since having the combination of photometric errors, variation in intrinsic colors and host galaxy dust properties causes distance uncertainties even when using multiband observations. However, a promising solution of this problem is based on near infrared observations, where the extinction effects are significantly reduced.

Frieman et al. (2003) estimated that in order to obtain precise measurements of w_0 and w_1, accounting for SNe Ia systematics, requires ~ 3000 light curves out to $z \sim 1.5$, measured with great precision and careful control of the systematics.

2.4.2 Galaxy clusters

The utility of galaxy clusters as cosmological probes relies in many aspects, among which is the determination of their mass to light ratio, a comparison of which with the corresponding cosmic ratio can provide the value of Ω_m [eg., Andernach et al. (2005)], the cluster masses can be also used to derive the cluster mass function to be compared with the analytic (Press-Schechter) or numerical (N-body simulations) model expectations (Basilakos et al., 2009; Haiman et al., 2001; Warren et al., 2006). The determination of the cluster mass can be done by means of the relation between mass any other observable, such as X-ray luminosity or temperature, cluster galaxy richness, Sunyaev-Zel'dovich effect (SZE) flux decrement or weak lensing shear, etc (Frieman et al., 2008).

Frieman et al. (2008) gives the redshift distribution of clusters selected according to some observable O, with selection function $f(O, z)$ as

$$\frac{d^2 N(z)}{dz d\Omega} = \frac{r^2(z)}{H(z)} \int_0^\infty f(O, z) dO \int_0^\infty p(O|M, z) \frac{dn(z)}{dM} dM ,\qquad (2.53)$$

where $dn(z)/dM$ is the space density of dark halos in comoving coordinates and $p(O|M, z)$ is the mass-observable relation, the probability that a halo of mass M, at redshift z, is observed as a cluster with observable property O. We can see that this last equation depends on the cosmological parameters through the comoving volume element (see equation (2.37)) and the term $dn(z)/dM$ which depends on the evolution of density perturbations.

2.4.3   Baryon acoustic oscillations

Gravity drives acoustic oscillations of the coupled photon-baryon fluid in the early universe. The scale of the oscillations is given by

$$s = \int_0^{t_{rec}} c_s(1 + z) dt = \int_{z_{rec}}^\infty \frac{c_s}{H(z)} dz,\qquad (2.54)$$

where c_s is the sound speed which is determined by the ratio of the baryon and photon energy densities, whereas t_{rec} and z_{rec} are the time and redshift when recombination occurred. These acoustic oscillations leave their inprint on the CMB temperature anisotropy angular power spectrum and in the baryon mass-density distribution. From the WMAP measurements we have $s = 147 \pm 2$ Mpc. Since the oscillations scale s provides a standard ruler that can be calibrated by the CMB anisotropies, then measurements of the BAO scale in the galaxy distribution provides a geometrical probe for cosmic acceleration (Frieman et al., 2008).

The systematics that could affect the BAO measurements are related to nonlinear gravitational evolution effects, scale-dependent differences between the clustering of galaxies and of dark matter (the so-called bias) and redshift-space distortions of the clustering, which can shift the BAO features (Frieman et al., 2008).

2.4.4 Weak gravitational lensing

The images of distant galaxies are distorted by the gravitational potential of foreground collapsed structures, intervening in the line of sight of the distant galaxies. This distortion can be used to measure the distribution of dark matter of the intervening structures and its evolution with time, hence it provides a probe for the effects of the accelerated expansion on the growth of structure (Frieman et al., 2008).

The gravitational lensing produced by LSS can be analysed statistically by locally averaging the shapes of large numbers of distant galaxies, thus obtaining the so called cosmic shear field at any point. The angular power spectrum of shear is a statistical measure of the power spectrum of density perturbations, and is given by (Hu & Jain, 2004)

$$P_l^\gamma(z_s) = \int_0^{z_s} dz \frac{H(z)}{D_A^2(z)} |W(z, z_s)|^2 P_\rho \left(k = \frac{l}{D_A(z)}; z \right), \qquad (2.55)$$

where l is the angular multipole, $W(z, z_s)$ is the lensing efficiency of a population of source galaxies and it is determined by the distance distributions of the source and lens galaxies, and $P_\rho(k, z)$ is the power spectrum of density perturbations.

Some systematics that could affect weak lensing measurements are, obviously, incorrect shear estimates, uncertainties in the galaxy photometric redshift estimates (which are commonly used), intrinsic correlations of galaxy shapes and theoretical uncertainties in the mass power spectrum on small scales (Frieman et al., 2008).

2.4.5 H II galaxies

H II galaxies are dwarf galaxies with a strong burst of star formation which dominates the luminosity of the object and allows it to be seen at very large distances. The $L(\text{H}\beta) - \sigma$ relation of H II galaxies allows distance modulus determination for these objects and therefore the construction of the Hubble diagrams. Hence, H II galaxies can be used as geometrical probes of the cosmic acceleration.

Previous analyses (Terlevich & Melnick, 1981; Melnick et al., 1987), have shown that the H II galaxies oxygen abundance affects systematically its $L(\text{H}\beta) - \sigma$ relation. The distance indicator proposed by the authors takes into account such effects

(Melnick et al., 1988), and was defined as:

$$M_z = \frac{\sigma^5}{O/H} \, ,$$

(2.56)

where σ is the galaxy velocity dispersion and O/H is the oxygen abundance relative to hydrogen. From this distance indicator, the distance modulus can be calculated as: (Melnick et al., 2000)

$$\mu = 2.5 \log_{10} \frac{\sigma^5}{F(H\beta)} - 2.5 \log_{10}(O/H) - A_{H\beta} - 26.44,$$

(2.57)

where $F(H\beta)$ is the observed $H\beta$ flux and $A_{H\beta}$ is the total extinction in $H\beta$.

Some possible systematics that could affect the $L(H\beta) - \sigma$ relation, are related to the reddening, the age of the stellar burst, as well as the local environment and morphology.

Through the next chapter we will explore carefully the use of H II galaxies as tracers of the Hubble function and the systematics that could arise when calibrating the $L(H\beta) - \sigma$ relation for these objects.

Chapter 3

H II Galaxies as Distance Indicators

In the search for white dwarfs, Humason & Zwicky (1947), using the 18-inch Schmidt telescope at Palomar, developed the technique of using multiply exposed large scale plates, each exposure covering a distinct region of the optical spectrum with the intention of identifying the target objects from the relative intensities in the different plates.

Haro (1956), while searching for emission line galaxies, using the technique pioneered by Humason and Zwicky, discovered some compact galaxies with strong emission lines. Since H II galaxies were easily recognized in objective prism plates, due to their strong narrow emission lines, many were discovered by objective prism surveys during the following years (Markarian, 1967; Zwicky & Zwicky, 1971; Smith et al., 1976; MacAlpine et al., 1977; Markarian et al., 1981).

Some years latter Sargent & Searle (1970) found in the Zwicky & Zwicky (1971) catalogue, some compact galaxies whose spectra were very similar to those of giant H II regions in spiral galaxies. They called them *isolated extragalactic* H II *regions*. After analysing their spectra they conclude that the galaxies are ionized by massive clusters of OB stars (Searle & Sargent, 1972; Bergeron, 1977) and are metal poor systems (Searle & Sargent, 1972; Lequeux et al., 1979; French, 1980; Kunth & Sargent, 1983).

Terlevich & Melnick (1981) and Melnick et al. (1988) analysed the dynamical properties of H II galaxies and proposed their usefulness as distance indicators; the data used for their analysis was published subsequently as a spectrophotometric catalogue (Terlevich et al., 1991) that has been used since in H II galaxies research.

Throughout the first section of the current chapter we will explore the main properties of H II galaxies, then we will discuss their $L(\mathrm{H}\beta) - \sigma$ relation and their possible systematics ending with an analysis of their use as tracers for the dark energy equation of state parameters.

3.1   H II Galaxies Properties

3.1.1   Giant extragalactic H II regions and H II galaxies

One of the defining characteristics of both H II galaxies and Giant Extragalactic H II Regions (GEHRs), is that the turbulent motions of their gaseous components are supersonic (Melnick et al., 1987).

GEHRs are zones of intense star formations in late type spirals (Sc) and irregular galaxies. Ionizing photons are generated by clusters of OB stars at a rate of $10^{51} - 10^{52}$ s^{-1}, ionizing large amounts ($10^4 - 10^6$ M$_\odot$) of low density ($N_e \approx 10 - 100$ cm^{-3}), inhomogeneously distributed gas. GEHRs have typical dimensions of the order $10^2 - 10^3$ pc and diverse morphologies (Shields, 1990; García-Benito, 2009).

H II galaxies are dwarf star forming galaxies that have undergone a recent episode of star formation, their interstellar gas is ionized by one or more massive clusters of OB stars. This type of galaxies have total masses of less than 10^{11} M$_\odot$ and a radius of less than 2 kpc with a surface brightness $\mu_V \geq 19$ mag arcsec^{-2} (García-Benito, 2009).

H II galaxies, being active star forming dwarf galaxies, are also a subset of the blue compact dwarf (BCD) galaxies, although in general the term "H II galaxy" is used when the objects have been selected for their strong, narrow emission lines (Terlevich et al., 1991) while BCD galaxies are selected for their blue colors and compactness. Furthermore, only a fraction of BCDs are dominated by H II regions, being then H II galaxies.

3.1.2   Morphology and structure

H II galaxies are compact objects with high central surface brightness. Telles et al. (1997) have classified H II galaxies in two classes: Type I which have irregular morphology and higher luminosity, and Type II which have symmetric and regular outer

structure. This regular outer structure could indicate large ages since the relaxation time is $\sim 10^8$ yr unless the stars have been formed in an already relaxed gaseous cloud (Kunth & Östlin, 2000).

The determination of the surface brightness profile for H II galaxies has given many apparently contradictory results and both exponential (Telles & Terlevich, 1997) and $r^{1/4}$ (Doublier et al., 1997) models have been claimed as best fit to the data.

The central part of H II galaxies is dominated by one or more knots of star formation giving rise in most cases to excess surface brightness.

3.1.3 Starburst in H II galaxies

H II galaxies have a high star formation rate (Searle & Sargent, 1972). Recent studies have revealed that the recent star formation is concentrated in super star clusters (SSC) with sizes ~ 20 pc (Telles, 2003).

One of the open questions about H II galaxies is the star formation triggering mechanism. Studies of environmental properties of H II galaxies have shown that, in general, these are isolated galaxies (Telles & Terlevich, 1995; Vílchez, 1995; Telles & Maddox, 2000; Campos-Aguilar et al., 1993; Brosch et al., 2004) hence the star formation could not be triggered by tidal interactions with another galaxies. As an alternative, it has been proposed that interaction with other dwarf galaxies or intergalactic H I clouds could be the cause of the star formation in H II galaxies (Taylor, 1997). However, the evidence is not conclusive (Pustilnik et al., 2001).

3.1.4 Ages of H II galaxies

The ages of H II galaxies (and starburst [SB] in general) are estimated from the $H\beta$ equivalent width as was suggested initially by Dottori & Bica (1981). In general two models of star formation time evolution are used:

- An instantaneous SB model, which assumes that all stars are formed at the same time in a short starburst episode, this model is generally applied to individual, low star-mass clusters.

- A continuous SB model, which assumes that the star formation is constant in

time, this model is assumed to be an average characteristic of a system.

Both models are simply the limiting cases for the possible star formation evolution. The second model can be thought of as a localized succession of short duration bursts separated by a small interval of time. Terlevich et al. (2003) showed that a continuous SB model fits better the observations of H II galaxies, which indicates that these are not truly young systems and that they have probably undergone considerable star formation previous to the present burst.

3.1.5 Abundances of H II galaxies
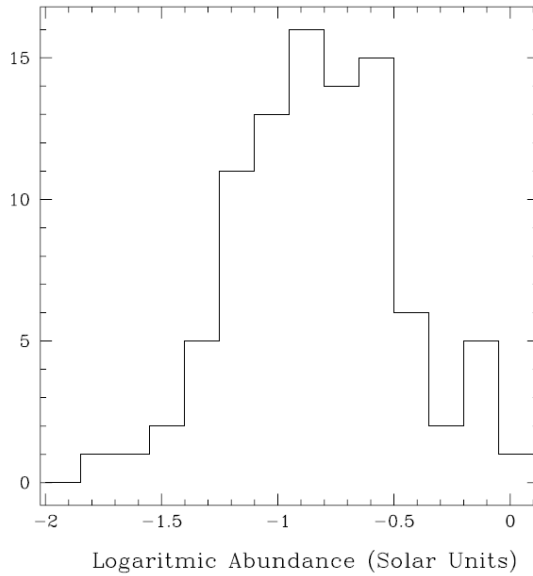
Figure 3.1: The metallicity distribution of H II galaxies from Terlevich et al. (1991), as measured form the oxygen abundances. Taken from Kunth & Östlin (2000).

The metallicity of H II galaxies was first analysed by Searle & Sargent (1972); they showed that oxygen and neon abundances for I Zw18 and II Zw40 were sub-solar. Subsequently, many works have addressed this issue [eg., (Alloin et al., 1978; Lequeux et al., 1979; French, 1980; Kinman & Davidson, 1981; Kunth & Sargent, 1983; Terlevich et al., 1991; Pagel et al., 1992)].

H II galaxies are metal poor systems, the abundance of metals in these systems ranges between $1/2$ Z$_\odot$ and $1/50$ Z$_\odot$. Figure 3.1 shows the oxygen abundances distribution for a sample of Terlevich et al. (1991) H II galaxies.

The oxygen abundance is normally considered as representative of the metallicity of H II galaxies as oxygen is the most abundant of the metals that constitute them. However, the abundances of other elements can be obtained too. Particularly interesting is the fact that since, in general, H II galaxies are chemically unevolved systems, the analysis of helium abundances in these systems is a good method for determining primordial helium abundances.

3.2 The $L(\mathrm{H}\beta) - \sigma$ Relation for H II Galaxies

Melnick (1978) found a correlation between the average turbulent velocity of H II regions in late spirals and irregular galaxies and the parent galaxy absolute magnitude, however at that moment the physics behind the correlation was not clear.

Terlevich & Melnick (1981) analysed the relation between $\mathrm{H}\beta$ luminosity, linewidth, metallicity and size for giant H II regions and H II galaxies finding correlations of the form:

$$luminosity \propto (linewidth)^4$$
$$size \propto (linewidth)^4,$$

which are of the kind encountered in pressure supported systems, then they conclude that H II galaxies (and giant H II regions) are self-gravitating systems in which the observed emission-line profile widths represent the velocity dispersion of discrete gas clouds in the gravitational potential. Furthermore, they found that the scatter in the $L - \sigma$ relation was correlated with metallicity.

Melnick et al. (1987) analysed the properties of GEHRs. They found that the turbulent motions of the gaseous component of those systems are supersonic. Furthermore, they obtain correlations of the form:

$$R_c \sim \sigma^{2.5 \pm 0.5}$$
$$L(\mathrm{H}\beta) \sim \sigma^{5.0 \pm 0.5};$$

and they confirm the correlation between the scatter in the relations and the metallicity (from oxygen abundance). They concluded that the encountered relations were an indication of the virialized nature of discrete gas fragments forming the structure of the

giant H II regions and being ionized by a central star cluster. However, they recognize the possibility that stellar winds could have some then unknown effect on the velocity dispersion of the nebular gas.

Melnick et al. (1988) studied the $L(\mathrm{H}\beta) - \sigma$ relation for H II galaxies in a sample of objects that later would be part of the Spectrophotometric Catalogue of H II Galaxies (Terlevich et al., 1991); they found a relation of the form:

$$\log_{10} L(\mathrm{H}\beta) = (4.70 \pm 0.30) \log_{10} \sigma + (33.61 \pm 0.50) \quad \delta \log_{10} L(\mathrm{H}\beta) = 0.29. \quad (3.1)$$

After a Principal Component Analysis (PCA) for the data, in which the oxygen abundance was used as parameter, they found that the metallicity, $(\mathrm{O/H})$, effectively is an important component of the scatter in the previous relation. Consequently, they propose a distance indicator:

$$M_z = \frac{\sigma^5}{(\mathrm{O/H})}, \qquad (3.2)$$

from which they obtain a new relation

$$\log_{10} L(\mathrm{H}\beta) = (1.0 \pm 0.04) \log_{10} M_z + (41.32 \pm 0.08) \quad \delta \log_{10} L(\mathrm{H}\beta) = 0.271$$
$$(3.3)$$

We must note that this last relation uses the distance scale of Aaronson et al. (1986) $(H_0 \sim 90 \ \mathrm{Km \ s^{-1} \ Mpc^{-1}})$.

Melnick et al. (2000) selected a sample of intermediate redshift $(z < 1)$ H II galaxies from the literature, using as selection criterion the emission lines strength. The objects with strongest emission lines (i.e. largest equivalent widths) were selected in order to avoid the evolved ones (Copetti et al., 1986), which can introduce a systematic error in the $L(\mathrm{H}\beta) - \sigma$ relation due to the effect of the underlying old population over the line widths. Using this sample, they found the $L(\mathrm{H}\beta) - \sigma$ relation shown in Figure 3.2; we can see clearly the effect of the stellar population evolution over the relation. In this work the distance indicator was re-calibrated with the then available distances for the sample. They found

$$\log_{10} L(\mathrm{H}\beta) = \log_{10} M_z + 29.5, \qquad (3.4)$$

from which they derive the distance modulus as

$$\mu = 2.5 \log_{10} \frac{\sigma^5}{F(\mathrm{H}\beta)} - 2.5 \log_{10}(\mathrm{O/H}) - A_{\mathrm{H}\beta} - 26.44, \qquad (3.5)$$
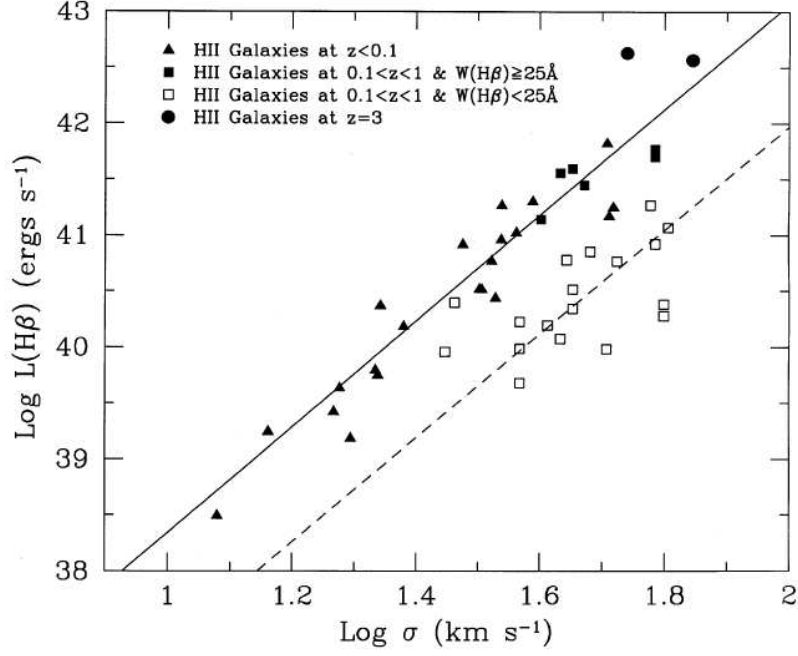
Figure 3.2: The $L(\mathrm{H}\beta) - \sigma$ relation for H II galaxies at intermediate redshifts. The solid line shows the maximum-likelihood fit to the young H II galaxies in the local Universe. The dashed line shows the predicted $L(\mathrm{H}\beta) - \sigma$ relation for an evolved population of H II galaxies. The cosmology is $H_0 = 65 \ \mathrm{km \ s^{-1} \ Mpc^{-1}}$. Taken from Melnick et al. (2000).

where $F(\mathrm{H}\beta)$ is the observed Hβ flux and $A_{\mathrm{H}\beta}$ is the total extinction.

The differential Hubble diagram for H II galaxies derived by Melnick et al. (2000) is shown in Figure 3.3. From the figure it is clear that the data present large scatter. For the local sample ($z < 0.1$), they derived an rms dispersion in distance modulus of $\sigma(\Delta\mu) = 0.52 \ \mathrm{mag}$. Melnick et al. (1988) claim that typical errors are about 10% in flux and 5% in σ, adding 10% in extinction and 20% in abundances, Melnick et al. (2000) expect a scatter of about $0.35 \ \mathrm{mag}$ in μ from observational errors. Hence, improvement in measurements is required in order to obtain better constrains.

Siegel et al. (2005) have constrained the value of Ω_m using a sample of 15 high-z H II galaxies ($2.17 < z < 3.39$) obtaining a best fit of $\Omega_m = 0.21^{+0.30}_{-0.12}$ for a Λ-dominated universe, which is consistent with other recent determinations. Their sample has been selected using the criterion of emission line strength as was selected in the (Melnick et al., 2000) sample. For the μ determination they have used (3.5) with a modification in the zero point (they used 26.18 in place of 26.44) due to the fact that
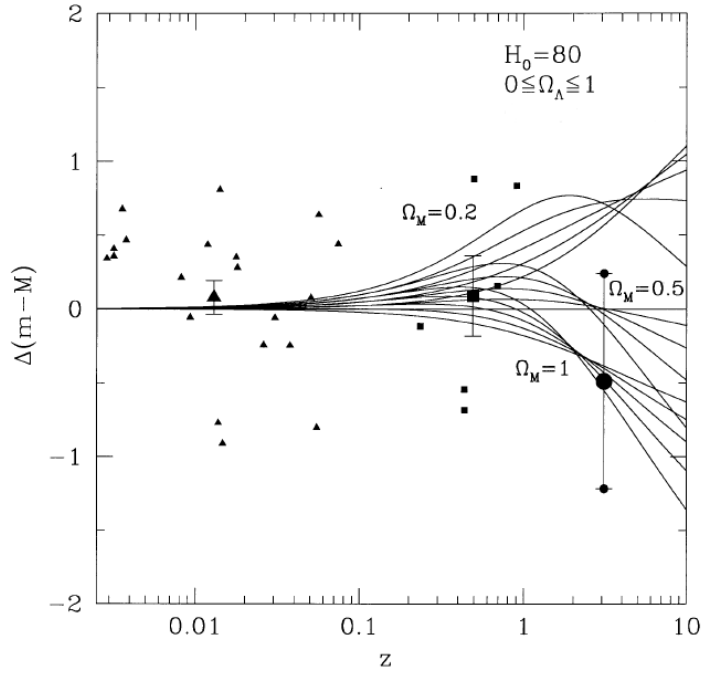
Figure 3.3: The differential Hubble diagram for H II galaxies with a wide range of red-shifts. Three families of curves for distinct values of Ω_m are shown, for every one $\Omega_\Lambda = (0, 0.25, 0.5, 0.75, 1.0)$. The large symbols represent the average redshift and distance modulus for each subsample. The error bars show the mean error in distance modulus assuming that each point is an independent measurement and ignoring observational errors. $H_0 = 80 \text{ km s}^{-1} \text{ Mpc}^{-1}$ was used to normalize the data points. The model lines are independent of H_0. Adapted from Melnick et al. (2000).

they have taken $H_0 = 71 \text{ km s}^{-1} \text{ Mpc}^{-1}$.

3.2.1 The physics of the $L(\mathrm{H}\beta) - \sigma$ relation

Melnick et al. (1987) found that H II galaxies present supersonic motions in their gaseous component. In order to explain the motions of the H II galaxies gaseous component, Terlevich & Melnick (1981) had proposed a model in which its nature is explained as being of gravitational origin. The basis for this argument is that correlations of the kind $L(\mathrm{H}\beta) \propto \sigma^4$ and $R \propto \sigma^2$ were observed in H II galaxies. These correlations are expected for virialized systems and in fact are observed in elliptical galaxies, spiral bulges and globular clusters.

Another factor that contributes to the origin of the supersonic turbulent motions in the gaseous component of H II galaxies is the stellar winds generated by massive
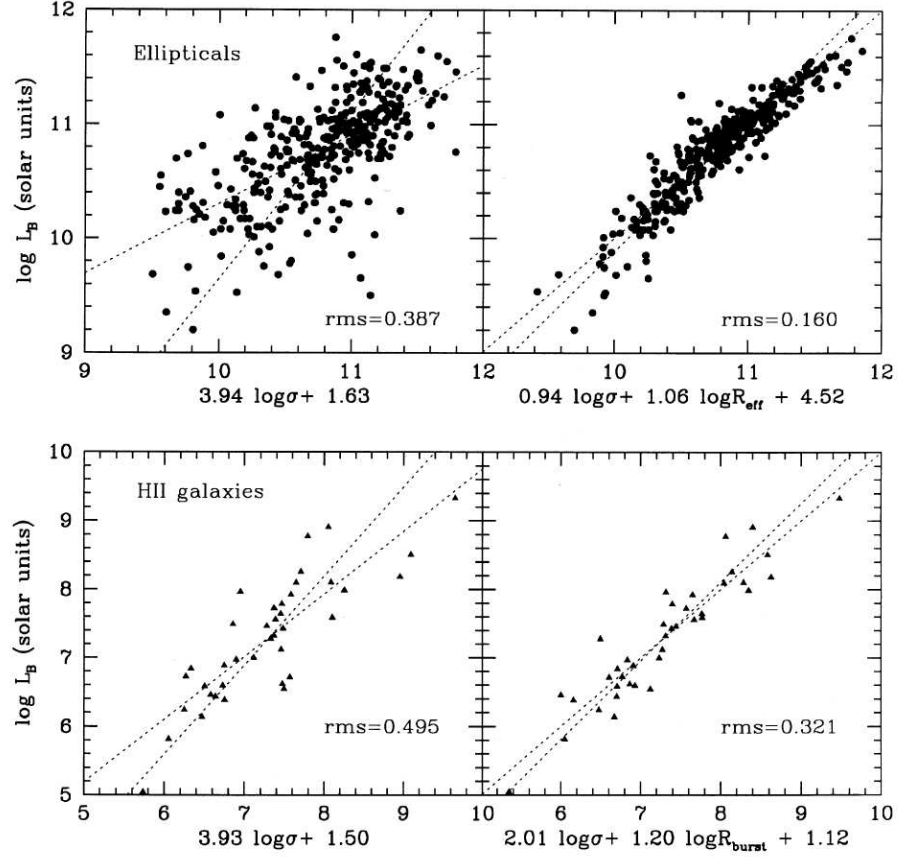
Figure 3.4: The fundamental plane of H II galaxies and normal elliptical galaxies from Telles & Terlevich (1995). The radii and magnitudes of H II galaxies are measured from continuum images. The velocity dispersions are the widths of the emission lines.

evolved stars. It has been shown that, unlike the case for evolved GEHRs where this effect dominates (Melnick et al., 1999) for H II galaxies it appears not to be dominant.

A strong support for the gravitational origin idea came from Telles (1995), where it is shown that these objects define a fundamental plane that is very similar to that defined by elliptical galaxies (see Figure 3.4). However, the scatter observed in the $L(H\beta) - \sigma$ may be due to the presence of a second parameter, perhaps possible variations in the initial mass function (IMF), rotation or the duration of the burst of star formation that powers the emission lines (Melnick et al., 2000).

It has been shown that the scatter in the $L(H\beta) - \sigma$ relation can be reduced if objects with $\sigma > 65$ kms^{-1} are rejected from the analysis (Melnick et al., 1988; Koo et al., 1995). This behavior can be understood if one assumes that H II galaxies are powered

by clusters of stars, then the above condition is equivalent to say that the time required for the clusters to form must be smaller that the main sequence lifetime of the most massive stars (Melnick et al., 2000).

3.2.2 Age effects

Around $3\,\mathrm{Myr}$ to $6\,\mathrm{Myr}$ after a starburst, the emission line flux decays fast and continuously whereas the continuum flux is roughly constant. Then, the equivalent widths (W) of emission lines are a good estimator of the starburst age (Copetti et al., 1986). In order to minimize systematic effects over the $L(\mathrm{H}\beta) - \sigma$ relation it is necessary to consider this effect by restricting the sample to objects with high $W(\mathrm{H}\beta)$ in order to select young starbursts and minimize the effects of a possible old underlying population over the equivalent width of the emission lines.

3.2.3 Extinction effects

Due to its effect over the flux of the $\mathrm{H}\beta$ line, the extinction or reddening is one important systematic for the $L(\mathrm{H}\beta) - \sigma$ relation. Two possible sources of extinction must be considered: dust in our Galaxy and dust in the H II galaxies themselves. It has been shown that the extinction correction for H II galaxies can be determined from Balmer decrements (Melnick et al., 1987, 1988).

3.2.4 Metallicity effects

The metallicity has an important effect over the $L(\mathrm{H}\beta) - \sigma$ relation as was pointed out in the analysis done by Terlevich & Melnick (1981) where it was shown that the residuals of this relation are correlated with metallicity. Furthermore, using PCA Melnick et al. (1987) showed that one of the two principal components with the larger weight was mostly determined by the oxygen abundance.
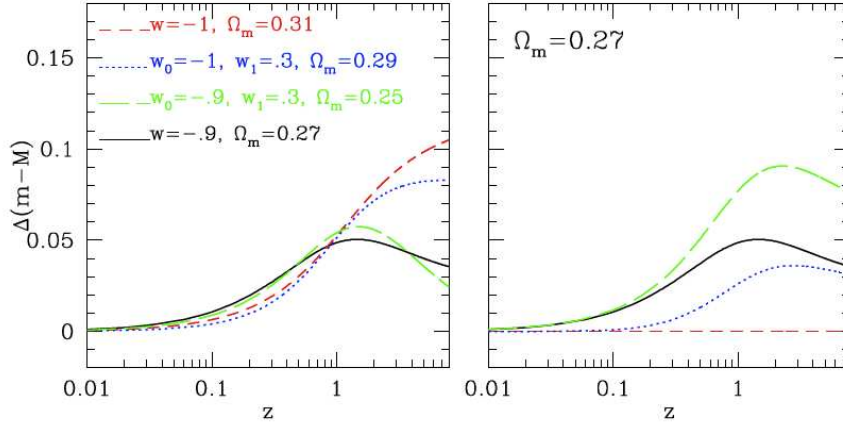
Figure 3.5: *Left Panel:* The expected distance modulus difference between the dark energy models shown and the reference Λ-model. *Right Panel:* The expected distance modulus differences once that the $\Omega_m - w(z)$ degeneracy is broken (imposing a unique Ω_m to all models). Taken from Plionis et al. (2009).

3.3 H II Galaxies as Cosmological Probes

This work's main aim is to constrain the parameter space of the dark energy equation of state and therefore we will begin by a brief theoretical analysis of the parameters involved.

From (2.20) we know that the Hubble function depends on the cosmological parameters following the relation:

$$H^2(z) = H_0^2 \left[\Omega_m (1+z)^3 + \Omega_w \exp\left(3 \int_0^z \frac{1 + w(x)}{1 + x} dx \right) \right], \qquad (3.6)$$

where we are neglecting the contribution of the radiation to the total energy density and we are assuming a flat universe. From (2.33) we know that:

$$\mu = 5 \log_{10} D_L + 25, \qquad (3.7)$$

where D_L, the luminosity distance is given by (2.31) and is expressed in Mpc.

Under the assumptions of (3.6) we can define a nominal *reference* Λ-cosmology with $\Omega_m = 0.27, \Omega_\Lambda = 0.73$ and $w = -1$. Then we can compare different models to the reference one. For this purpose we define:

$$\Delta \mu = \mu_\Lambda - \mu_{model} , \qquad (3.8)$$

39

Table 3.1: Cosmological parameters fits using the SNe Ia data within flat cosmologies. Note that for the case where $\mathbf{p} = (\Omega_m, w)$ (last row), the errors shown are estimated after marginalizing with respect to the other fitted parameters. Taken from Plionis et al. (2010).

D07			Constitution		
w	Ω_m	χ^2_{min}/df	w	Ω_m	χ^2_{min}/df
-1 (fixed)	$0.280^{+0.025}_{-0.015}$	$187.03/180$	-1 (fixed)	$0.286^{+0.012}_{-0.018}$	$439.78/365$
$-1.025^{+0.060}_{-0.045}$	0.292 ± 0.018	$187.02/179$	-1.025 ± 0.030	0.298 ± 0.012	$439.79/364$

where μ_Λ is the distance modulus given by the *reference* Λ-cosmology and μ_{model} is the one given by any another model.

Figure 3.5 shows the difference between some cosmological models for which their parameters are indicated. It can be seen that the relative magnitude deviations between dark energy models is ≤ 0.1 mag, which indicates the necessary high accuracy in the photometry of any object used as a tracer. Furthermore, it is clear that larger relative deviations of the distance moduli are present at $z \geq 1.5$, and therefore high-z tracers are needed to effectively constrain the values of the equation of state parameters, in fact at redshifts higher than those currently probed by SNe Ia.

Another important factor, that we can see in Figure 3.5, is that there are strong degeneracies between different cosmological models at $z \leq 1$ (in some cases even at higher redshifts), this due to the known $\Omega_m - w(z)$ degeneracy. This fact shows the necessity of at least two independent cosmological probes in order to break the degeneracies. If we additionally consider that we have abundant evidence for $0.26 \leq \Omega_m \leq 0.3$, we can expect that the degeneracies would be considerably reduced, as in fact is shown in the right hand panel of Figure 3.5.

As previously mentioned, the single available direct test for cosmic acceleration is based on the SNe Ia distance-redshift relation, and therefore it is useful to test how the constraints of the cosmological parameters change when the SNe Ia sample is increased. Plionis et al. (2010) analyse two SNe Ia data sets, the Davis et al. (2007) [hereafter *D07*] compilation of 192 SNe Ia and the *Constitution* compilation of 397 SNe Ia (Hicken et al., 2009), which are not independent since most of the *D07* is included in the *Constitution* sample.
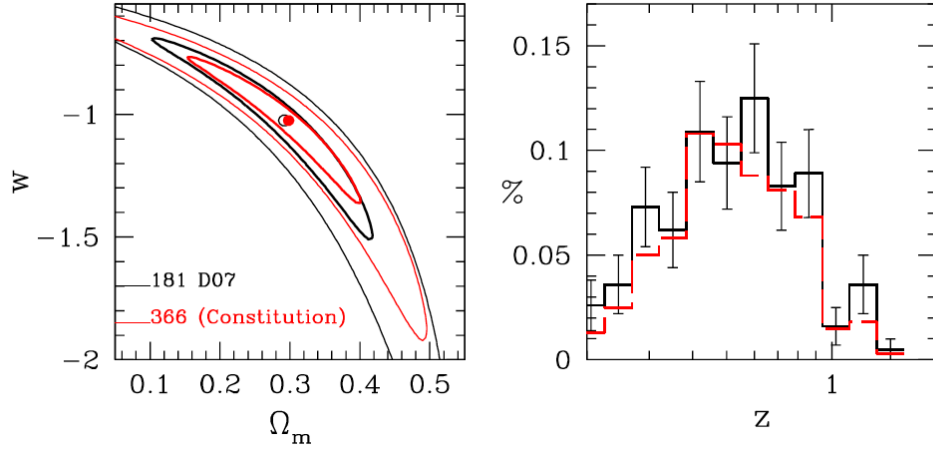
Figure 3.6: *Left Panel*: Cosmological parameters solution space using either of the two SNe Ia data sets (*Constitution:* red contours and *D07:* black contours). Contours corresponding to the 1 and 3σ confidence levels are shown. *Right Panel:* Normalized redshift distribution of the two SNe Ia data sets. Taken from Plionis et al. (2010).

In order to perform the data analysis, a likelihood estimator[1] (see Appendix B) was defined as:

$$\mathcal{L}^{SNIa}(\mathbf{p}) \propto \exp[-\chi^2_{SNIa}(\mathbf{p})/2], \tag{3.9}$$

where $\mathbf{p}$ is a vector containing the cosmological parameters that we want to fit for, and

$$\chi^2_{SNIa}(\mathbf{p}) = \sum_{i=1}^{N} \left[\frac{\mu^{th}(z_i, \mathbf{p}) - \mu^{obs}(z_i)}{\sigma_i} \right]^2, \tag{3.10}$$

where μ^{th} is given by (3.7) and (3.6), z_i is the observed redshift, μ^{obs} is the observed distance modulus and σ_i is the observed distance modulus uncertainty. A flat universe was assumed for the analysis so $\mathbf{p} \equiv (\Omega_m, w_0, w_1)$. Finally, since only SNe Ia with $z > 0.02$ were used in order to avoid redshift uncertainties due to peculiar motions, the final samples were of 181 (*D07*) and 366 (*Constitution*) SNe Ia.

Table 3.1 presents solutions using the previous mentioned data sets. We can see that the cosmological parameters derived are consistent between both data sets.

Figure 3.6 shows the cosmological parameters solution space for the two above mentioned data sets. We can see that although the *Constitution* data set has twice as many data points as *D07*, the constraints obtained form the former are similar to those obtained from the latter. This fact indicates that, for Hubble function tracers, increasing

---

[1] Likelihoods are normalized to their maximum values.
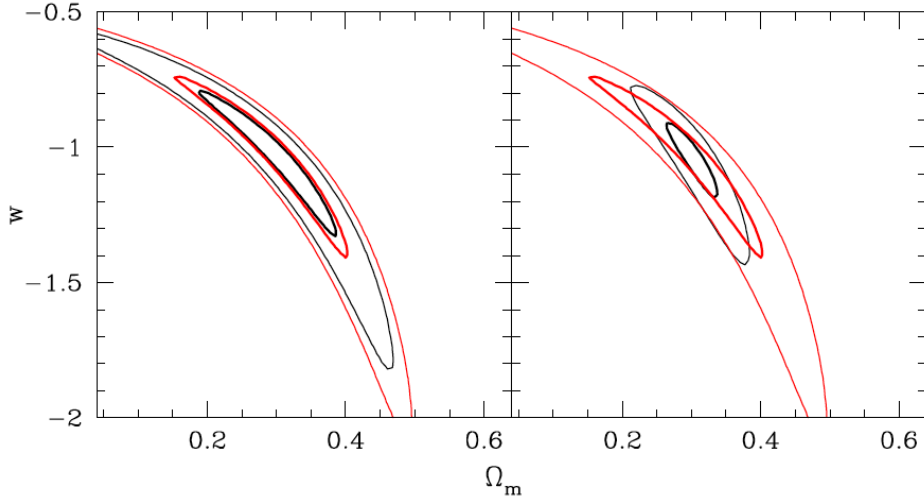
Figure 3.7: *Left Panel*: Comparison of the *Constitution* data set derived constraints (red contours) with those derived by reducing to half their uncertainties (black contours). *Right Panel:* Comparison of constrains from *Constitution* (red contours) with those derived by adding a sample of 82 high-z tracers ($2.7 \lesssim z \lesssim 3.5$) with distance modulus mean uncertainty of $\sigma_\mu \simeq 0.38$ (black contours). Taken from Plionis et al. (2010).

the number of data points covering the same redshift range and with the current uncertainty level for SNe Ia, does not provide significantly better constraints for cosmological parameters.

From the previous discussion it becomes clear that we have two possible options to obtain more stringent constraints of cosmological parameters:

- Trace the same redshift range ($z \lesssim 1.5$), that has been traced until now using SNe Ia, but reducing significantly the distance modulus uncertainties or

- Trace at higher redshifts, where the different theoretical models show the largest deviations, maintaining or if possible reducing the distance modulus uncertainties now obtained for high-z SNe Ia ($\langle \sigma_\mu \rangle \simeq 0.4$).

Plionis et al. (2010) analysed both alternatives by means of a Monte-Carlo procedure, and as it is shown in Figure 3.7, when the *Constitution* data uncertainties are reduced by half, the reduction in the range of the solution space is quite small; however, when a high-z 82 mock-object subsample, with distance modulus uncertainties comparable to those of actual high-z SNe Ia data, is added to the *Constitution* data set, a significantly reduced solution space was found. It is important to note that the redshift
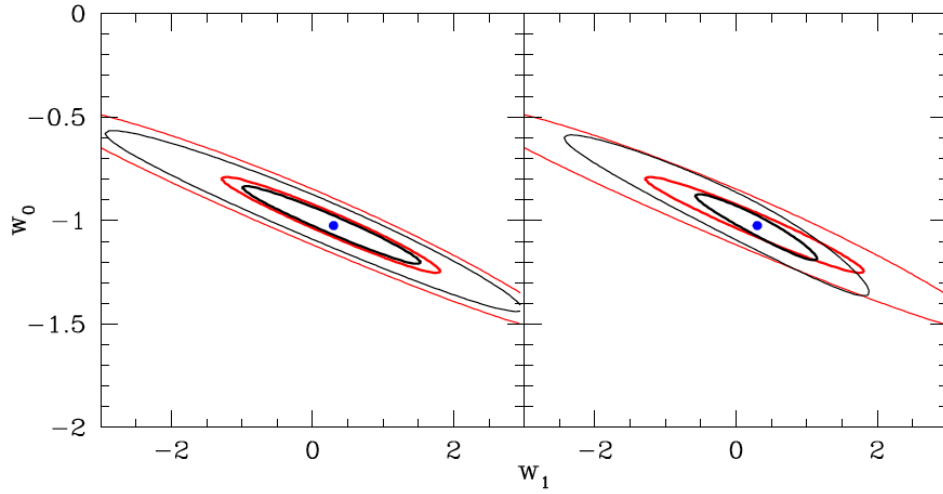
Figure 3.8: Similar as in Figure 3.7, but allowing for an evolving Dark Energy equation of state and after marginalizing with respect to Ω_m. The input cosmological model has $(w_0, w_1) = (-1.025, 0.3)$ and is represented by the red contours. Taken from Plionis et al. (2010).

distribution ($2.68 \lesssim z \lesssim 3.55$), for the added mock subsample, is in the range where the largest deviations between different cosmological models are expected (see Figure 3.5). The same behavior was found when an evolving dark energy equation of state model was implemented (see Figure 3.8).

From the previous discussion it is clear that in order to obtain more stringent constrains to the cosmological parameters, using the Hubble relation, a better strategy is to use standard candles which trace a redshift range where larger differences between the cosmological models are expected ($2 \lesssim z \lesssim 4$).

Near infrared surveys (Pettini et al., 2001; Erb et al., 2003) have shown that H II galaxies can be observed at much larger redshifts than SNe Ia and since they can be used as standard candles, due to their $L(\mathrm{H}\beta) - \sigma$ relation, they are excellent candidates for high-z tracers to be used to constrain the cosmological parameters.

In the next chapter we will list the actions needed to recalibrate the $L(\mathrm{H}\beta) - \sigma$ relation for H II galaxies and to construct their Hubble diagram in order to constrain the cosmological parameters solution space.

Chapter 4

Methodology

The main objective of this work is to trace the Hubble function using the redshift-distance relation for H II galaxies with the intention of obtaining more stringent constraints for the dark energy equation of state parameters. However, in order to fulfill this objective, we must recalibrate the H II galaxies $L(H\beta) - \sigma$ relation taking care of all possible systematics that can affect it.

From the methodological view point, we need to consider two distinct phases for this project:

- During the first phase, we must obtain a low-z, or local, sample of H II galaxies from which we will derive the required recalibration of the $L(H\beta) - \sigma$ relation.

- The second phase consists of obtaining intermediate and high-z samples of H II galaxies which will be used to improve the constraints to cosmological parameters.

Through this chapter, we will describe the methodology for the acquisition and analysis of the data needed to accomplish every one of the above mentioned phases.

4.1   The Local Universe Sample

A local sample of 128 objects was selected from the Sloan Digital Sky Survey (SDSS) Data Release 7 (DR7) spectroscopic data. We used as selection criteria the presence of

strong emission lines and a redshift range $0.01 < z < 0.2$, which allows us to avoid objects affected by local peculiar motions relative to the Hubble flow while keeping exposure times relatively short. The targets have magnitudes $g = 15.8 - 19.4$ and Hβ fluxes $I(\mathrm{H}\beta) = 4 - 49 \times 10^{-15}$ erg s^{-1} cm^{-2} as measured from the SDSS $3''$ fibers.

4.1.1 Observations

The observations required for the $L(\mathrm{H}\beta) - \sigma$ relation calibration are of two types:

- High resolution spectroscopy to measure the velocity dispersion from the Hβ line profile (typical values are $20 - 80$ km s^{-1}).

- Low resolution spectroscopy with wide slits (spectrophotometry) to obtain the integrated emission lines flux. Since the typical objects angular size is $\lesssim 10''$.

The high resolution spectroscopy already has been performed for the entire sample by means of echelle spectroscopy at 8 meter class telescopes. The telescopes and instruments used are the Ultraviolet and Visual Echelle Spectrograph (UVES) at the European Southern Observatory (ESO) Very Large Telescope (VLT) in Chile and the High Dispersion Spectrograph (HDS) at the National Astronomical Observatory of Japan (NAOJ) Subaru Telescope in Hawaii.

The low resolution spectroscopy is being performed with long slit spectrographs at 2 meter class telescopes, specifically using the Boller & Chivens spectrograph (B&C) at the Observatorio Astronómico Nacional (OAN) in San Pedro Mártir and the B&C at the Observatorio Astrofísico Guillermo Haro (OAGH) in Cananea.

The data reduction is being performed using IRAF[1] procedures and the reduction pipelines provided for the instruments UVES and HDS.

---

[1] IRAF is distributed by the National Optical Observatory, which is operated by the Association of Universities for Research in Astronomy, Inc., under cooperative agreement with the National Science Foundation.

4.1.2 Line widths and profiles

The line widths are estimated from the echelle data. The measured velocity dispersions are corrected as follows

$$\sigma_0^2 = \sigma_{obs}^2 - \sigma_{th}^2 - \sigma_{inst}^2, \tag{4.1}$$

where σ_{obs} is the observed velocity dispersion, σ_{th} is the thermal broadening and σ_{inst} is the instrumental broadening.

The thermal broadening is due to the components of the thermal motions of atoms along the line of sight, and is given by

$$\sigma_{th} = \sqrt{\frac{kT}{mc^2}} \lambda_0, \tag{4.2}$$

where k is the Boltzmann constant, T is the temperature, m is the mass of the emitting particle, c is the speed of light and λ_0 is the rest wavelength.

The instrumental profile contributes to the observed profile as

$$g(\lambda) = \int f(\lambda - x) h(x) dx, \tag{4.3}$$

where $f(\lambda)$ is the input line profile, $h(\lambda)$ is the instrumental profile and $g(\lambda)$ is the output profile. We have here a convolution between the instrumental and line profiles. In general, if we assume that the instrumental profile and the line profile have gaussian shape, then we can measure the instrumental profile width directly from skylines.

Uncertainties in the observed widths are estimated by comparison of the [O III] $\lambda 5007$ and [O III] $\lambda 4959$ profiles (Heckman et al., 1981).

In order to analyse the lines profile, we follow the profile parametrization given by Whittle (1985). He defines two lengths a and b as the distances from the line profile median to the position at left and right where 10 % of the profile has been integrated from the profile extremes (see Figure 4.1).

From a and b, the following parameters can be constructed:

$$IPV(20\%) = (a + b) \text{ km s}^{-1}, \tag{4.4}$$

$$A(20\%) = (a - b)/(a + b), \tag{4.5}$$

$$S(20\%) = (a - b) \text{ km s}^{-1}, \tag{4.6}$$

where, IPV is the inter percentile velocity, A is the asymmetry and S is the shift.
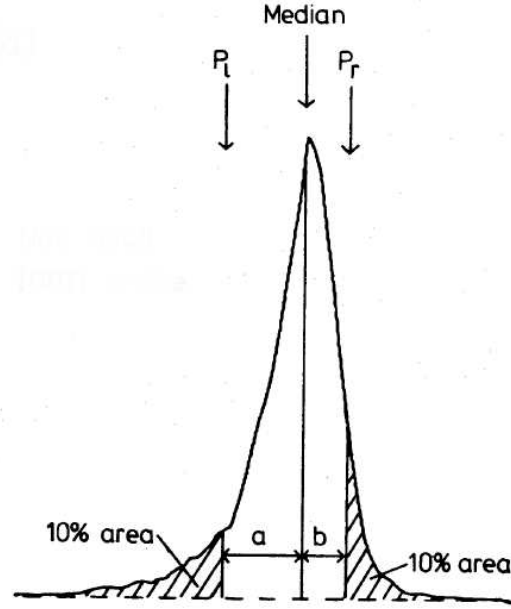
Figure 4.1: Definitions for an area parameter scheme to characterize profile symmetry and width. Taken from Whittle (1985).

4.1.3 Distances

The purpose of the local sample is to calibrate the $L(\mathrm{H}\beta) - \sigma$ relation for H II galaxies, so object distances must be obtained in order to calculate $L(\mathrm{H}\beta)$ from line fluxes.

From equation (2.35), we know that, at low redshifts, the distance to an object can be obtained from:

$$D_L \equiv r \approx \frac{cz}{H_0},\qquad(4.7)$$

where z is the redshift, and r is the distance. However, we need to correct for the motion of the sun relative to the Local Group (LG) centroid and for the "Kaiser" effect, i.e. a line of sight distortion caused by the additional Doppler shift to the cosmological redshift, given by peculiar velocities (Kaiser, 1987).

To correct from heliocentric velocity ($v_{hel} = cz$) to velocity at the LG frame, v_{LG}, we have (Courteau & van den Bergh, 1999):

$$v_{LG} = v_{hel} - 79\cos l \cos b + 296\sin l \cos b - 36\sin b,\qquad(4.8)$$

where l and b are the Galactic coordinates of the observed galaxy.

The Kaiser effect correction is given as (Basilakos & Plionis, 1998):

$$r = \frac{cz}{H_0} + \frac{1}{H_0}[\mathbf{v}(r) - \mathbf{v}(0)] \cdot \hat{\mathbf{r}}, \tag{4.9}$$

where $\mathbf{v}(0)$ is the peculiar velocity of the LG relative to the CMB and $\mathbf{v}(r)$ the peculiar velocity of a galaxy at position r. We must understand that this last correction is only important at low redshifts and that if $\mathbf{v}(r)$ has random orientation, the correction is dominated by the Local Group term.

For estimating the distance we use the value for $H_0 = 73 \pm 1.9 \text{ km s}^{-1} \text{ Mpc}^{-1}$ determined by Tegmark et al. (2006) from CMB (WMAP) and BAO (SDSS luminous red galaxies power spectrum). In general we will use the redshifts derived from SDSS spectra and their corresponding errors. The errors in distance are straightforwardly calculated from error propagation.

4.1.4 Emission line fluxes

The emission line fluxes are measured from long slit spectra that are taken using a wide slit in order to avoid flux loses. The 1σ uncertainties in the flux will be estimated from the expression (Tresse et al., 1999):

$$\sigma_F = \sigma_c D \sqrt{2N_{pix} + W/D}, \tag{4.10}$$

where σ_c is the mean standard deviation per pixel of the continuum on each side of the line, D is the spectral dispersion, N_{pix} is the number of pixels covered by the line and W is the line equivalent width. The error in W can be calculated from:

$$\sigma_W = \frac{W}{F}\sigma_c D \sqrt{W/D + 2N_{pix} + (W/D)^2/N_{pix}}. \tag{4.11}$$

4.1.5 Extinction

The reddening corrections are done using the absorption coefficients derived from Balmer decrements, since we have fluxes for Hα, Hβ and Hγ. However, the presence of an underlying old population can not be completely ruled out from all the sample objects, and consequently we will have Balmer emission lines superimposed to stellar absorption lines. One important consequence of this last situation is that the internal extinction is overestimated (Olofsson, 1995).

In order to correct for the underlying absorption lines in the extinction determinations, we use the technique proposed by Rosa-González et al. (2002). The first step is the determination of the underlying Balmer absorption (Q) and "true" visual extinction (A_V) from the observed one (A_V^*).

The ratio between a line intensity, $F(\lambda)$, and Hβ line intensity, $F(\text{H}\beta)$, is given by

$$\frac{F(\lambda)}{F(\text{H}\beta)} = \frac{F_0(\lambda)}{F_0(\text{H}\beta)} 10^{-0.4A_V[k(\lambda)-k(\text{H}\beta)]/R_V}, \tag{4.12}$$

where, $k(\lambda) = A(\lambda)/E(B-V)$ is given by the used extinction law, $R_V = A_V/E(B-V)$ is the optical total-to-selective extinction ratio and the subscript 0 indicates unreddened values.

For the analysis we use as reference the theoretical ratios for Case B recombination $F_0(\text{H}\alpha)/F_0(\text{H}\beta) = 2.86$ and $F_0(\text{H}\gamma)/F_0(\text{H}\beta) = 0.47$(Osterbrock, 1989). In absence of an underlying absorption, the observed flux ratios can be expressed as a function of the theoretical ratios and the visual extinction:

$$\log_{10} \frac{F(\text{H}\alpha)}{F(\text{H}\beta)} = \log_{10} 2.86 - 0.4[k(\text{H}\alpha) - k(\text{H}\beta)]A_V/R_V, \tag{4.13}$$

$$\log_{10} \frac{F(\text{H}\gamma)}{F(\text{H}\beta)} = \log_{10} 0.47 - 0.4[k(\text{H}\gamma) - k(\text{H}\beta)]A_V/R_V. \tag{4.14}$$

When we include the underlying absorption and assume that the absorption and emission lines have the same widths, the observed ratio between Hα and Hβ is given as

$$\frac{F(\text{H}\alpha)}{F(\text{H}\beta)} = \frac{2.86\{1 - PQ[W_+(\text{H}\beta)/W_+(\text{H}\alpha)]\}}{1 - Q}, \tag{4.15}$$

where, $W_+(\text{H}\alpha)$ and $W_+(\text{H}\beta)$ are the equivalent widths in emission for the lines, $Q = W_-(\text{H}\beta)/W_+(\text{H}\beta)$ is the ratio between the equivalent widths of Hβ in absorption and in emission, $P = W_-(\text{H}\alpha)/W_-(\text{H}\beta)$ is the ratio between the equivalent widths in absorption of Hα and Hβ.

The value P can be obtained theoretically from spectra evolution models. Olofsson (1995) has shown that for solar abundance and stellar mass in the range $0.1 \text{ M}_\odot \leq M \leq 100 \text{ M}_\odot$ using a Salpeter IMF, the value of P is close to 1 with a dispersion ~ 0.3 for ages between $1 - 15$ Myr. Since the variation of P produces a change in $F(\text{H}\alpha)/F(\text{H}\beta)$ ratio of less than 2 %, then we assume $P = 1$.

For the ratio between Hγ and Hβ, we have

$$\frac{F(\text{H}\gamma)}{F(\text{H}\beta)} = \frac{0.47 - GQ}{1 - Q}, \tag{4.16}$$

where $G = W_-(\text{H}\gamma)/W_-(\text{H}\beta)$ is the ratio between the equivalent widths in absorption of Hγ and Hβ. The work of González Delgado et al. (1999) strongly suggests that the value of the parameter G can be taken as 1.

Having as origin the theoretical values for the ratios $\log_{10}[F(\text{H}\alpha)/F(\text{H}\beta)] = 0.46$ and $\log_{10}[F(\text{H}\gamma)/F(\text{H}\beta)] = -0.33$, using the observed ratios we can define a vector for the observed visual extinction $(\mathbf{A}^*_\mathbf{V})$ and from equations (4.13) and (4.14) and a set of values for A_V, we define a vector for the "true" visual extinction, whereas from equations (4.15) and (4.16) and a set of values of Q, we define a vector for the underlying absorption $\mathbf{Q}$. Assuming that the vector addition $\mathbf{Q} + \mathbf{A_V} = \mathbf{A}^*_\mathbf{V}$ is satisfied, by minimizing the distance between the position of the vector $\mathbf{A}^*_\mathbf{V}$ and the vector addition $\mathbf{Q} + \mathbf{A_V}$ for every pair of parameters (Q, A_V), we obtain simultaneously the values for Q and A_V that correspond to the observed visual extinction.

The unreddened fluxes are obtained from the expression

$$F_{obs}(\lambda) = F_o(\lambda)10^{-0.4A_V k(\lambda)/R_V}, \tag{4.17}$$

where the used extinction law is given by Calzetti (1999).

Finally, the errors are propagated by means of a Monte Carlo procedure (see Appendix B).

4.1.6 Abundances

The estimated abundances are O/H, since oxygen is used as indicator of metallicity. Electron densities are derived from the graph given by Osterbrock (1988) using the ratio [O II] $\lambda3729$/[O II] $\lambda3726$ and assuming initially $T = 10^4$ K. Then we calculate the electron temperature as (Pagel et al., 1992):

$$t \equiv t(\text{O III}) = 1.432[\log_{10} R - 0.85 + 0.03 \log_{10} t + \log_{10}(1 + 0.0433xt^{0.06})]^{-1}, \tag{4.18}$$

where t is given in units of 10^4 K, $x = 10^{-4} n_e t_2^{-1/2}$, n_e is the electron density in cm^{-3} and

$$R \equiv \frac{I(4959) + I(5007)}{I(4363)}, \tag{4.19}$$

$$t_2^{-1} = 0.5(t^{-1} + 0.8); \tag{4.20}$$

the abundances can be calculated from:

$$12 + \log_{10}(\mathrm{O}^{++}/\mathrm{H}^+) = \log_{10} \frac{I(4959) + I(5007)}{\mathrm{H}\beta} + 6.174 + \frac{1.251}{t} - 0.55 \log_{10} t \tag{4.21}$$

$$12 + \log_{10}(\mathrm{O}^+/\mathrm{H}^+) = \log_{10} \frac{I(3726) + I(3729)}{\mathrm{H}\beta} + 5.890 + \frac{1.676}{t_2} - 0.40 \log_{10} t_2$$
$$+ \log_{10}(1 + 1.35x); \tag{4.22}$$

total abundance for oxygen is derived by adding this last two equations.

The errors are propagated by means of a Monte Carlo procedure.

4.2 The Intermediate and High-z Samples

In order to effectively obtain more stringent constraints to cosmological parameters, we must obtain intermediate ($0.2 < z \leq 1.5$) and high-z ($z > 1.5$) samples of *bona fide* H II galaxies. The sample could be obtained from a search in published near infrared surveys of intermediate and high-z starburst galaxies.

Lyman break galaxy (LBGs) surveys are the natural place to begin the search. LBGs are starburst galaxies, but otherwise normal, at high redshifts ($2.5 \lesssim z \lesssim 5$) identified by the colors of their spectral energy distribution (SED) around the Lyman continuum discontinuity (912 Å) (Giavalisco, 2002). The spectra of LBGs is remarkably similar to those of local starburst galaxies. Examples of near infrared spectroscopic surveys of LBGs are the ones accomplished by Pettini et al. (2001) and Erb et al. (2003).

An important selection criterion is that of selecting galaxies with $W(\mathrm{H}\beta) > 25$ Å as has been advocated by Melnick et al. (2000), in order to avoid the already evolved H II galaxies, which apparently follow a shifted $L(\mathrm{H}\beta) - \sigma$ relation (see Section 3.2).

4.2.1 Observations

In order to measure the velocity dispersion from the Hβ line profile, we require echelle spectroscopy at 8 meter class telescopes ranging from the visual to the near infrared.

For the Hβ line profile measurements, we propose to make use of the X-Shooter instrument at ESO-VLT in Chile. X-Shooter is a single target echelle spectrograph of intermediate resolution ($R = 4000 - 14000$) with a wavelength range of $3000 - 25000$ Å split in 3 arms (Kaper et al., 2009). This instrument allows Hβ line profile measurements up to $z \sim 4$.

4.2.2 Extinction

The extinction determination for the intermediate and high-z samples could be done if our observations include Hβ and Hγ, then we could do direct determinations of the reddening using the Balmer decrement technique explained in Section 4.1.5.

4.2.3 Abundances

The abundances O/H, for the intermediate and high-z samples could be determined by means of the method outlined in Section 4.1.6, then our observed spectra must go up to [O III] $\lambda5007$ line at least, this implies that with the proposed instrument we can go to $z \sim 4$, which is enough for our purposes.

Chapter 5

The Local Universe Sample

Through this chapter we give a detailed description of the local universe sample of H II galaxies and some preliminary results obtained for the $L(\mathrm{H}\beta) - \sigma$ relation calibration.

The first section of this chapter describes the basic characteristics of the local universe sample of H II galaxies, through the second section the performed observations are described in detail, while the third section explains the observation reduction procedures; finally the last section describes the preliminary results obtained.

5.1   The Sample

The sample is composed of 128 H II galaxies selected from the SDSS DR7 spectroscopic data, in accordance with the presence of strong emission lines and in a redshift range $0.01 < z < 0.2$. Figure 5.1 shows the sample distribution in redshift, we can see that a big fraction of the galaxies have $z < 0.1$, then the correction for "Kaiser" effect (see Section 4.1.3) becomes important.

Figure 5.2 shows the H II galaxies local sample distribution in right ascension. From the figure, it is clear that the distribution is not uniform, however it can be covered with two observing runs, strategically located at two semesters of the same year.

Figure 5.3 shows the H II galaxies local sample sky distribution in Galactic Coordinates. We can see that almost all the objects avoid the galactic plane, limiting the effect of dust extinction from the Galaxy.
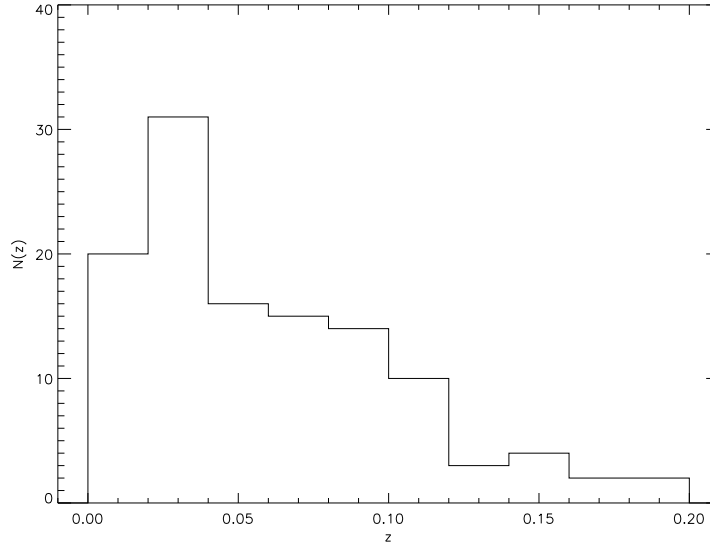
Figure 5.1: Redshift distribution of the local sample of H II galaxies.
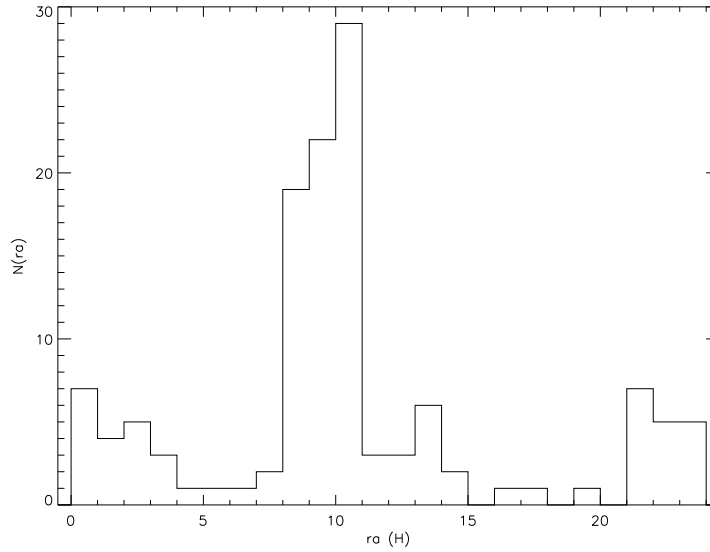
Figure 5.2: Local sample of H II galaxies distribution in right ascension.
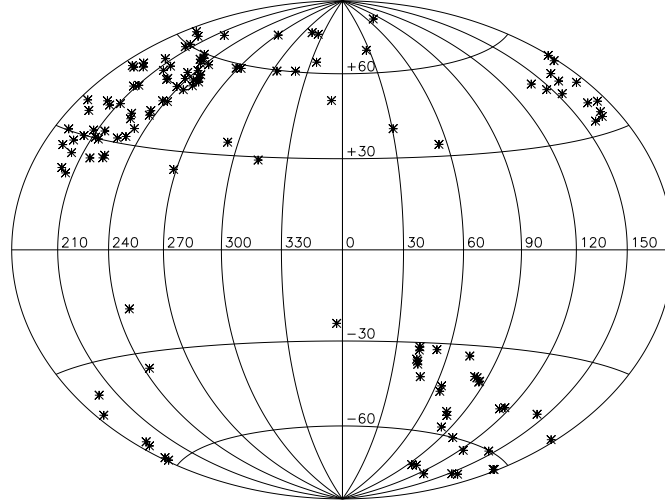
Figure 5.3: Local sample of H II galaxies sky distribution in Galactic coordinates.

5.2 Observations

Two types of observation have been carried out, high resolution echelle grating spectroscopy to measure the velocity dispersion from the Hβ line profile and low resolution long-slit spectroscopy with wide slits (spectrophotometry) to obtain the integrated emission line fluxes.

In Table 5.1 a journal of observations is shown giving a few details about the different observing runs. Through the next two sections the high and low resolution measurements are described in greater detail.

Table 5.1: Journal of observations for the H II galaxies local sample high and low resolution measurements.

Dates	Telescope	Instrument	Detector	Slit	Observer
5 & 16 Nov 2008	NOAJ-Subaru	HDS	EEV ($2 \times 2K \times 4K$)[a]	4"	F. Bresolin
16 & 17 Apr 2009	ESO-VLT	UVES-Red	EEV ($2 \times 2K \times 4K$)	2"	R. Terlevich & E. Terlevich
15 - 17 Mar 2010	OAN - 2.12m	B&C	SITe3 ($1K \times 1K$)	10"	F.Bresolin & R. Chávez
10 - 13 Apr 2010	OAGH - 2.12m	B&C	VersArray (1300×660)	8.14"	R. Terlevich, E. Terlevich & R. Chávez

[a] 2×4 binning.

5.2.1 High resolution spectroscopy

The high dispersion observations for the local sample were performed using 8 meter class telescopes with echelle grating spectrographs, since this technique provides high dispersion and high spectral resolution. The employed instruments were the UVES at ESO-VLT observatory in Chile and the HDS at NAOJ-Subaru Telescope in Hawaii.

In general the spectral resolution, R, is given by

$$\frac{\lambda}{\Delta\lambda} = R = nN, \tag{5.1}$$

where n is the interference order, N is the number of grating lines, λ is the operating wavelength and is related to the angular Rayleigh resolution ($\Delta\theta$) as $\lambda = Ns\Delta\theta\cos\theta$, where s is the separation of the lines and θ is the angle to the normal to the grating in which the light is dispersed; $\Delta\lambda$ is the smallest wavelength interval that may be resolved and is given by $\Delta\lambda = ns\Delta\theta\cos\theta$.

From the above equation we see that the spectral resolution is dictated by the order of the spectrum and the number of grating lines. Then observing a high order spectra we can improve the resolution. Echelle gratings operate at high orders, therefore in order to avoid obscuration of those high orders by the vertical parts of the grating, they have great blaze angles.[1] Furthermore, in order to avoid the superimposition of the different order spectra, a Cross Disperser is used to separate them [see eg. Kitchin (1995)].

UVES is a high resolution cross-dispersed echelle spectrograph located at the Nasmyth B focus of ESO-VLT Unit Telescope 2 (UT2) (Kueyen). The instrument accessible spectral range goes from 3000 Å to 11000 Å with two arms. The maximum spectral resolution is 80000 in the Blue Arm or 110000 in the Red Arm. A complete description of the instrument is given by Dekker et al. (2000).

HDS is a high resolution cross-dispersed echelle spectrograph located at the Optical Nasmyth platform of NAOJ-Subaru Telescope. The instrument accessible spectral range goes from 3000 Å to 10000 Å. The maximum spectral resolution is 160000. A complete description of the instrument is given by Noguchi et al. (2002).

---

[1] The blaze angle is the individual grooves tilt angle with respect to the grating surface normal.

5.2.2 Spectrophotometry

The long-slit spectroscopy with wide slit or spectrophotometry for the H II galaxies local sample was performed using 2 meter class telescopes, the instruments employed were the B&C spectrograph at OAN 2.12 m telescope in San Pedro Martir (Baja California, Mexico) and the B&C spectrograph at OAGH 2.12 m telescope in Cananea (Sonora, Mexico).

The B&C at OAN is a low resolution spectrograph, the grating employed has $600\,\mathrm{l\,mm^{-1}}$ and a blaze angle of $8°63'$, it was centered at ~ 5850 Å; the width of the slit was 10". The resolution obtained with this configuration is $R \sim 347$ and the spectral coverage was of ~ 2100 Å.

The B&C at OAGH is also a low resolution spectrograph, the grating employed through the observations has $150\,\mathrm{l\,mm^{-1}}$ and a blaze angle of $3°30'$; it was centered at ~ 5000 Å. The slit width was 8.14".

5.3 Reduction Procedures

The UVES data reduction was carried out using the UVES pipeline V4.3.0 over the GASGANO V2.2.7 environment[2] . Figure 5.4 shows an example of UVES echelle spectra reduced using the mentioned procedure.

The HDS data were reduced using IRAF packages and a script for overscan removal and detector linearity corrections provided by the NAOJ-Subaru telescope team. Figure 5.5 shows an example of HDS echelle spectra reduced using the mentioned procedure.

The long-slit spectra observed at OAN and OAGH were reduced using IRAF. Figure 5.6 shows an example of a long-slit reduced spectrum.

Table 5.2 shows the local H II galaxies sample and the corresponding Hβ FWHM and flux measurements. The Hβ flux measurements have been taken from the SDSS DR7 spectroscopic data, since not all the long slit observations have been carried out yet.

---

[2] GASGANO is a JAVA based Data File Organizer developed and maintained by ESO.
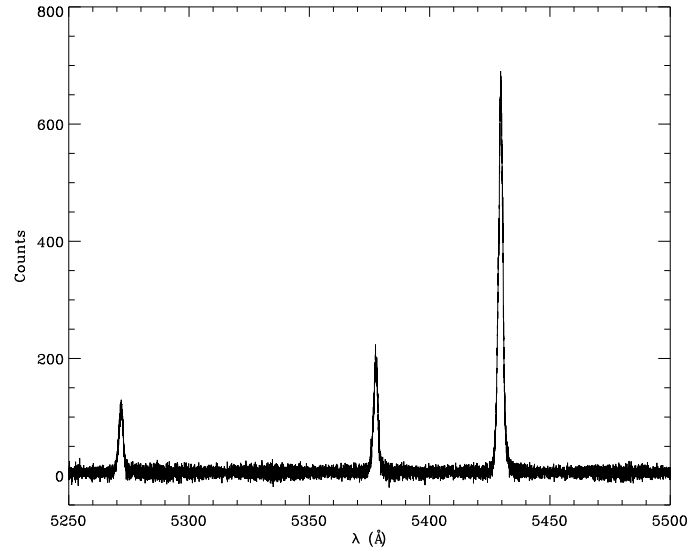
Figure 5.4: A UVES spectrum reduced using the UVES pipeline V4.3.0.
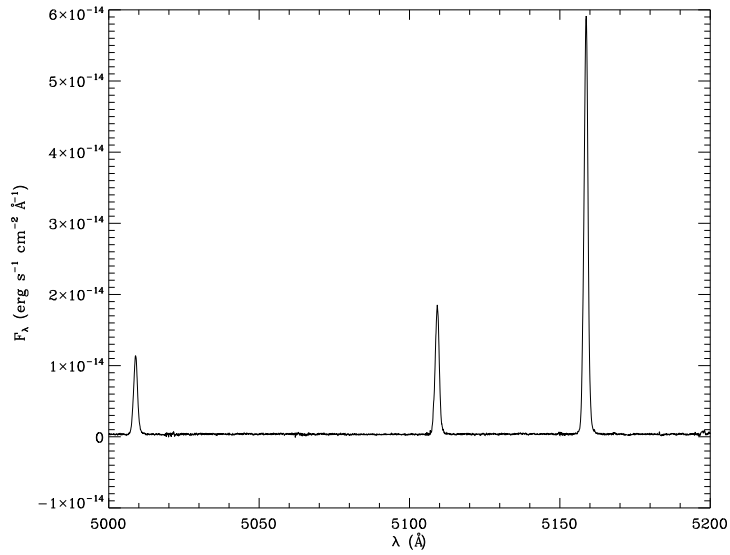
Figure 5.5: An HDS spectrum reduced using the IRAF package.
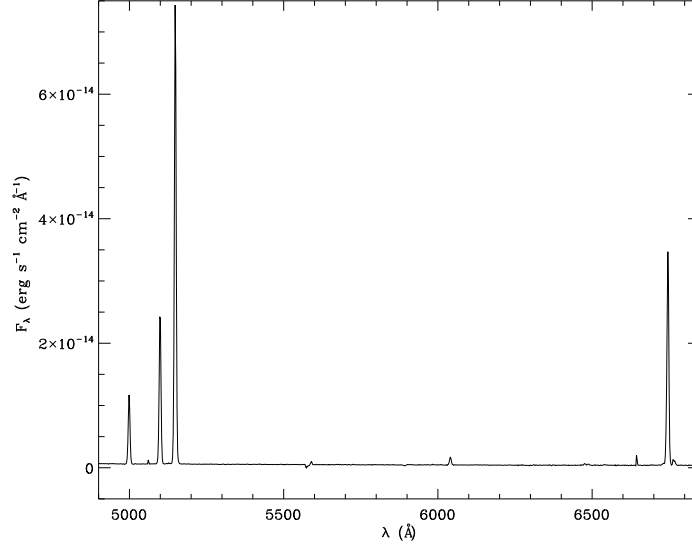
Figure 5.6: An example of a long-slit spectrum reduced using the IRAF package.

Table 5.2: Measurements for H II galaxies local sample. The Hβ flux is taken from the SDSS DR7 spectroscopic data, the Hβ FWHM has been measured form the observations.

Name	R.A.(deg) (J2000)	Dec. (deg) (J2000)	z	Hβ flux (10^{-17} erg s^{-1}cm^{-2})	Hβ FWHM (Å)	Mag (g)
J000657.02+005125.9	1.738	0.857	0.074	887.310	3.266	18.55
J001647.75-104742.2	4.199	-10.795	0.023	1717.550	2.959	16.36
J002339.62-094848.6	5.915	-9.814	0.053	1281.400	2.912	17.58
J002425.94+140410.6	6.108	14.070	0.014	2756.820	3.277	15.86
J003218.59+150014.1	8.077	15.004	0.018	2530.140	3.092	16.49
J005147.3+000940	12.947	0.161	0.038	964.801	2.929	17.97
J005602.26-101009.4	14.009	-10.169	0.058	665.667	3.239	18.34
J013258.54-085337.6	23.244	-8.894	0.095	797.703	3.099	18.82
J013344.63+005711.2	23.436	0.953	0.019	710.715	2.542	17.79
J014137.21-091435.2	25.405	-9.243	0.018	910.119	2.489	17.47
J014707.03+135629.2	26.779	13.941	0.057	1143.680	3.148	17.98
J021852.9-091218.7	34.720	-9.205	0.013	715.859	2.829	18.12
J022037.66-092907.2	35.157	-9.485	0.113	870.718	3.855	19.13
J024052.19-082827.4	40.217	-8.474	0.082	1732.470	3.611	18.98
J024453.66-082137.9	41.224	-8.361	0.078	698.172	3.192	18.83
J025426.12-004122.6	43.609	-0.690	0.015	1332.450	2.841	17.31
J030321.41-075923.1	45.839	-7.990	0.165	652.144	4.009	19.37
J031023.94-083432.8	47.600	-8.576	0.052	608.647	3.077	18.73
J033526.63-003811.3	53.861	-0.636	0.023	690.638	2.772	17.75
J040937.62-051805.8	62.407	-5.302	0.075	614.001	2.816	19.16
051519-391741	78.829	-39.295	——	——	——	——

Continued on Next Page. . .

61

Table 5.2 – Continued

Name	R.A. (deg) (J2000)	Dec. (deg) (J2000)	z	Hβ flux (10^{-17} erg s^{-1}cm^{-2})	Hβ FWHM (Å)	Mag (g)
064650-374322	101.708	-37.723	——	——	——	——
J074806.30+193146.9	117.026	19.530	0.063	873.054	3.005	18.25
J074947.00+154013.3	117.446	15.670	0.074	447.334	3.304	18.90
J080000.69+274642.0	120.003	27.778	0.039	988.880	2.968	17.47
J080619.49+194927.3	121.581	19.824	0.070	2933.670	3.938	16.97
J081334.17+313252.1	123.392	31.548	0.020	2265.630	2.540	16.48
J081403.77+235328.9	123.516	23.891	0.020	1205.840	3.090	17.56
J081420.78+575008	123.587	57.836	0.055	738.648	2.936	17.69
J081737.59+520236.3	124.407	52.043	0.024	2504.000	2.978	16.38
J082520.11+082723.2	126.334	8.456	0.087	436.081	3.223	18.89
J082530.68+504804.4	126.378	50.801	0.097	1053.990	3.656	18.59
J082722.57+202612.7	126.844	20.437	0.109	891.573	3.739	18.25
J083946.02+140033.2	129.942	14.009	0.112	703.921	3.728	18.74
J084000.37+180530.9	130.002	18.092	0.072	1092.700	3.221	18.91
J084029.91+470710.2	130.125	47.120	0.042	2499.880	3.232	17.60
J084056.02+022030.9	130.233	2.342	0.050	737.187	3.530	18.50
J084219.07+300703.5	130.579	30.118	0.084	962.136	3.652	17.81
J084220.94+115000.3	130.587	11.833	0.029	2204.440	2.966	16.47
J084414.22+022621.2	131.059	2.439	0.091	1676.480	3.884	18.10
J084527.61+530852.9	131.365	53.148	0.031	1983.240	2.700	17.08
J084634.39+362620.8	131.643	36.439	0.011	3247.390	2.706	16.31
J085221.71+121651.7	133.090	12.281	0.076	3707.300	3.835	17.35
J090418.11+260106.3	136.075	26.018	0.098	1137.280	3.841	18.01
J090506.86+223833.8	136.279	22.643	0.126	797.280	3.446	18.92
J090531.07+033530.4	136.379	3.592	0.039	1101.830	3.036	17.60
J091434.95+470207.2	138.646	47.035	0.027	3948.050	2.796	16.29
J091640.98+182807.9	139.171	18.469	0.022	1122.660	2.668	17.99
J091652.23+003113.9	139.218	0.521	0.057	655.065	3.227	18.51
J092540.93+063116.8	141.421	6.521	0.075	682.426	3.656	18.25
J092749.18+084037.1	141.955	8.677	0.107	830.257	3.991	18.71
J092918.39+002813.1	142.327	0.470	0.094	700.588	2.939	19.28
J093006.43+602653.3	142.527	60.448	0.014	3212.300	2.560	16.84
J093424.08+222522.6	143.600	22.423	0.084	991.600	3.701	18.48
J093813.49+542825	144.556	54.474	0.102	1512.650	4.005	17.53
J094000.51+203122.5	145.002	20.523	0.045	1038.600	3.042	18.05
J094252.78+354725.9	145.720	35.791	0.015	1919.670	2.735	17.08
J094254.27+340411.8	145.726	34.070	0.023	643.652	2.579	19.01
J094809.89+425713.5	147.041	42.954	0.017	1601.710	2.692	17.39
J095000.77+300341	147.503	30.061	0.017	1484.470	2.506	17.32
J095023.31+004229.2	147.597	0.708	0.098	1231.630	3.995	18.60
J095131.76+525936	147.882	52.993	0.046	1860.920	3.758	17.47
J095226.96+021759.8	148.112	2.300	0.119	1002.630	3.970	18.41
J095227.53+322809.4	148.115	32.469	0.015	1484.210	2.463	16.89
J095545.56+413429.8	148.940	41.575	0.016	1951.340	2.740	16.19
J100720.49+193349.5	151.835	19.564	0.031	592.760	2.637	18.76

Continued on Next Page. . .

Table 5.2 – Continued

Name	R.A. (deg) (J2000)	Dec. (deg) (J2000)	z	Hβ flux (10^{-17} erg s^{-1}cm^{-2})	Hβ FWHM (Å)	Mag (g)
J100746.51+025228.4	151.944	2.875	0.024	1806.920	2.845	17.73
J101036.63+641242.6	152.653	64.212	0.040	2348.790	3.968	17.08
J101042.53+125516.7	152.677	12.921	0.061	3186.550	3.681	17.05
J101136.05+263027.5	152.900	26.508	0.055	906.885	2.925	18.19
J101157.08+130822.1	152.988	13.139	0.144	863.927	3.714	19.84
J101430.97+004755.0	153.629	0.799	0.147	736.971	4.092	18.65
J101458.64+193219.5	153.744	19.539	0.013	493.033	2.726	18.73
J102429.25+052451	156.122	5.414	0.033	2740.080	2.802	16.77
102732-284201	156.883	-28.700	——	——	——	——
J103226.95+271755.2	158.112	27.299	0.192	531.843	4.122	19.68
J103328.52+070801.7	158.369	7.134	0.045	3889.220	3.664	16.23
J103411.73+014247.2	158.549	1.713	——	481.560	3.200	16.24
J103509.33+094516.7	158.789	9.755	0.049	768.406	3.093	18.37
J103726.54+270759.6	159.361	27.133	0.077	636.101	3.404	18.26
J104457.79+035313.1	161.241	3.887	0.013	4209.360	3.248	17.48
J104554.77+010405.8	161.478	1.068	0.026	3888.740	2.874	16.56
J104653.98+134645.7	161.725	13.779	0.011	1845.540	2.606	17.54
J104723.6+302144.2	161.848	30.362	0.029	4889.010	3.154	15.93
J104755.92+073951.1	161.983	7.664	0.168	664.981	4.504	19.91
J104829.22+111520.1	162.122	11.256	0.093	704.205	3.287	18.86
J105032.51+153806.3	162.635	15.635	0.085	2444.490	3.200	18.24
J105040.83+342947.2	162.670	34.496	0.052	1433.410	3.253	17.68
J105108.88+131927.9	162.787	13.324	0.045	629.329	3.101	18.06
J105210.41+032713.2	163.043	3.454	0.150	417.647	3.788	19.14
J105326.02+043014.4	163.358	4.504	0.019	1096.980	2.932	17.66
J105331.40+011740.4	163.381	1.295	0.124	761.683	3.942	18.51
J105741.94+653539.8	164.425	65.594	0.011	1664.520	2.940	16.11
J105940.97+080056.8	164.921	8.016	0.027	1352.170	3.123	17.69
J110838.50+223809.7	167.160	22.636	0.024	1727.950	2.961	17.79
J114212.21+002004.0	175.551	0.334	——	6897.220	3.117	14.34
J115023.85-003141.0	177.599	-0.528	——	——	——	16.50
J121329.49+114056.8	183.373	11.682	0.021	2154.400	2.859	17.02
121717-280233	184.321	-28.043	——	——	——	——
J125305.97-031258.8	193.275	-3.216	0.023	19097.400	3.709	15.20
J130119.25+123959.5	195.330	12.667	0.069	2256.900	4.261	17.57
J131235.33+125744.5	198.147	12.962		1463.110	2.684	19.94
J132347.46-013252.0	200.948	-1.548	0.023	1562.150	2.957	18.15
J132549.42+330354.3	201.456	33.065	0.015	3833.200	2.581	16.60
133708-325528	204.283	-32.924	——	——	——	——
J134531.50+044232.7	206.381	4.709	0.030	1669.010	3.051	17.64
J142342.87+225728.7	215.929	22.958	0.033	1782.250	3.458	17.85
J144805.37-011057.6	222.022	-1.183		4850.170	3.302	21.83
J162152.57+151856.0	245.469	15.316	0.034	3184.830	3.595	16.98
J171236.63+321633.4	258.153	32.276	0.012	1512.660	2.503	17.52
192758-413432	291.992	-41.576	——	——	——	——

Continued on Next Page...

Table 5.2 – Continued

Name	R.A. (deg) (J2000)	Dec. (deg) (J2000)	z	Hβ flux (10^{-17} erg s^{-1}cm^{-2})	Hβ FWHM (Å)	Mag (g)
J210114.39-055510.3	315.310	-5.920	0.196	529.060	4.271	19.46
J210501.5-062238.8	316.256	-6.377	0.143	466.403	3.404	18.80
J211527.07-075951.3	318.863	-7.998	0.028	1267.590	2.709	17.93
J211902.28-074226.8	319.760	-7.707	0.090	522.035	3.221	18.37
J212043.95+010006.9	320.183	1.002	0.114	698.367	4.617	18.43
J212332.71-074831.1	320.886	-7.809	0.028	510.141	2.932	18.15
J214350.86-072003.6	325.962	-7.334	0.110	475.440	3.745	18.94
J220802.87+131334.5	332.012	13.226	0.116	608.787	3.897	18.62
J221823.85+003918.4	334.599	0.655	0.108	387.723	3.501	19.36
J222510.13-001152.8	336.292	-0.198	0.067	1461.150	3.419	18.40
J224556.93+125022.3	341.487	12.840	0.081	1299.470	3.642	18.03
J225140.31+132713.4	342.918	13.454	0.062	2100.980	3.413	16.65
J230117.65+135230.2	345.324	13.875	0.025	1034.660	2.920	17.62
J230123.59+133314.7	345.348	13.554	0.030	1854.490	2.948	16.98
J230703.74+011311.2	346.766	1.220	0.126	996.506	4.180	18.29
J231442.13+010621.1	348.676	1.106	0.034	519.005	2.661	17.74
J232936.55-011056.9	352.402	-1.182	0.066	846.007	3.158	18.03

5.4 Preliminary Results

The measurements from the above described observations have been analysed as described in Section 4.1. The analytic procedures have been implemented in an IDL (Interactive Data Language) code.

Figure 5.7 shows a preliminary $L(\mathrm{H}\beta) - \sigma$ correlation where the σ values have been obtained from the observations and the $L(\mathrm{H}\beta)$ values have been derived from the fluxes taken from the SDSS DR7 spectroscopic data. Here we have not yet considered any of the possible systematics. The solid line in the figure represents a least squares fit to the data, where the errors in both σ and $L(\mathrm{H}\beta)$ have been considered.

The $L(\mathrm{H}\beta) - \sigma$ relation obtained is given by

$$\log_{10} L(\mathrm{H}\beta) = (3.95 \pm 0.10) \log_{10} \sigma + (34.68 \pm 0.17) \quad \delta \log_{10} L(\mathrm{H}\beta) = 0.299,$$

(5.2)

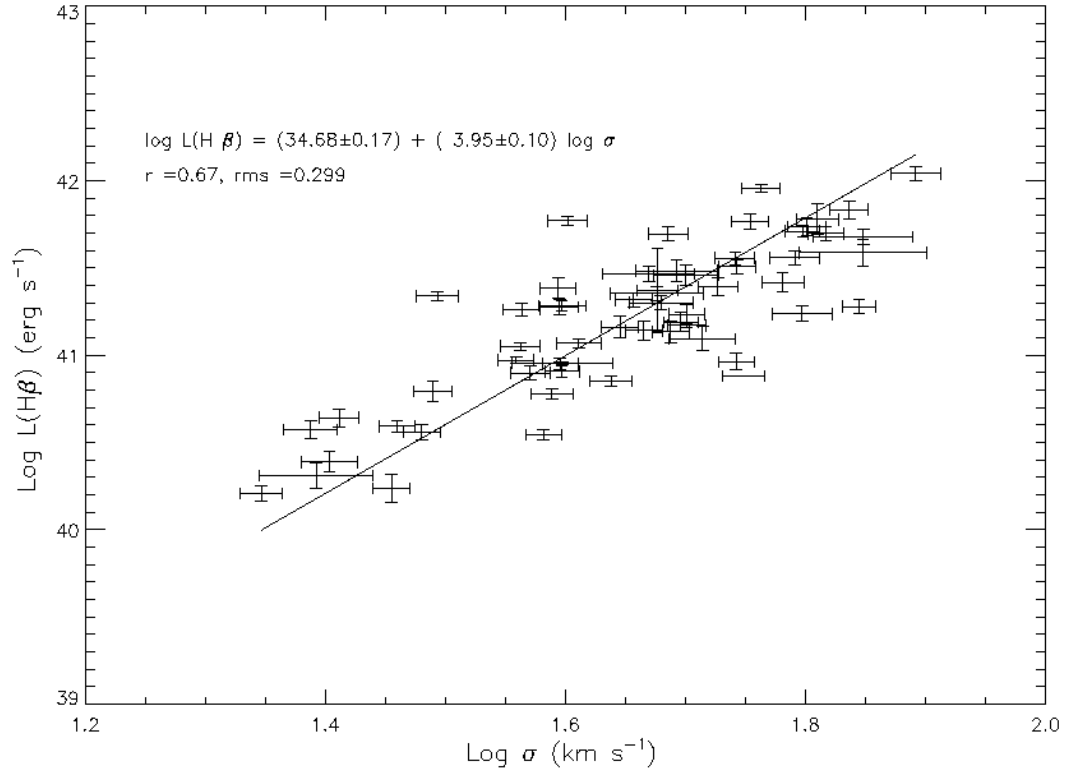this relation is similar to the one obtained by Melnick et al. (1988). We reproduce it

Figure 5.7: $L(\mathrm{H}\beta) - \sigma$ preliminary correlation. The σ values have been obtained from the observations whereas the $L(\mathrm{H}\beta)$ values have been derived from the fluxes taken from the SDSS DR7 spectroscopic data. The solid line shows a least squares fit to the data.

here from equation (3.1):

$$\log_{10} L(\mathrm{H}\beta) = (4.70 \pm 0.30)\log_{10}\sigma + (33.61 \pm 0.50) \quad \delta\log_{10} L(\mathrm{H}\beta) = 0.29.$$

Form Figure 5.7 and the above equation it is clear that a considerable dispersion in the data is present, therefore a careful analysis of the possible systematics (i.e. metallicity, age, environment, morphology) is necessary. Furthermore, the integrated $\mathrm{H}\beta$ fluxes obtained from the low resolution long-slit spectroscopy will be used in the correlation in order to correct for any flux loses or errors present in the SDSS DR7 data.

The preliminary results reported here are based in a subsample of only 59 H II galaxies, the reason for that is that many objects have been excluded since their SDSS DR7 spectrum is of poor quality, with missing lines or clearly spurious features.

In the next chapter I describe the work that is necessary to do in order to improve the $L(\mathrm{H}\beta) - \sigma$ relation taking care of all the possible systematics and with a better determination of the $\mathrm{H}\beta$ fluxes for the entire 128 galaxies sample. In addition, I describe the work that I plan to do in order to obtain improved cosmological constraints from the intermediate and high-z H II galaxies sample.

Chapter 6

Future Work and Concluding Remarks

Through this chapter we describe the work to do during the doctoral research and give a set of conclusions to this work.

The future work can be thought basically in terms of two partial objectives that must be accomplished in order to fulfill our main objective:

1. To improve the $L(\mathrm{H}\beta) - \sigma$ relation for H II galaxies using the better possible data and taking care of all the possible systematics.

2. To obtain high quality velocity dispersion data for a sample of intermediate and high-z H II galaxies and using the improved $L(\mathrm{H}\beta) - \sigma$ relation to construct a H II galaxies Hubble diagram to high-z.

Having accomplished the above two partial objectives, we will use the Hubble diagram of H II galaxies (possibly combined with SNe Ia data) to put stringent constraints to the dark energy equation of state (i.e. the expansion history of the Universe).

Through the first section of this chapter we explore the work to do in order to achieve the above mentioned first objective, whereas the second section explores the work to do in order to arrive at the second objective. Finally, conclusions to this work are given in the third section.

6.1 Improving the $L(\mathrm{H}\beta) - \sigma$ Relation

In order to improve the $L(\mathrm{H}\beta) - \sigma$ relation we will need accurate integrated flux measurements for the local H II galaxies sample from long-slit spectroscopy. By now we have measurements for ~ 50 % of the 128 objects of our selected sample, and therefore we need to obtain the measurements for the rest of the sample.

To accomplish our aim of measuring the integrated fluxes of the entire local sample of H II galaxies, we already have been allocated 3 observing nights (8th to 10th October 2010) at OAN 2.12 m telescope and another 5 observing nights at the OAGH 2.12 m telescope in December 2010.

In parallel with the integrated fluxes data acquisition, we must analyse the effect of possible systematics over the $L(\mathrm{H}\beta) - \sigma$ relation of H II galaxies, such as metallicity, age, environment and morphology. The metallicity, morphology and environment analysis can be performed, for a good fraction of the sample, using the SDSS spectroscopic and photometric data.

The improved $L(\mathrm{H}\beta) - \sigma$ relation of H II galaxies is a fundamental fist step in order to eventually obtain stringent constraints of cosmological parameters, since it will permit us to construct a Hubble diagram for H II galaxies and increase the probability of being allocated observing time at 8 m class telescopes in order to observe the intermediate and high-z sample of H II galaxies.

6.2 Cosmological Constraints from H II Galaxies

The construction of the Hubble diagram of H II galaxies to high-z is the fundamental mean to fulfill our main objective which is to obtain stringent constraints for the dark energy equation of state.

Among the important tasks to perform is the selection of the intermediate and high-z samples form the literature. This must be achieved first in order to request observing time for the corresponding measurements at 8 m class telescopes, which is the natural next step.

The task of measuring the velocity dispersion of the intermediate and high-z sample is critical for the accomplishment of our objectives. Having the velocity dispersion

data, the construction of the Hubble diagram of H II galaxies and its analysis, in order to constrain the cosmological parameters, will be the final tasks for this project.

6.3 Concluding Remarks

The cosmic acceleration problem is one of the most important open issues in the whole of physics. Its solution could shed light over many other important problems in physics and astronomy.

The observational evidence for the cosmic acceleration is strong and originates in many distinct probes. All the current probes are limited by systematic errors, that in many cases require a better comprehension.

The physical mechanism responsible for the cosmic acceleration is unclear. The current evidence is consistent with a cosmological constant but without ruling out dark energy theories or some other dynamical models. Form the theoretical side, the vacuum energy theories face the cosmological constant problem.

Large observational efforts are necessary in order to better constrain the dark energy equation of state parameters. We have shown that the use of tracers to high-z is a better option that an increase in the number of tracers, if we try to obtain better constraints.

We have proposed the use of H II galaxies $L(\text{H}\beta) - \sigma$ relation, to determine the Hubble function to intermediate and high redshifts and to obtain stringent constraints for the dark energy equation of state. We have shown that a good determination of the zero point and a reduction of the scatter of the $L(\text{H}\beta) - \sigma$ relation are necessary; in addition we must take care of all possible systematics that could affect this correlation, in order to succeed in our aims.

We have presented a preliminary H II galaxies $L(\text{H}\beta) - \sigma$ relation, given by

$$\log_{10} L(\text{H}\beta) = (3.95 \pm 0.10) \log_{10} \sigma + (34.68 \pm 0.17) \quad \delta \log_{10} L(\text{H}\beta) = 0.299,$$

which is similar to the one obtained in previous works. We hope to improve it by using better integrated flux determinations and taking care of all the possible systematics.

In the future we hope to improve the H II galaxies $L(\text{H}\beta) - \sigma$ relation and to select, measure and analyse an intermediate and high-z sample of H II galaxies in order to

determine the Hubble function to a redshift high enough to obtain stringent constraints for the dark energy equation of state parameters.

Appendices

Appendix A

Cosmological Field Equations

The purpose of this appendix is to derive the Cosmological Field Equations from the General Relativity (GR) Field Equations; the approach followed for the derivation is variational since this method is intuitive, easy to follow and, not the least, very powerful.

A.1 The General Relativity Field Equations

The GR Field Equations can be written as

$$R_{\mu\nu} - \frac{1}{2}g_{\mu\nu}R + \Lambda g_{\mu\nu} = -\kappa T_{\mu\nu}, \tag{A.1}$$

or alternatively as

$$R_{\mu\nu} = -\kappa \left(T_{\mu\nu} - \frac{1}{2}T g_{\mu\nu} \right) + \Lambda g_{\mu\nu}, \tag{A.2}$$

where $R_{\mu\nu}$ is the Ricci Tensor, $T_{\mu\nu}$ is the Energy-Momentum Tensor, $g_{\mu\nu}$ is the Metric Tensor, Λ is the cosmological constant and κ is a constant given by

$$\kappa = 8\pi G, \tag{A.3}$$

note that we are using units in which $c = 1$.

Our general approach to obtain the GR field equations for the FRW metric will be simply to obtain variationaly the Ricci Tensor and then to use the value of the Energy-Momentum Tensor for a perfect fluid to obtain the right-hand side of the GR field equations.

A.2 The Euler-Lagrange Equations

From the calculus of variations we know that if we like to find a function that makes an integral dependent on that function stationary, on a certain interval, we can proceed as follows; first we have the integral that we like to make stationary

$$S = \int_a^b L(q^a, \dot{q}^a, t)dt, \tag{A.4}$$

where we define S as the action, L is the Lagrangian which is dependent on q^a, a set of generalized coordinates (a is an index running over all the elements of the set), $\dot{q}^a$, the set of the generalized coordinates time derivatives, $\dot{q}^a \equiv dq^a/dt$ and t, the time, a parameter.

The variation of the action can be written as

$$\delta S = \int_a^b \left(\frac{\partial L}{\partial q^a} \delta q^a + \frac{\partial L}{\partial \dot{q}^a} \delta \dot{q}^a \right) dt \tag{A.5}$$

$$= \int_a^b \frac{\partial L}{\partial q^a} \delta q^a dt + \int_a^b \frac{\partial L}{\partial \dot{q}^a} \delta \dot{q}^a dt, \tag{A.6}$$

integrating the last term by parts and requiring the variation δS to be zero (the condition for S to be stationary), we have

$$\int_a^b \frac{\partial L}{\partial q^a} \delta q^a dt + \left[\frac{\partial L}{\partial \dot{q}^a} \delta q^a \right]_a^b - \int_a^b \frac{d}{dt} \left(\frac{\partial L}{\partial \dot{q}^a} \right) \delta q^a dt = 0 \tag{A.7}$$

$$\left[\frac{\partial L}{\partial \dot{q}^a} \delta q^a \right]_a^b + \int_a^b \left[\frac{\partial L}{\partial q^a} - \frac{d}{dt} \left(\frac{\partial L}{\partial \dot{q}^a} \right) \right] \delta q^a dt = 0, \tag{A.8}$$

since a and b are fixed then the first term vanishes and in order for the integral to be zero, since δq^a is arbitrary, then

$$\frac{d}{dt} \left(\frac{\partial L}{\partial \dot{q}^a} \right) - \frac{\partial L}{\partial q^a} = 0 \tag{A.9}$$

These are the Euler-Lagrange equations that must be satisfied in order to make the action stationary.

A.3 Variational Method for Geodesics

In order to obtain the equations for the geodesics, and from them read out the metric connection coefficients, we must solve the Euler-Lagrange equations for the Lagrangian

$$L = \frac{1}{2} g_{ab} \dot{x}^a \dot{x}^b, \tag{A.10}$$

where g_{ab} are the metric elements and $\dot{x}^a$ are the coordinates time derivatives. Applying the Euler-Lagrange equations over the Lagrangian we obtain

$$\frac{d}{dt}(g_{ac}\dot{x}^a) - \frac{1}{2}(\partial_c g_{ab})\dot{x}^a \dot{x}^b = 0 \tag{A.11}$$

$$\dot{g}_{ac}\dot{x}^a + g_{ac}\ddot{x}^a - \frac{1}{2}(\partial_c g_{ab})\dot{x}^a \dot{x}^b = 0 \tag{A.12}$$

$$(\partial_b g_{ac})\dot{x}^a \dot{x}^b + g_{ac}\ddot{x}^a - \frac{1}{2}(\partial_c g_{ab})\dot{x}^a \dot{x}^b = 0 \tag{A.13}$$

$$g_{ac}\ddot{x}^a + (\partial_b g_{ac})\dot{x}^a \dot{x}^b - \frac{1}{2}(\partial_c g_{ab})\dot{x}^a \dot{x}^b = 0, \tag{A.14}$$

since $\dot{x}^a$ and $\dot{x}^b$ commutes, then we have

$$g_{ac}\ddot{x}^a + \frac{1}{2}(\partial_b g_{ac} + \partial_a g_{bc} - \partial_c g_{ab})\dot{x}^a \dot{x}^b = 0 \tag{A.15}$$

$$g^{dc}[\ddot{x}^a + \frac{1}{2}(\partial_b g_{ac} + \partial_a g_{bc} - \partial_c g_{ab})\dot{x}^a \dot{x}^b] = 0 \tag{A.16}$$

$$\ddot{x}^d + \frac{1}{2}g^{dc}(\partial_b g_{ac} + \partial_a g_{bc} - \partial_c g_{ab})\dot{x}^a \dot{x}^b = 0 \tag{A.17}$$

$$\ddot{x}^d + \Gamma^d_{ab}\dot{x}^a \dot{x}^b = 0 \tag{A.18}$$

$$\ddot{x}^a + \Gamma^a_{bc}\dot{x}^b \dot{x}^c = 0, \tag{A.19}$$

where Γ^a_{bc} are the metric connection coefficients and were clearly defined as

$$\Gamma^a_{bc} = \frac{1}{2}g^{dc}(\partial_b g_{ac} + \partial_a g_{bc} - \partial_c g_{ab}) \tag{A.20}$$

and from (A.17) we can read without effort the metric connection coefficients.

A.4 Application to the FRW Metric

Using the FRW metric a distance element can be written as

$$ds^2 = dt^2 - a^2(t)\left[\frac{dr^2}{1 - kr^2} + r^2(d\theta^2 + \sin^2\theta d\phi^2)\right] \tag{A.21}$$

then the metric is given by

$$[g_{ab}] = \begin{pmatrix} 1 & 0 & 0 & 0 \\ 0 & -\frac{a^2(t)}{1-kr^2} & 0 & 0 \\ 0 & 0 & -a^2(t)r^2 & 0 \\ 0 & 0 & 0 & -a^2(t)r^2\sin^2\theta \end{pmatrix}. \tag{A.22}$$

From the previous section, equation (A.14) is the easiest to use; then we will apply this equation successively for values of the index c running from 0 to 3. In the case in which $c = 0$ we have

$$g_{00}\ddot{x}^0 - \frac{1}{2}[(\partial_0 g_{11})\dot{x}^1\dot{x}^1 + (\partial_0 g_{22})\dot{x}^2\dot{x}^2 + (\partial_0 g_{33})\dot{x}^3\dot{x}^3] = 0, \tag{A.23}$$

then substituting and solving we obtain

$$\ddot{t} + \frac{a\dot{a}}{1-kr^2}(\dot{r})^2 + a\dot{a}r^2(\dot{\theta})^2 + a\dot{a}r^2\sin^2\theta(\dot{\phi})^2 = 0, \tag{A.24}$$

from here we can read the metric connection coefficients

$$\Gamma^0_{11} = \frac{a\dot{a}}{1-kr^2} \tag{A.25}$$

$$\Gamma^0_{22} = a\dot{a}r^2 \tag{A.26}$$

$$\Gamma^0_{33} = a\dot{a}r^2\sin^2\theta. \tag{A.27}$$

For the case when $c = 1$ we have

$$g_{11}\ddot{x}^1 + (\partial_0 g_{11})\dot{x}^1\dot{x}^0 + (\partial_1 g_{11})\dot{x}^1\dot{x}^1 - \frac{1}{2}[(\partial_1 g_{11})\dot{x}^1\dot{x}^1 + (\partial_1 g_{22})\dot{x}^2\dot{x}^2 + (\partial_1 g_{33})\dot{x}^3\dot{x}^3] = 0, \tag{A.28}$$

then substituting and solving we obtain

$$\ddot{r} + 2\frac{\dot{a}}{a}\dot{t}\dot{r} + \frac{kr}{1-kr^2}(\dot{r})^2 - r(1-kr^2)(\dot{\theta})^2 - r(1-kr^2)\sin^2\theta(\dot{\phi})^2 = 0, \tag{A.29}$$

from here we can read the metric connection coefficients

$$\Gamma^1_{01} = \frac{\dot{a}}{a} \tag{A.30}$$

$$\Gamma^1_{11} = \frac{kr}{1-kr^2} \tag{A.31}$$

$$\Gamma^1_{22} = -r(1-kr^2) \tag{A.32}$$

$$\Gamma^1_{33} = -r(1-kr^2)\sin^2\theta. \tag{A.33}$$

For the case when $c = 2$ we have

$$g_{22}\ddot{x}^2 + (\partial_0 g_{22})\dot{x}^2\dot{x}^0 + (\partial_1 g_{22})\dot{x}^2\dot{x}^1 - \frac{1}{2}(\partial_2 g_{33})\dot{x}^3\dot{x}^3 = 0, \tag{A.34}$$

then substituting and solving we obtain

$$\ddot{\theta} + 2\frac{\dot{a}}{a}\dot{\theta}\dot{t} + 2\frac{1}{r}\dot{\theta}\dot{r} - \sin\theta\cos\theta(\dot{\phi})^2 = 0, \tag{A.35}$$

from here we can read the metric connection coefficients

$$\Gamma^2_{02} = \frac{\dot{a}}{a} \tag{A.36}$$

$$\Gamma^2_{12} = \frac{1}{r} \tag{A.37}$$

$$\Gamma^2_{33} = -\sin\theta\cos\theta. \tag{A.38}$$

For the case when $c = 3$ we have

$$g_{33}\ddot{x}^3 + (\partial_0 g_{33})\dot{x}^3\dot{x}^0 + (\partial_1 g_{33})\dot{x}^3\dot{x}^1 + (\partial_2 g_{33})\dot{x}^3\dot{x}^2 = 0, \tag{A.39}$$

then substituting and solving we obtain

$$\ddot{\phi} + 2\frac{\dot{a}}{a}\dot{\phi}\dot{t} + 2\frac{1}{r}\dot{\phi}\dot{r} + 2\frac{\cos\theta}{\sin\theta}\dot{\phi}\dot{\theta} = 0, \tag{A.40}$$

from here we can read the metric connection coefficients

$$\Gamma^3_{03} = \frac{\dot{a}}{a} \tag{A.41}$$

$$\Gamma^3_{12} = \frac{1}{r} \tag{A.42}$$

$$\Gamma^3_{23} = \frac{\cos\theta}{\sin\theta} = \cot\theta. \tag{A.43}$$

A.5   Obtaining the Ricci Tensor

Having the metric connection coefficients, the next step is to obtain the independent values of the Ricci tensor which is given by

$$R_{\mu\nu} = \partial_\nu\Gamma^\sigma_{\mu\sigma} - \partial_\sigma\Gamma^\sigma_{\mu\nu} + \Gamma^\rho_{\mu\sigma}\Gamma^\sigma_{\rho\nu} - \Gamma^\rho_{\mu\nu}\Gamma^\sigma_{\rho\sigma}. \tag{A.44}$$

From the metric connection coefficients we obtain that

$$
\begin{aligned}
R_{00} &= 3\partial_0\Gamma^1_{01} + 3(\Gamma^1_{01})^2 & \text{(A.45)}\\
&= 3\left[\left(\frac{\ddot{a}}{a} - \left(\frac{\dot{a}}{a}\right)^2\right) + \left(\frac{\dot{a}}{a}\right)^2\right] & \text{(A.46)}\\
&= 3\frac{\ddot{a}}{a}, & \text{(A.47)}
\end{aligned}
$$

for R_{11} we obtain

$$
\begin{aligned}
R_{11} &= 2\partial_1\Gamma^2_{12} - \partial_0\Gamma^0_{11} - \Gamma^0_{11}\Gamma^1_{01} - 2\Gamma^1_{11}\Gamma^2_{12} + 2(\Gamma^2_{12})^2 & \text{(A.48)}\\
&= -\frac{2}{r^2} - \frac{(\dot{a}^2 + a\ddot{a})}{1 - kr^2} - \frac{\dot{a}^2}{1 - kr^2} - \frac{2k}{1 - kr^2} + \frac{2}{r^2} & \text{(A.49)}\\
&= -\frac{a\ddot{a} + 2\dot{a}^2 + 2k}{1 - kr^2}, & \text{(A.50)}
\end{aligned}
$$

for R_{22} we have

$$
\begin{aligned}
R_{22} &= \partial_2\Gamma^3_{23} - \partial_0\Gamma^0_{22} - \partial_1\Gamma^1_{22} + 2\Gamma^0_{22}\Gamma^2_{02} + 2\Gamma^1_{22}\Gamma^2_{12} + (\Gamma^3_{23})^2 & \text{(A.51)}\\
&\quad -3\Gamma^0_{22}\Gamma^1_{01} - \Gamma^1_{22}\Gamma^1_{11} - 2\Gamma^1_{22}\Gamma^2_{12}\\
&= -\csc^2\theta - r^2(\dot{a}^2 + \ddot{a}a) + (1 - kr^2) - 2kr^2 + 2r^2\dot{a}^2 & \text{(A.52)}\\
&\quad -2(1 - kr^2) + \cot^2\theta - 3r^2\dot{a}^2 + kr^2 + 2(1 - kr^2)\\
&= -r^2(a\ddot{a} + 2\dot{a}^2 + 2k), & \text{(A.53)}
\end{aligned}
$$

finally for R_{33} we have

$$
\begin{aligned}
R_{33} &= -\partial_0\Gamma^0_{33} - \partial_1\Gamma^1_{33} - \partial_2\Gamma^2_{33} + 2\Gamma^0_{33}\Gamma^3_{03} + 2\Gamma^1_{33}\Gamma^3_{13} + 2\Gamma^2_{33}\Gamma^3_{23} & \text{(A.54)}\\
&\quad -3\Gamma^0_{33}\Gamma^1_{01} - \Gamma^1_{33}\Gamma^1_{11} - 2\Gamma^1_{33}\Gamma^2_{12} - \Gamma^2_{33}\Gamma^3_{23}\\
&= -r^2\sin^2\theta(\dot{a}^2 + a\ddot{a}) - 3kr^2\sin^2\theta + \sin^2\theta + \cos^2\theta - \sin^2\theta & \text{(A.55)}\\
&\quad +2r^2\sin^2\theta\dot{a}^2 - 2\sin^2\theta(1 - kr^2) - 2\cos^2\theta - 3r^2\sin^2\theta\dot{a}^2\\
&\quad +kr^2\sin^2\theta + 2\sin^2\theta(1 - kr^2) + \cos\theta\\
&= -r^2\sin^2\theta(a\ddot{a} + 2\dot{a}^2 + 2k) & \text{(A.56)}
\end{aligned}
$$

A.6 The Energy-Momentum Tensor

In order to simplify we will assume that the matter that fills the Universe can be characterized as a perfect fluid, this assumption implies that we are neglecting any

shear-viscous, bulk-viscous and heat-conductive properties of the matter (Hobson et al., 2005). The energy-momentum tensor is given by

$$T^{\mu\nu} = (\rho + p)u^\mu u^\nu - pg^{\mu\nu}. \tag{A.57}$$

Since in a comoving coordinate system the 4-velocity is given simply by $u^\mu = \delta_0^\mu$ and $u_\mu = \delta_\mu^0$, then we have

$$T_{\mu\nu} = (\rho + p)\delta_\mu^0 \delta_\nu^0 - pg_{\mu\nu}. \tag{A.58}$$

For the contracted energy-momentum tensor we have

$$\begin{align}
T &= T_\mu^\mu \tag{A.59} \\
&= (\rho + p) - p\delta_\mu^\mu \tag{A.60} \\
&= \rho + p - 4p \tag{A.61} \\
&= \rho - 3p, \tag{A.62}
\end{align}$$

then, we have that

$$\begin{align}
T_{\mu\nu} - \frac{1}{2}Tg_{\mu\nu} &= (\rho + p)\delta_\mu^0 \delta_\nu^0 - pg_{\mu\nu} - \frac{1}{2}(\rho - 3p)g_{\mu\nu} \tag{A.63} \\
&= (\rho + p)\delta_\mu^0 \delta_\nu^0 - \frac{1}{2}(\rho + p)g_{\mu\nu}, \tag{A.64}
\end{align}$$

from here we can substitute in the right hand side of (A.2) to obtain

$$\begin{align}
-\kappa(T_{00} - \frac{1}{2}Tg_{00}) + \Lambda g_{00} &= -\frac{1}{2}\kappa(\rho + 3p) + \Lambda \tag{A.65} \\
-\kappa(T_{11} - \frac{1}{2}Tg_{11}) + \Lambda g_{11} &= -\left[\frac{1}{2}(\rho - p) + \Lambda\right]\frac{a^2}{1 - kr^2} \tag{A.66} \\
-\kappa(T_{22} - \frac{1}{2}Tg_{22}) + \Lambda g_{22} &= -\left[\frac{1}{2}(\rho - p) + \Lambda\right]a^2r^2 \tag{A.67} \\
-\kappa(T_{33} - \frac{1}{2}Tg_{33}) + \Lambda g_{33} &= -\left[\frac{1}{2}(\rho - p) + \Lambda\right]a^2r^2\sin^2\theta. \tag{A.68}
\end{align}$$

A.7   The Cosmological Field Equations

In the two previous sections we have derived both sides of the GR Field Equations, then at this point the reamaining step is to combine these results to obtain the Cosmological

Field Equations. For R_{00} we have

$$3\frac{\ddot{a}}{a} = -\frac{1}{2}\kappa(\rho + 3p) + \Lambda \tag{A.69}$$

$$3\frac{\ddot{a}}{a} = -\frac{8\pi G}{2}(\rho + 3p) + \Lambda \tag{A.70}$$

$$\frac{\ddot{a}}{a} = -\frac{4\pi G}{3}(\rho + 3p) + \frac{1}{3}\Lambda; \tag{A.71}$$

for R_{11} we have

$$-\frac{a\ddot{a} + 2\dot{a}^2 + 2k}{1 - kr^2} = -\left[\frac{1}{2}\kappa(\rho - p) + \Lambda\right]\frac{a^2}{1 - kr^2} \tag{A.72}$$

$$a\ddot{a} + 2\dot{a}^2 + 2k = (4\pi G(\rho - p) + \Lambda)a^2, \tag{A.73}$$

substituting the value for $\ddot{a}$ from (A.71) we have

$$-\frac{4\pi G}{3}(\rho + 3p)a^2 + \frac{1}{3}\Lambda a^2 + 2\dot{a}^2 + 2k = 4\pi G(\rho - p)a^2 + \Lambda a^2 \tag{A.74}$$

$$2\dot{a}^2 = \frac{4\pi G}{3}(4\rho)a^2 + \frac{2}{3}\Lambda a^2 - 2k \tag{A.75}$$

$$\left(\frac{\dot{a}}{a}\right)^2 = \frac{8\pi G\rho}{3} - \frac{k}{a^2} + \frac{\Lambda}{3}; \tag{A.76}$$

for R_{22} we have

$$-r^2(a\ddot{a} + 2\dot{a}^2 + 2k) = -\left[\frac{1}{2}\kappa(\rho - p) + \Lambda\right]a^2r^2 \tag{A.77}$$

$$a\ddot{a} + 2\dot{a}^2 + 2k = (4\pi G(\rho - p) + \Lambda)a^2, \tag{A.78}$$

we have obtained (A.73), then the equation given by R_{22} is not independent. For R_{33} we have

$$-r^2\sin^2\theta(a\ddot{a} + 2\dot{a}^2 + 2k) = -\left[\frac{1}{2}\kappa(\rho - p) + \Lambda\right]a^2r^2\sin^2\theta \tag{A.79}$$

$$a\ddot{a} + 2\dot{a}^2 + 2k = (4\pi G(\rho - p) + \Lambda)a^2, \tag{A.80}$$

anew, we have obtained (A.73) and then the equation R_{33} is redundant.

From the previous discusion, only two of the four equations are independent (equation (A.71) and equation (A.76)):

$$\frac{\ddot{a}}{a} = -\frac{4\pi G}{3}(\rho + 3p) + \frac{1}{3}\Lambda \tag{A.81}$$

$$\left(\frac{\dot{a}}{a}\right)^2 = \frac{8\pi G\rho}{3} - \frac{k}{a^2} + \frac{\Lambda}{3}, \tag{A.82}$$

these are the Cosmological Field Equations.

Appendix B

Statistical Techniques in Cosmology

In order to analyse the large data sets that are now available for cosmological work it is absolutely necessary the use of more and more sophisticated statistical tools. Here we present a few basic statistical techniques that are used through this work and that in general can be applied in cosmological data sets analysis. Through this appendix we closely follow the work of Verde (2010).

B.1 Bayes Theorem and Statistical Inference

The fundamental rules of probability are (hereafter $\mathcal{P}$ is the probability of an event):

1. $\mathcal{P} \geq 0$.

2. $\int_{-\infty}^{\infty} dx \mathcal{P}(x) = 1$.

3. For mutually exclusive events $\mathcal{P}(x \cup y) = \mathcal{P}(x) + \mathcal{P}(y)$.

4. For dependent events $\mathcal{P}(x \cap y) = \mathcal{P}(x)\mathcal{P}(y|x)$, where $\mathcal{P}(y|x)$ is the conditional probability of y given that x has already occurred.

from the last relation we can derive the Bayes theorem (writing $\mathcal{P}(x, y) = \mathcal{P}(y, x)$):

$$\mathcal{P}(H|D) = \frac{\mathcal{P}(H)\mathcal{P}(D|H)}{\mathcal{P}(D)} \tag{B.1}$$

where D stands for *data*, H for *hypothesis* or model, $\mathcal{P}(H|D)$ is called the *posterior*, $\mathcal{P}(D|H)$ is the *likelihood* and $\mathcal{P}(H)$ is called the *prior*.

Bayes theorem is at the base of statistical inference, let us assume that we have some already collected data set, then $\mathcal{P}(D) = 1$, and we have a model characterized by some set of parameters $\mathbf{p}$, in general we want to know the probability distribution for the model parameters given the data $\mathcal{P}(\mathbf{p}|D)$ (from a bayesian view point as opposed to a frequentist one). However, usually we can compute accurately the likelihood which, by Bayes theorem, is related to the posterior by the prior.

One fundamental problem with the above approach is that the use of distinct priors leads to different posteriors since e.g. if we have a prior in two distinct equally valid variables, then we have a distinct probability distributions for every prior, say $\mathcal{P}(x)$ and $\mathcal{G}(y)$, then in order to transform from one distribution to the other one we have

$$\mathcal{P}(x)dx = \mathcal{G}(y)dy, \tag{B.2}$$

$$\mathcal{P}(x) = \mathcal{G}(y)\left|\frac{dy}{dx}\right|. \tag{B.3}$$

Another important concept is the marginalization procedure. If we have a multivariate distribution, say $\mathcal{P}(x, y)$ and we want to know the probability distribution $\mathcal{P}(x)$ regardless of the values of y, then we *marginalize* with respect to y:

$$\mathcal{P}(x) = \int dy \mathcal{P}(x, y). \tag{B.4}$$

B.2 Chi-square and Goodness of Fit

In order to find the model, characterized by a set of parameters $\mathbf{p}$, that better fit a given data set, we must define a merit function that quantifies the correspondence between the model and the data.

The least squares fitting is given by

$$\chi^2 = \sum_i w_i[D_i - y(x_i|\mathbf{p})]^2, \tag{B.5}$$

where D_i are the data points, $y(x_i|\mathbf{p})$ is the model and w_i are suitably defined weights. The minimum variance weight is $w_i = 1/\sigma_i^2$ where σ_i denotes the error on data point i. With these weights the least squares is called chi-square. The best fit parameters are those that minimize the χ^2.

If the data are correlated, the chi-square becomes

$$\chi^2 = \sum_{ij} [D_i - y(x_i|\mathbf{p})]Q_{ij}[D_j - y(x_j|\mathbf{p})], \tag{B.6}$$

where Q denotes the inverse of the covariance matrix.

The probability distribution for the values of χ^2 around its minimum value, is given by a χ^2 distribution for $\nu = n - m$ degrees of freedom, where n is the number of independent data points and m is the number of parameters. The probability that the value of χ^2 obtained from the fit exceeds by chance the value $\hat{\chi}$ for the *correct* model is $Q(\nu, \hat{\chi}) = 1 - \Gamma(\nu/2, \hat{\chi}/2)$ where Γ is the incomplete Gamma function. Q measures the goodness of the fit.

B.3   Likelihood

If in the Bayes theorem we take $\mathcal{P}(D) = 1$ since we assume that we already have the data, and $\mathcal{P}(H) = 1$ since we ignore the prior, then estimating the likelihood we obtain the posterior. However, since we have ignored the prior then we can not give the goodness of fit or the absolute probability for a model in which case we can only obtain relative probabilities. Assuming that the data are gaussianly distributed the likelihood is given by a multi-variate Gaussian:

$$\mathcal{L} = \frac{1}{(2\pi)^{n/2}|det(C)|^{1/2}} \exp\left[-\frac{1}{2}\sum_{ij}(D - y)_i C_{ij}^{-1}(D - y)_j\right], \tag{B.7}$$

where C_{ij} is the covariance matrix.

For Gaussian distributions we have $\mathcal{L} \propto \exp[-1/2\chi^2]$ and minimizing the χ^2 is equivalent to maximizing the likelihood.

The likelihood ratio is used in order to obtain results independently of the prior, it is the comparison between the likelihood at a point and the maximum likelihood, $\mathcal{L}_{max}$. Then, a model is acceptable if the likelihood ratio,

$$\Lambda = -2\ln\left[\frac{\mathcal{L}(p)}{\mathcal{L}_{max}}\right], \tag{B.8}$$

is above a given threshold.

83

B.4 Fisher Matrix

The Fisher matrix allows to estimate the parameters error for a given model. It is defined as

$$F_{ij} = - \left\langle \frac{\partial^2 \ln \mathcal{L}}{\partial p_i \partial p_j} \right\rangle, \tag{B.9}$$

where the average is the ensemble average over observational data (those that would be gathered if the real Universe was given by the model).

For a parameter i the marginalized error is given by

$$\sigma_{p_i} \geq (F^{-1})_{ii}^{1/2}, \tag{B.10}$$

this last equation is the Kramer-Rao inequality that implies that the Fisher matrix always gives an optimistic estimate of the errors. This inequality is an equality only if the likelihood is Gaussian, this happens when the data are gaussianly distributed and the model depends linearly on the parameters.

B.5 Monte Carlo Methods

The methodology of Monte Carlo methods for error analysis can be described as follows. Given a measured data set D_0, we can fit some model to it and obtain a set of parameters p_0 and their errors. With the intention of exploring the errors for p_0, we assume that the fitted parameters p_0 are the *true* ones. Subsequently, we construct an ensemble of simulated sets of parameters p_i^s taking care of the observational errors associated with the data set D_0. Finally, we can construct the distribution $p_i^s - p_0$ from which we can explore the parameters error.

The Monte Carlo methods for error determinations are specially useful when complicated effects can be simulated but not described analytically by a model.

Appendix C

The Cosmic Distance Ladder

From the relation (2.30) we can see that knowing the values for the absolute luminosity L and the flux f for an object we can obtain immediately the value of the luminosity distance D_L; if we obtain D_L and z for a great number of objects we can determine an approximate value for H_0, as can be seen from (2.35), or constrain the cosmological model by means of the relation (2.31); then the knowledge of D_L is of great importance, notwithstanding, the difficult problem is to determine the value of the absolute luminosity.

Conventionally, the objects used to measure distances in cosmology, are classified as primary and secondary distance indicators. The primary distance indicators are those whose absolute luminosities are measured either directly, by kinematic methods, or indirectly, by means of the association of these objects with others whose distance was measured by kinematic methods. The primary distance indicators are not bright enough to be studied at distances farther than the corresponding to values of z around 0.01. The secondary distance indicators are bright enough to be studied at larger distances and their absolute luminosities are known through their association with primary distance indicators (Weinberg, 2008); is by means of these last objects that we can constrain a cosmological model since, aside of other considerations, their value of z is large enough to make negligible the contribution of the peculiar velocities to the redshift determination.

C.1 Kinematic Methods to Distance Determinations

As already said, in cosmology the primary distance indicators are of importance as calibrators of the secondary distance indicators which can be used to constrain a cosmological model, but these primary distance indicators must be calibrated by means of distance determinations carried out by kinematic methods. Below we will briefly discuss the kinematic methods used to measure the distance to the primary distance indicators.
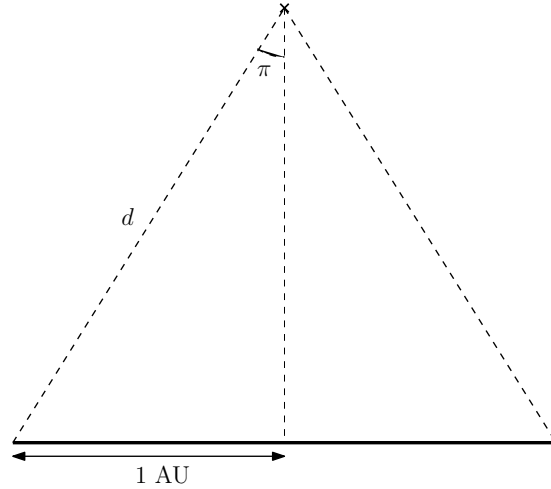
C.1.1 Trigonometric parallax

Figure C.1: Scheme illustrating the Trigonometric Parallax

While the earth's annual motion around the sun takes place, the stars appear to have an elliptical motion due to the true movement of our planet, the maximum angular radius of this motion is called parallax, π; this situation is schematized in Figure C.1. We can see that it is possible to calculate the actual distance to a star by means of an accurate measure of its parallax and knowing the mean distance between the sun and the earth, which is called an astronomical unit (AU). The distance to the star is given by

$$d = \frac{1 \text{ AU}}{\sin \pi},$$

(C.1)

if we assume that $\pi \ll 1 \text{ rad}$, which is the case for all the stars, then $\sin \pi \simeq \pi$, with

enough approximation; even more, if we give π in arcseconds, we obtain the relation

$$\frac{d}{\mathrm{pc}} = \left(\frac{\pi}{\mathrm{arcsec}}\right)^{-1}, \tag{C.2}$$

where 1 parsec (pc) has been defined as the distance of an object when $\pi = 1''$ and the measure baseline is 1 AU, since $1\ \mathrm{rad} = 206264.8''$ and $1\ \mathrm{AU} = 1.49 \times 10^{13}\ \mathrm{cm}$, then

$$1\ \mathrm{pc} = 206264.8\ \mathrm{AU} = 3.09 \times 10^{18}\ \mathrm{cm}.$$

This simple trigonometric method can not be applied accurately from the earth surface for stars with $\pi < 0.03''$ due to atmospheric turbulence effects (seeing) which blurs the star's image; then using ground-based telescopes this method can only be used to measure distances to stars that are about 30 pc from us (Weinberg, 2008).

From 1989 to 1993 the Hipparcos satellite, launched by the European Space Agency (ESA), measured parallaxes for more than 100 000 stars in the solar neighbourhood with a median accuracy of $\sigma = 0.97\ \mathrm{mas}$ (Perryman et al., 1997); this remarkable accuracy can be obtained since the observations were carried out from space and the usual problems related with the terrestrial atmosphere and gravitational field were not present.

C.1.2 The moving-cluster method

The fundamental assumption over which this method is constructed is that of the parallelism in the space motion of the member stars of an open cluster; i.e, the space velocity vectors of the members of the cluster, must point in the same direction. The implications of the previous assumption are that the random motions, the expansion or contraction velocities and the space velocities due to rotation, for the individual members, must be negligible (Hanson, 1975).

Since the space velocity vectors of all the stars in the cluster are parallel, then for an observer for whom the cluster is receding (or approaching), all the stars appear to be moving to (from) a convergent point (CP), the geometry for this situation is depicted in Figure C.2. From the figure we can see that the angle between the positions of the stars and the CP on the sky ψ[1], and the angle between the star's space velocity vector and

---

[1] Note that this angle is seen by an outside fixed observer, from the point of view of an observer on one of the stars there is no such CP at all.
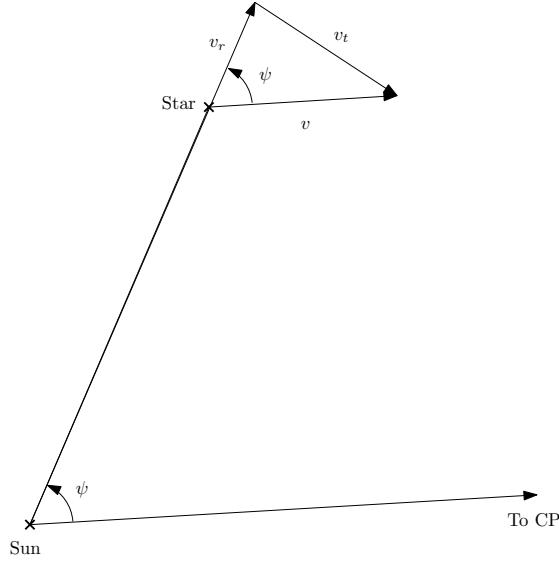
Figure C.2: Scheme that shows the geometric construction for the moving-cluster method; adapted from Binney & Merrifield (1998).

the Sun-star line of sight are the same, then we have that

$$v_t = v_r \tan \psi, \tag{C.3}$$

where v_r is the radial velocity, i.e the space velocity vector component in the direction of the line of sight, and v_t is the tangent velocity defined as

$$v_t = \mu d, \tag{C.4}$$

where μ is the proper motion of the star, i.e. its angular apparent motion on the sky plane, and d is the distance from the sun to the star; then from the two previous definitions we have that

$$d = \frac{v_r \tan \psi}{\mu}, \tag{C.5}$$

or using the definition (C.2)

$$\frac{\pi}{\text{mas}} = \frac{4.74}{\tan \psi} \left(\frac{v_r}{\text{km s}^{-1}} \right)^{-1} \frac{\mu}{\text{mas yr}^{-1}}. \tag{C.6}$$

From the above relation we can determine the parallax or the distance to every star member of the cluster under consideration, using its observed proper motion, radial velocity (easily obtained measuring the shift of spectral lines) and its value of ψ (Binney & Merrifield, 1998).

C.2 Primary Distance Indicators

As previously pointed out, the primary distance indicators are of importance in the calibration of the secondary distance indicators.

C.2.1 Cepheids

The Cepheids are one of the best known primary distance indicators. These variable stars are very bright and since they exhibit a regular variation of their luminosity with time, they are useful to measure distances outside our galaxy. In 1912 Henrietta Swan Leavitt (Leavitt & Pickering, 1912) observed that the Cepheid variables that she was studying in the Small Magellanic Cloud (SMC) have fluxes that vary as a function of the period of the variation in luminosity (Leavitt law). The Cepheids pulsation periods are from 2 to over 100 days whereas their brightness variations go from $-2 < M_V < -6\,\mathrm{mag}$ (Freedman & Madore, 2010).

The basic physics behind the Leavitt law is well understood, the Stephan-Boltzmann law can be written as

$$L = 4\pi R^2 \sigma T_e^4, \tag{C.7}$$

where, L, in this case, is the bolometric luminosity, R is the star radius and T_e is the star effective temperature. Expressing the above relation in therms of magnitudes, we have

$$M_{\mathrm{BOL}} = -5\log_{10} R - 10\log_{10} T_e + C; \tag{C.8}$$

thereafter we can map $\log_{10} T_e$ into an observable intrinsic color like $(B - V)_o$ or $(V - I)_o$ and map the radius into an observable period using a period-mean-density relation [2], then we obtain the period-luminosity-color (PLC) relation for Cepheids as (Freedman & Madore, 2010)

$$M_V = \alpha\log_{10} P + \beta(B - V)_o + \gamma. \tag{C.9}$$

Today the slope of the Period-Luminosity (PL) relation is generally taken from the Cepheids in the Large Magellanic Cloud (LMC). The values of the PL relation given

---

[2] A relation of the type $\omega_{\mathrm{dyn}} = 2\pi/P = (GM/R^3)^{1/2} \approx (G\bar{\rho})^{1/2}$, where ω_{dyn} is the dynamical frequency and is proportional to the inverse of a free fall over the distance of a stellar radius.

by the Hubble Space Telescope (HST) key project (Freedman et al., 2001), assuming that the LMC distance modulus is $\mu(LMC) = 18.50$ mag, are

$$
\begin{aligned}
M_V &= -2.760[\pm 0.03](\log_{10} P - 1) - 4.218[\pm 0.02] & \text{(C.10)} \\
M_I &= -2.962[\pm 0.02](\log_{10} P - 1) - 4.904[\pm 0.01], & \text{(C.11)}
\end{aligned}
$$

where P is the period in days; but this results have been under discussion due to considerations of metallicity effects in the determinations of the LMC distance modulus (Cole, 1998; Girardi et al., 1998; Salaris et al., 2003).

The calibration of the PL relation can be done by observations of galactic Cepheids, in which case trigonometric parallax determinations are generally used. Using data from Hipparcos, the PL relation has been given as (Feast & Catchpole, 1997)

$$
M_V = -2.81 \log_{10} P - 1.43[\pm 0.10]. \tag{C.12}
$$

Assuming the slope given by the last equation, Feast (2005) has parametrized the PL relation as

$$
M_V = -2.81 \log_{10} P + \gamma, \tag{C.13}
$$

where γ is the PL relation zero-point, and using four distinct methods he has obtained a mean value of $\gamma = -1.40$.

Finally, recent work points out that no significant difference exists in the slopes of the PL relation between our Galaxy and the LMC (Fouqué et al., 2007), and gives for our Galaxy

$$
\begin{aligned}
M_V &= -2.678[\pm 0.076] \log_{10} P - 1.275[\pm 0.023] & \text{(C.14)} \\
M_I &= -2.980[\pm 0.074] \log_{10} P - 1.726[\pm 0.022]; & \text{(C.15)}
\end{aligned}
$$

and for the LMC

$$
\begin{aligned}
M_V &= -2.734[\pm 0.029] \log_{10} P - 1.348[\pm 0.007] & \text{(C.16)} \\
M_I &= -2.957[\pm 0.020] \log_{10} P - 1.811[\pm 0.005]; & \text{(C.17)}
\end{aligned}
$$

where it has been assumed that the LMC distance modulus is $\mu(LMC) = 18.40$ mag, which is consistent with recent results (Benedict et al., 2007).

C.2.2 Tip of the red giant branch method

The tip of the red giant branch (TRGB) is a technique for determining distances to nearby galaxies. This method uses the well understood (Salaris et al., 2002) discontinuity in the luminosity function (LF) of stars evolving up the red giant branch (RGB) in old, low metallicity stellar populations that has been calibrated using Galactic globular clusters; necessary condition for its application beeing that the observed RGB LF is well populated (~ 100 stars within 1 mag form the TRGB) (Madore & Freedman, 1995).

The empirical calibration of the TRGB is typically given as:

$$M_I^{TRGB} = f([\text{Fe/H}]) + \text{ZP} \tag{C.18}$$

where, M_I^{TRGB} is the absolute magnitude for the TRGB[3] , $f([\text{Fe/H}])$ is a function of the metallicity (typically a polynomial), and ZP is the calibration Zero Point. This kind of models neglect the impact of other parameters on the calibration and then induce uncertainties of order ± 0.1 mag in the determination of M_I^{TRGB} (Bellazzini, 2008).

C.3 Secondary Distance Indicators

The primary distance indicators are not sufficiently bright to be observed at $z > 0.01$, brighter objects are needed as tracers to constrain a cosmological model, these brighter objects can be galaxies or supernovae, which are as bright as galaxies. We need methods to obtain the luminosity of these objects in order to obtain their distances.

C.3.1 Type Ia supernovae

Type Ia Supernovae (SNe Ia) are the result of the thermonuclear destruction of an accreting carbon-oxygen white dwarf star approaching the Chandrasekhar mass limit. Observationally, the defining characteristic of SNe Ia is the absence of H and He lines and the presence of strong Si absorption lines in their spectra.

In spite of the fact that the details of the nature of the SNe Ia explosion are still obscure, the origin of the observed light curve is relatively well understood. It is powered

---

[3] In this case for the Cousins' I passband, but the model is similar in other bands.

by the radioactive decay of ^{56}Ni into ^{56}Co, and then into ^{56}Fe. The SN ejecta is heated by energetic gamma rays, produced by the radioactive decay, and then radiates thermally to produce the observed light curve. Photometrically, SN Ia rises to maximum light in a period of 20 days, followed by a decline of ~ 3 mag in the following month and ~ 1 mag per month subsequently (Freedman & Madore, 2010; Wolschin, 2010).

SNe Ia are not intrinsically standard candles, but can be standardized by means of simple empirical correspondences. The first of these relations is the light-curve width–luminosity relationship (WLR) or 'Phillips relation' (Phillips, 1993); essentially SN Ia peak luminosities are strongly correlated with the width of their light curve. Furthermore, SN Ia light curves can be parametrized using a 'stretch' parameter, which stretches or contracts a template light curve to match an observed one (Perlmutter et al., 1997). As an aside, the physical origin of the Phillips relation is yet not completely clear (Kasen & Woosley, 2007; Wolschin, 2010).

Another –though poorly understood– relation is between the SNe Ia luminosity and their color B - V (Tripp, 1998; Wolschin, 2010). The two previous relationships can be applied to observed peak magnitudes m:

$$m_{\text{corr}} = m + \alpha(s - 1) - \beta C, \tag{C.19}$$

where the stretch-luminosity is parametrized by α, and the color-luminosity relation by β. After applying the calibration to SNe Ia measurements, precise distance estimates (to $0.12 - 0.14$ mag) can be obtained.

C.3.2   Tully-Fisher relation

Tully & Fisher (1977) proposed the existence of a correlation between the global H I line (21 cm) profile width and the absolute blue magnitude of spiral galaxies; later, after the study of the correlation of the H I width and infrared luminosity, the physical basis for this relation was understood, i.e that the 21 cm line is widened by Doppler effect, caused by the rotation of the galaxy; therefore the H I line width is an indicator of the maximum speed of rotation of the galaxy V_{rot}, which by gravity is related to the mass of the galaxy, which in turn is related to the luminosity L by the mass-luminosity ratio (Aaronson et al., 1979). Roughly, we have

$$L \sim V_{rot}^4. \tag{C.20}$$

The Tully-Fisher relation, calibrated with Cepheids distances and metallicity-corrected, has been given as (Sakai et al., 2000)

$$
\begin{aligned}
B_{T,Z}^c &= -(8.07 \pm 0.72)(\log_{10} W_{20}^c - 2.5) - (19.88 \pm 0.11) &\text{(C.21)} \\
I_{T,Z}^c &= -(9.46 \pm 0.76)(\log_{10} W_{20}^c - 2.5) - (21.19 \pm 0.12), &\text{(C.22)}
\end{aligned}
$$

where $X_{T,Z}^c$ are aperture magnitudes corrected for metallicity and Galactic and internal extinction, and W_{20}^c are the 20% line widths corrected for inclination and redshift.

C.3.3   Faber-Jackson relation

For elliptical galaxies a correlation exists that is similar to the Tully-Fisher relation, only in this case between the luminosity and the velocity dispersion. The theoretical basis for this is too the Virial theorem (Faber & Jackson, 1976). The analytical form of this relation can be given roughly as

$$
L_e \sim \sigma_0^4, \tag{C.23}
$$

where L_e is the luminosity inside the effective radius and σ_0 is the central velocity dispersion measured from spectral line broadening (Binney & Merrifield, 1998).

List of Figures

List of Tables

References

Aaronson, M., Bothun, G., Mould, J., Huchra, J., Schommer, R. A., & Cornell, M. E. 1986, ApJ, 302, 536

Aaronson, M., Huchra, J., & Mould, J. 1979, ApJ, 229, 1

Aguirre, A. 1999, ApJ, 525, 583

Albrecht, A., Bernstein, G., Cahn, R., Freedman, W. L., Hewitt, J., Hu, W., Huth, J., Kamionkowski, M., Kolb, E. W., Knox, L., Mather, J. C., Staggs, S., & Suntzeff, N. B. 2006, ArXiv Astrophysics e-prints

Alloin, D., Bergeron, J., & Pelat, D. 1978, A&A, 70, 141

Amanullah, R., Lidman, C., Rubin, D., Aldering, G., Astier, P., Barbary, K., Burns, M. S., Conley, A., Dawson, K. S., Deustua, S. E., Doi, M., Fabbro, S., Faccioli, L., Fakhouri, H. K., Folatelli, G., Fruchter, A. S., Furusawa, H., Garavini, G., Goldhaber, G., Goobar, A., Groom, D. E., Hook, I., Howell, D. A., Kashikawa, N., Kim, A. G., Knop, R. A., Kowalski, M., Linder, E., Meyers, J., Morokuma, T., Nobili, S., Nordin, J., Nugent, P. E., Östman, L., Pain, R., Panagia, N., Perlmutter, S., Raux, J., Ruiz-Lapuente, P., Spadafora, A. L., Strovink, M., Suzuki, N., Wang, L., Wood-Vasey, W. M., Yasuda, N., & Supernova Cosmology Project, T. 2010, ApJ, 716, 712

Andernach, H., Plionis, M., López-Cruz, O., Tago, E., & Basilakos, S. 2005, in Astronomical Society of the Pacific Conference Series, Vol. 329, Nearby Large-Scale Structures and the Zone of Avoidance, ed. A. P. Fairall & P. A. Woudt, 289–293

Astier, P., Guy, J., Regnault, N., Pain, R., Aubourg, E., Balam, D., Basa, S., Carlberg, R. G., Fabbro, S., Fouchez, D., Hook, I. M., Howell, D. A., Lafoux, H., Neill, J. D., Palanque-Delabrouille, N., Perrett, K., Pritchet, C. J., Rich, J., Sullivan, M., Taillet, R., Aldering, G., Antilogus, P., Arsenijevic, V., Balland, C., Baumont, S., Bronder, J., Courtois, H., Ellis, R. S., Filiol, M., Gonçalves, A. C., Goobar, A., Guide, D., Hardin, D., Lusset, V., Lidman, C., McMahon, R., Mouchet, M., Mourao, A., Perlmutter, S., Ripoche, P., Tao, C., & Walton, N. 2006, A&A, 447, 31

Basilakos, S., & Plionis, M. 1998, MNRAS, 299, 637

References

Basilakos, S., Plionis, M., & Solà, J. 2009, Phys. Rev. D, 80, 083511

Bellazzini, M. 2008, Memorie della Societa Astronomica Italiana, 79, 440

Benedict, G. F., McArthur, B. E., Feast, M. W., Barnes, T. G., Harrison, T. E., Patterson, R. J., Menzies, J. W., Bean, J. L., & Freedman, W. L. 2007, AJ, 133, 1810

Bergeron, J. 1977, ApJ, 211, 62

Binney, J., & Merrifield, M. 1998, Galactic astronomy, ed. J. Binney & M. Merrifield

Brosch, N., Almoznino, E., & Heller, A. B. 2004, MNRAS, 349, 357

Caldwell, R. R., & Kamionkowski, M. 2009, Annual Review of Nuclear and Particle Science, 59, 397

Calzetti, D. 1999, Ap&SS, 266, 243

Campos-Aguilar, A., Moles, M., & Masegosa, J. 1993, AJ, 106, 1784

Carroll, S. M. 2001, Living Reviews in Relativity, 4, 1

Carroll, S. M., Duvvuri, V., Trodden, M., & Turner, M. S. 2004, Phys. Rev. D, 70, 043528

Cole, A. A. 1998, ApJ, 500, L137

Copeland, E. J., Sami, M., & Tsujikawa, S. 2006, International Journal of Modern Physics D, 15, 1753

Copetti, M. V. F., Pastoriza, M. G., & Dottori, H. A. 1986, A&A, 156, 111

Courteau, S., & van den Bergh, S. 1999, AJ, 118, 337

Davis, T. M., Mörtsell, E., Sollerman, J., Becker, A. C., Blondin, S., Challis, P., Clocchiatti, A., Filippenko, A. V., Foley, R. J., Garnavich, P. M., Jha, S., Krisciunas, K., Kirshner, R. P., Leibundgut, B., Li, W., Matheson, T., Miknaitis, G., Pignata, G., Rest, A., Riess, A. G., Schmidt, B. P., Smith, R. C., Spyromilio, J., Stubbs, C. W., Suntzeff, N. B., Tonry, J. L., Wood-Vasey, W. M., & Zenteno, A. 2007, ApJ, 666, 716

Deffayet, C. 2001, Physics Letters B, 502, 199

Dekker, H., D'Odorico, S., Kaufer, A., Delabre, B., & Kotzlowski, H. 2000, in Society of Photo-Optical Instrumentation Engineers (SPIE) Conference Series, Vol. 4008, Society of Photo-Optical Instrumentation Engineers (SPIE) Conference Series, ed. M. Iye & A. F. Moorwood, 534–545

Dottori, H. A., & Bica, E. L. D. 1981, A&A, 102, 245

Doublier, V., Comte, G., Petrosian, A., Surace, C., & Turatto, M. 1997, A&AS, 124, 405

Drell, P. S., Loredo, T. J., & Wasserman, I. 2000, ApJ, 530, 593

Dvali, G., Gabadadze, G., & Porrati, M. 2000, Physics Letters B, 485, 208

Efstathiou, G., Sutherland, W. J., & Maddox, S. J. 1990, Nature, 348, 705

Eisenstein, D. J., Zehavi, I., Hogg, D. W., Scoccimarro, R., Blanton, M. R., Nichol, R. C., Scranton, R., Seo, H., Tegmark, M., Zheng, Z., Anderson, S. F., Annis, J., Bahcall, N., Brinkmann, J., Burles, S., Castander, F. J., Connolly, A., Csabai, I., Doi, M., Fukugita, M., Frieman, J. A., Glazebrook, K., Gunn, J. E., Hendry, J. S., Hennessy, G., Ivezić, Z., Kent, S., Knapp, G. R., Lin, H., Loh, Y., Lupton, R. H., Margon, B., McKay, T. A., Meiksin, A., Munn, J. A., Pope, A., Richmond, M. W., Schlegel, D., Schneider, D. P., Shimasaku, K., Stoughton, C., Strauss, M. A., SubbaRao, M., Szalay, A. S., Szapudi, I., Tucker, D. L., Yanny, B., & York, D. G. 2005, ApJ, 633, 560

Erb, D. K., Shapley, A. E., Steidel, C. C., Pettini, M., Adelberger, K. L., Hunt, M. P., Moorwood, A. F. M., & Cuby, J. 2003, ApJ, 591, 101

Faber, S. M., & Jackson, R. E. 1976, ApJ, 204, 668

Feast, M. 2005, in Astronomical Society of the Pacific Conference Series, Vol. 329, Nearby Large-Scale Structures and the Zone of Avoidance, ed. A. P. Fairall & P. A. Woudt, 241

Feast, M. W., & Catchpole, R. M. 1997, MNRAS, 286, L1

Fixsen, D. J., Cheng, E. S., Gales, J. M., Mather, J. C., Shafer, R. A., & Wright, E. L. 1996, ApJ, 473, 576

Fouqué, P., Arriagada, P., Storm, J., Barnes, T. G., Nardetto, N., Mérand, A., Kervella, P., Gieren, W., Bersier, D., Benedict, G. F., & McArthur, B. E. 2007, A&A, 476, 73

Freedman, W. L., & Madore, B. F. 2010, ArXiv e-prints

Freedman, W. L., Madore, B. F., Gibson, B. K., Ferrarese, L., Kelson, D. D., Sakai, S., Mould, J. R., Kennicutt, Jr., R. C., Ford, H. C., Graham, J. A., Huchra, J. P., Hughes, S. M. G., Illingworth, G. D., Macri, L. M., & Stetson, P. B. 2001, ApJ, 553, 47

French, H. B. 1980, ApJ, 240, 41

Frieman, J. A., Huterer, D., Linder, E. V., & Turner, M. S. 2003, Phys. Rev. D, 67, 083505

Frieman, J. A., Turner, M. S., & Huterer, D. 2008, ARA&A, 46, 385

References

García-Benito, R. 2009, PhD thesis, Universidad Autonoma de Madrid

Giavalisco, M. 2002, ARA&A, 40, 579

Girardi, L., Groenewegen, M. A. T., Weiss, A., & Salaris, M. 1998, MNRAS, 301, 149

González Delgado, R. M., Leitherer, C., & Heckman, T. M. 1999, ApJS, 125, 489

Haiman, Z., Mohr, J. J., & Holder, G. P. 2001, ApJ, 553, 545

Hanson, R. B. 1975, AJ, 80, 379

Haro, G. 1956, Boletin de los Observatorios Tonantzintla y Tacubaya, 2, 8

Heckman, T. M., Miley, G. K., van Breugel, W. J. M., & Butcher, H. R. 1981, ApJ, 247, 403

Hicken, M., Wood-Vasey, W. M., Blondin, S., Challis, P., Jha, S., Kelly, P. L., Rest, A., & Kirshner, R. P. 2009, ApJ, 700, 1097

Hobson, M. P., Efstathiou, G. P., & Lasenby, A. N. 2005, General Relativity, ed. C. U. Press

Hu, W., & Dodelson, S. 2002, ARA&A, 40, 171

Hu, W., & Jain, B. 2004, Phys. Rev. D, 70, 043009

Humason, M. L., & Zwicky, F. 1947, ApJ, 105, 85

Jaffe, A. H., Ade, P. A., Balbi, A., Bock, J. J., Bond, J. R., Borrill, J., Boscaleri, A., Coble, K., Crill, B. P., de Bernardis, P., Farese, P., Ferreira, P. G., Ganga, K., Giacometti, M., Hanany, S., Hivon, E., Hristov, V. V., Iacoangeli, A., Lange, A. E., Lee, A. T., Martinis, L., Masi, S., Mauskopf, P. D., Melchiorri, A., Montroy, T., Netterfield, C. B., Oh, S., Pascale, E., Piacentini, F., Pogosyan, D., Prunet, S., Rabii, B., Rao, S., Richards, P. L., Romeo, G., Ruhl, J. E., Scaramuzzi, F., Sforna, D., Smoot, G. F., Stompor, R., Winant, C. D., & Wu, J. H. 2001, Physical Review Letters, 86, 3475

Kaiser, N. 1987, MNRAS, 227, 1

Kaper, L., D'Odorico, S., Hammer, F., Pallavicini, R., Kjaergaard Rasmussen, P., Dekker, H., Francois, P., Goldoni, P., Guinouard, I., Groot, P. J., Hjorth, J., Horrobin, M., Navarro, R., Royer, F., Santin, P., Vernet, J., & Zerbi, F. 2009, in Science with the VLT in the ELT Era, ed. A. Moorwood, 319

Kasen, D., & Woosley, S. E. 2007, ApJ, 656, 661

Kinman, T. D., & Davidson, K. 1981, ApJ, 243, 127

Kitchin, C. R. 1995, Optical astronomical spectroscopy, ed. Kitchin, C. R.

Koo, D. C., Guzman, R., Faber, S. M., Illingworth, G. D., Bershady, M. A., Kron, R. G., & Takamiya, M. 1995, ApJ, 440, L49

Kunth, D., & Östlin, G. 2000, A&A Rev., 10, 1

Kunth, D., & Sargent, W. L. W. 1983, ApJ, 273, 81

Leavitt, H. S., & Pickering, E. C. 1912, Harvard College Observatory Circular, 173, 1

Leibundgut, B. 2001, ARA&A, 39, 67

Lequeux, J., Peimbert, M., Rayo, J. F., Serrano, A., & Torres-Peimbert, S. 1979, A&A, 80, 155

Linder, E. V. 2003, Physical Review Letters, 90, 091301

—. 2010, ArXiv e-prints

MacAlpine, G. M., Smith, S. B., & Lewis, D. W. 1977, ApJS, 34, 95

Maddox, S. J., Efstathiou, G., Sutherland, W. J., & Loveday, J. 1990, MNRAS, 242, 43P

Madore, B. F., & Freedman, W. L. 1995, AJ, 109, 1645

Markarian, B. E. 1967, Astrofizika, 3, 24

Markarian, B. E., Lipovetskii, V. A., & Stepanyan, D. A. 1981, Astrophysics, 17, 321

Mather, J. C., Cheng, E. S., Eplee, Jr., R. E., Isaacman, R. B., Meyer, S. S., Shafer, R. A., Weiss, R., Wright, E. L., Bennett, C. L., Boggess, N. W., Dwek, E., Gulkis, S., Hauser, M. G., Janssen, M., Kelsall, T., Lubin, P. M., Moseley, Jr., S. H., Murdock, T. L., Silverberg, R. F., Smoot, G. F., & Wilkinson, D. T. 1990, ApJ, 354, L37

Melnick, J. 1978, A&A, 70, 157

Melnick, J. 2003, in Astronomical Society of the Pacific Conference Series, Vol. 297, Star Formation Through Time, ed. E. Perez, R. M. Gonzalez Delgado, & G. Tenorio-Tagle, 3

Melnick, J., Moles, M., Terlevich, R., & Garcia-Pelayo, J.-M. 1987, MNRAS, 226, 849

Melnick, J., Tenorio-Tagle, G., & Terlevich, R. 1999, MNRAS, 302, 677

Melnick, J., Terlevich, R., & Moles, M. 1988, MNRAS, 235, 297

Melnick, J., Terlevich, R., & Terlevich, E. 2000, MNRAS, 311, 629

References

Miknaitis, G., Pignata, G., Rest, A., Wood-Vasey, W. M., Blondin, S., Challis, P., Smith, R. C., Stubbs, C. W., Suntzeff, N. B., Foley, R. J., Matheson, T., Tonry, J. L., Aguilera, C., Blackman, J. W., Becker, A. C., Clocchiatti, A., Covarrubias, R., Davis, T. M., Filippenko, A. V., Garg, A., Garnavich, P. M., Hicken, M., Jha, S., Krisciunas, K., Kirshner, R. P., Leibundgut, B., Li, W., Miceli, A., Narayan, G., Prieto, J. L., Riess, A. G., Salvo, M. E., Schmidt, B. P., Sollerman, J., Spyromilio, J., & Zenteno, A. 2007, ApJ, 666, 674

Noguchi, K., Aoki, W., Kawanomoto, S., Ando, H., Honda, S., Izumiura, H., Kambe, E., Okita, K., Sadakane, K., Sato, B., Tajitsu, A., Takada-Hidai, T., Tanaka, W., Watanabe, E., & Yoshida, M. 2002, PASJ, 54, 855

Olofsson, K. 1995, A&AS, 111, 57

Osterbrock, D. E. 1988, PASP, 100, 412

—. 1989, Astrophysics of gaseous nebulae and active galactic nuclei, ed. University Science Books

Pagel, B. E. J., Simonson, E. A., Terlevich, R. J., & Edmunds, M. G. 1992, MNRAS, 255, 325

Peacock, J. A., Schneider, P., Efstathiou, G., Ellis, J. R., Leibundgut, B., Lilly, S. J., & Mellier, Y. 2006, ESA-ESO Working Group on "Fundamental Cosmology", Tech. rep.

Perlmutter, S., Aldering, G., Goldhaber, G., Knop, R. A., Nugent, P., Castro, P. G., Deustua, S., Fabbro, S., Goobar, A., Groom, D. E., Hook, I. M., Kim, A. G., Kim, M. Y., Lee, J. C., Nunes, N. J., Pain, R., Pennypacker, C. R., Quimby, R., Lidman, C., Ellis, R. S., Irwin, M., McMahon, R. G., Ruiz-Lapuente, P., Walton, N., Schaefer, B., Boyle, B. J., Filippenko, A. V., Matheson, T., Fruchter, A. S., Panagia, N., Newberg, H. J. M., Couch, W. J., & The Supernova Cosmology Project. 1999, ApJ, 517, 565

Perlmutter, S., Gabi, S., Goldhaber, G., Goobar, A., Groom, D. E., Hook, I. M., Kim, A. G., Kim, M. Y., Lee, J. C., Pain, R., Pennypacker, C. R., Small, I. A., Ellis, R. S., McMahon, R. G., Boyle, B. J., Bunclark, P. S., Carter, D., Irwin, M. J., Glazebrook, K., Newberg, H. J. M., Filippenko, A. V., Matheson, T., Dopita, M., Couch, W. J., & The Supernova Cosmology Project. 1997, ApJ, 483, 565

Perlmutter, S., & Schmidt, B. P. 2003, in Lecture Notes in Physics, Berlin Springer Verlag, Vol. 598, Supernovae and Gamma-Ray Bursters, ed. K. Weiler, 195–217

Perryman, M. A. C., Lindegren, L., Kovalevsky, J., Hoeg, E., Bastian, U., Bernacca, P. L., Crézé, M., Donati, F., Grenon, M., van Leeuwen, F., van der Marel, H., Mignard, F., Murray, C. A., Le Poole, R. S., Schrijver, H., Turon, C., Arenou, F., Froeschlé, M., & Petersen, C. S. 1997, A&A, 323, L49

Pettini, M., Shapley, A. E., Steidel, C. C., Cuby, J., Dickinson, M., Moorwood, A. F. M., Adelberger, K. L., & Giavalisco, M. 2001, ApJ, 554, 981

Phillips, M. M. 1993, ApJ, 413, L105

Plionis, M., Terlevich, R., Basilakos, S., Bresolin, F., Terlevich, E., Melnick, J., & Chávez, R. 2010, in American Institute of Physics Conference Series, Vol. 1241, American Institute of Physics Conference Series, ed. J.-M. Alimi & A. Fuözfa, 267–276

Plionis, M., Terlevich, R., Basilakos, S., Bresolin, F., Terlevich, E., Melnick, J., & Georgantopoulos, I. 2009, Journal of Physics Conference Series, 189, 012032

Pryke, C., Halverson, N. W., Leitch, E. M., Kovac, J., Carlstrom, J. E., Holzapfel, W. L., & Dragovan, M. 2002, ApJ, 568, 46

Pustilnik, S. A., Kniazev, A. Y., Lipovetsky, V. A., & Ugryumov, A. V. 2001, A&A, 373, 24

Ratra, B., & Vogeley, M. S. 2008, PASP, 120, 235

Reichardt, C. L., Ade, P. A. R., Bock, J. J., Bond, J. R., Brevik, J. A., Contaldi, C. R., Daub, M. D., Dempsey, J. T., Goldstein, J. H., Holzapfel, W. L., Kuo, C. L., Lange, A. E., Lueker, M., Newcomb, M., Peterson, J. B., Ruhl, J., Runyan, M. C., & Staniszewski, Z. 2009, ApJ, 694, 1200

Riess, A. G., Filippenko, A. V., Challis, P., Clocchiatti, A., Diercks, A., Garnavich, P. M., Gilliland, R. L., Hogan, C. J., Jha, S., Kirshner, R. P., Leibundgut, B., Phillips, M. M., Reiss, D., Schmidt, B. P., Schommer, R. A., Smith, R. C., Spyromilio, J., Stubbs, C., Suntzeff, N. B., & Tonry, J. 1998, AJ, 116, 1009

Riess, A. G., Strolger, L., Casertano, S., Ferguson, H. C., Mobasher, B., Gold, B., Challis, P. J., Filippenko, A. V., Jha, S., Li, W., Tonry, J., Foley, R., Kirshner, R. P., Dickinson, M., MacDonald, E., Eisenstein, D., Livio, M., Younger, J., Xu, C., Dahlén, T., & Stern, D. 2007, ApJ, 659, 98

Robertson, H. P. 1935, ApJ, 82, 284

Rosa-González, D., Terlevich, E., & Terlevich, R. 2002, MNRAS, 332, 283

Sakai, S., Mould, J. R., Hughes, S. M. G., Huchra, J. P., Macri, L. M., Kennicutt, Jr., R. C., Gibson, B. K., Ferrarese, L., Freedman, W. L., Han, M., Ford, H. C., Graham, J. A., Illingworth, G. D., Kelson, D. D., Madore, B. F., Sebo, K., Silbermann, N. A., & Stetson, P. B. 2000, ApJ, 529, 698

Salaris, M., Cassisi, S., & Weiss, A. 2002, PASP, 114, 375

Salaris, M., Percival, S., & Girardi, L. 2003, MNRAS, 345, 1030

Sargent, W. L. W., & Searle, L. 1970, ApJ, 162, L155

Searle, L., & Sargent, W. L. W. 1972, ApJ, 173, 25

Seljak, U., Makarov, A., McDonald, P., Anderson, S. F., Bahcall, N. A., Brinkmann, J., Burles, S., Cen, R., Doi, M., Gunn, J. E., Ivezić, Ž., Kent, S., Loveday, J., Lupton, R. H., Munn, J. A., Nichol, R. C., Ostriker, J. P., Schlegel, D. J., Schneider, D. P., Tegmark, M., Berk, D. E., Weinberg, D. H., & York, D. G. 2005, Phys. Rev. D, 71, 103515

Shields, G. A. 1990, ARA&A, 28, 525

Siegel, E. R., Guzmán, R., Gallego, J. P., Orduña López, M., & Rodríguez Hidalgo, P. 2005, MNRAS, 356, 1117

Smith, M. G., Aguirre, C., & Zemelman, M. 1976, ApJS, 32, 217

Song, Y., Hu, W., & Sawicki, I. 2007, Phys. Rev. D, 75, 044004

Spergel, D. N., Bean, R., Doré, O., Nolta, M. R., Bennett, C. L., Dunkley, J., Hinshaw, G., Jarosik, N., Komatsu, E., Page, L., Peiris, H. V., Verde, L., Halpern, M., Hill, R. S., Kogut, A., Limon, M., Meyer, S. S., Odegard, N., Tucker, G. S., Weiland, J. L., Wollack, E., & Wright, E. L. 2007, ApJS, 170, 377

Spergel, D. N., Verde, L., Peiris, H. V., Komatsu, E., Nolta, M. R., Bennett, C. L., Halpern, M., Hinshaw, G., Jarosik, N., Kogut, A., Limon, M., Meyer, S. S., Page, L., Tucker, G. S., Weiland, J. L., Wollack, E., & Wright, E. L. 2003, ApJS, 148, 175

Taylor, C. L. 1997, ApJ, 480, 524

Tegmark, M., Eisenstein, D. J., Strauss, M. A., Weinberg, D. H., Blanton, M. R., Frieman, J. A., Fukugita, M., Gunn, J. E., Hamilton, A. J. S., Knapp, G. R., Nichol, R. C., Ostriker, J. P., Padmanabhan, N., Percival, W. J., Schlegel, D. J., Schneider, D. P., Scoccimarro, R., Seljak, U., Seo, H.-J., Swanson, M., Szalay, A. S., Vogeley, M. S., Yoo, J., Zehavi, I., Abazajian, K., Anderson, S. F., Annis, J., Bahcall, N. A., Bassett, B., Berlind, A., Brinkmann, J., Budavari, T., Castander, F., Connolly, A., Csabai, I., Doi, M., Finkbeiner, D. P., Gillespie, B., Glazebrook, K., Hennessy, G. S., Hogg, D. W., Ivezić, Ž., Jain, B., Johnston, D., Kent, S., Lamb, D. Q., Lee, B. C., Lin, H., Loveday, J., Lupton, R. H., Munn, J. A., Pan, K., Park, C., Peoples, J., Pier, J. R., Pope, A., Richmond, M., Rockosi, C., Scranton, R., Sheth, R. K., Stebbins, A., Stoughton, C., Szapudi, I., Tucker, D. L., Berk, D. E. V., Yanny, B., & York, D. G. 2006, Phys. Rev. D, 74, 123507

Tegmark, M., Strauss, M. A., Blanton, M. R., Abazajian, K., Dodelson, S., Sandvik, H., Wang, X., Weinberg, D. H., Zehavi, I., Bahcall, N. A., Hoyle, F., Schlegel, D., Scoccimarro, R., Vogeley, M. S., Berlind, A., Budavari, T., Connolly, A., Eisenstein,

D. J., Finkbeiner, D., Frieman, J. A., Gunn, J. E., Hui, L., Jain, B., Johnston, D., Kent, S., Lin, H., Nakajima, R., Nichol, R. C., Ostriker, J. P., Pope, A., Scranton, R., Seljak, U., Sheth, R. K., Stebbins, A., Szalay, A. S., Szapudi, I., Xu, Y., Annis, J., Brinkmann, J., Burles, S., Castander, F. J., Csabai, I., Loveday, J., Doi, M., Fukugita, M., Gillespie, B., Hennessy, G., Hogg, D. W., Ivezić, Ž., Knapp, G. R., Lamb, D. Q., Lee, B. C., Lupton, R. H., McKay, T. A., Kunszt, P., Munn, J. A., O'Connell, L., Peoples, J., Pier, J. R., Richmond, M., Rockosi, C., Schneider, D. P., Stoughton, C., Tucker, D. L., vanden Berk, D. E., Yanny, B., & York, D. G. 2004, Phys. Rev. D, 69, 103501

Telles, E. 2003, in Astronomical Society of the Pacific Conference Series, Vol. 297, Star Formation Through Time, ed. E. Perez, R. M. Gonzalez Delgado, & G. Tenorio-Tagle, 143

Telles, E., & Maddox, S. 2000, MNRAS, 311, 307

Telles, E., Melnick, J., & Terlevich, R. 1997, MNRAS, 288, 78

Telles, E., & Terlevich, R. 1995, MNRAS, 275, 1

—. 1997, MNRAS, 286, 183

Telles, J. E. 1995, PhD thesis, Univ. Cambridge, (1995)

Terlevich, R., & Melnick, J. 1981, MNRAS, 195, 839

Terlevich, R., Melnick, J., Masegosa, J., Moles, M., & Copetti, M. V. F. 1991, A&AS, 91, 285

Terlevich, R., Terlevich, E., Rosa-González, D., & Silich, S. 2003, in Astronomical Society of the Pacific Conference Series, Vol. 297, Star Formation Through Time, ed. E. Perez, R. M. Gonzalez Delgado, & G. Tenorio-Tagle, 149

Tresse, L., Maddox, S., Loveday, J., & Singleton, C. 1999, MNRAS, 310, 262

Tripp, R. 1998, A&A, 331, 815

Tully, R. B., & Fisher, J. R. 1977, A&A, 54, 661

Verde, L. 2010, in Lecture Notes in Physics, Berlin Springer Verlag, Vol. 800, Lecture Notes in Physics, Berlin Springer Verlag, ed. G. Wolschin, 147–177

Vílchez, J. M. 1995, AJ, 110, 1090

Warren, M. S., Abazajian, K., Holz, D. E., & Teodoro, L. 2006, ApJ, 646, 881

Weinberg, S. 1989, Reviews of Modern Physics, 61, 1

—. 2008, Cosmology, ed. S. Weinberg (Oxford University Press)

Whittle, M. 1985, MNRAS, 213, 1

Wolschin, G., ed. 2010, Lecture Notes in Physics, Berlin Springer Verlag, Vol. 800, Lectures on Cosmology Accelerated Expansion of the Universe

Yadav, J., Bharadwaj, S., Pandey, B., & Seshadri, T. R. 2005, MNRAS, 364, 601

Zwicky, F., & Zwicky, M. A. 1971, Catalogue of selected compact galaxies and of post-eruptive galaxies, ed. Zwicky, F. & Zwicky, M. A.